

NOVEL SENSING APPROACHES TOWARDS ULTIMATE MEMS SENSORS

by

Varun Subramaniam Kumar



APPROVED BY SUPERVISORY COMMITTEE:

Siavash Pourkamali, Chair

Jeong-Bong Lee

Walter Hu

S. O. Reza Moheimani

Copyright 2018

Varun Subramaniam Kumar

All Rights Reserved

NOVEL SENSING APPROACHES TOWARDS ULTIMATE MEMS SENSORS

by

VARUN SUBRAMANIAM KUMAR, B. TECH, MS

DISSERTATION

Presented to the Faculty of

The University of Texas at Dallas

in Partial Fulfillment

of the Requirements

for the Degree of

DOCTOR OF PHILOSOPHY IN

ELECTRICAL ENGINEERING

THE UNIVERSITY OF TEXAS AT DALLAS

May 2018

ACKNOWLEDGMENTS

I would like to express my sincere gratitude to my advisor, Dr. Siavash Pourkamali for funding and encouraging my research and for allowing me to grow as a research scientist. Your advice on both research as well as on my career have been priceless. I would like to thank him for his guidance throughout the course of my research work and for his encouraging advice without which this dissertation would be incomplete. I would also like to thank my dissertation committee members: Dr. J B Lee, Dr. Walter Hu and Dr. Reza Moheimani for taking out time to give me your brilliant suggestions and comments. They are always appreciated.

My sincere thanks to my former and current colleagues at “Micron X” (μnX) lab- Dr. Emad Mehdizadeh, Alireza Ramezany, Mohammad Mahdavi, Amin Abbasalipour, Vahid Qaradaghi and Dr. Maribel Maldonado Garcia. I would also like to thank the staff at the UTD Cleanroom Research Laboratory for their ceaseless effort and valuable input regarding usage of cleanroom tools.

A special thanks to my father and mother for the infinite sacrifices they have made on my behalf- If not for your prayers, I would have never come this far. I also wish to thank my wife, Sushmita Sudarshan for being a constant motivation for me to move forward each day that goes by.

January 2018

NOVEL SENSING APPROACHES TOWARDS ULTIMATE MEMS SENSORS

Varun Subramaniam Kumar, PhD
The University of Texas at Dallas, 2018

Supervising Professor: Dr. Siavash Pourkamali

Within the past few decades, various micro-electromechanical (MEMS) accelerometers, magnetometers and vibration sensors utilizing different actuation and sensing mechanisms have been demonstrated. Such sensors are integral to various consumer, industrial, military, environmental and biomedical applications. Although abovementioned sensors based on MEMS technology have been successfully developed and commercialized and are widely used, this dissertation focuses on exploring novel approaches to significantly improve the performance of such sensors.

In most cases for the MEMS accelerometer, the large power consumption of MEMS sensors is attributed to the analog front end needed for reading, processing, and analog to digital conversion of the sensor output, which is typically responsible for most to all the power consumption of the whole sensor. The proposed effort in this dissertation aims at development of a new class of digitally readable MEMS accelerometers allowing significant power reduction by eliminating the need for the analog front-end.

Conventional magnetometers that offer high sensitivities for fields smaller than a few nT's are not MEMS compatible and cannot undergo miniaturization. MEMS Magnetometers have an edge over

conventional counterparts due to their unique features such as small size, low cost, lower power consumption and simplicity of operation. Such properties offer unrivalled advantages, especially when it comes to medical applications, such as magneto-encephalography, where compact arrays of ultra-sensitive sensors are desirable. This dissertation demonstrates ultra-high sensitivities (noise floor in $\text{pT}/\sqrt{\text{Hz}}$) for a Lorentz force resonant MEMS magnetometer enabled by internal-thermal piezoresistive vibration amplification. A detailed model of the magneto-thermo-electro-mechanical internal amplification is also developed and studied. Frequency output Lorentz force MEMS magnetometers with enhanced sensitivity using a leverage mechanism have also been explored.

Currently no low cost, low power, and compact vibration sensor solution exists that can provide frequency distribution data for the measured vibrations. This dissertation shows implementation and characterization of building blocks of a low-power miniaturized vibration spectrum analyzer with a resolution of 1mg over a wide frequency range (0-10kHz) using a standard CMOS process, without adding any complex post processing fabrication steps.

In summary, under this work, digitally operated MEMS accelerometers, ultra-sensitive Lorentz force MEMS magnetometers, and building blocks of low power wideband CMOS-MEMS vibration sensors have been successfully designed and implemented.

TABLE OF CONTENTS

ACKNOWLEDGMENTS.....	iv
ABSTRACT.....	v
LIST OF FIGURES.....	xi
LIST OF TABLES.....	xvii
CHAPTER 1 INTRODUCTION.....	1
1.1 Microelectromechanical Systems.....	1
1.2 MEMS Accelerometers.....	2
1.3 MEMS Magnetometers.....	4
1.4 CMOS-MEMS Vibration Sensors.....	8
CHAPTER 2 ULTRA-LOW POWER DIGITALLY OPERATED MEMS ACCELEROMETERS.....	12
2.1 Principle of Operation.....	12
2.2 MEMS Tunneling Accelerometer.....	13
2.2.1 Background and Motivation.....	13
2.2.2 Device Description and Fabrication.....	14
2.2.3 Measurement Setup and Results.....	16
CHAPTER 3 BINARY TUNABLE INERTIAL SENSORS WITH USE OF DIGITAL CONTROL.....	20
3.1 Linear Accelerometer.....	20
3.1.1 Device Description.....	20

3.1.2 Design Considerations.....	21
3.1.3 Design Specifications.....	22
3.1.4 Binary Search for Acceleration Measurement.....	23
3.1.5 Device Fabrication.....	25
3.1.6 Measurement Setup and Results- Determination of electrode voltages	25
3.1.7 Operating Power Consumption.....	29
3.2 Rotational Accelerometer.....	30
3.2.1 Device Description.....	30
3.2.2 Device Fabrication.....	31
3.2.3 Device Performance.....	32
3.2.4 Resonance Response.....	34
CHAPTER 4 BINARY TUNABLE INERTIAL SENSORS WITHOUT USE OF DIGITAL CONTROL.....	36
4.1 Self-Computing Coupled Switch Inertial Sensors.....	36
4.2 Device Fabrication.....	38
4.3 Measurement Setup and Results.....	38
CHAPTER 5 SENSITIVITY ENHANCEMENT OF AMPLITUDE MODULATED LORENTZ FORCE MEMS MAGNETOMETERS.....	43
5.1 Internal Thermal-Piezoresistive Amplification.....	43
5.2 Electro-thermo-mechanical Model.....	46
5.3 Device Fabrication and Description.....	49
5.4 Measurement Results.....	50

5.4.1 Test Setup.....	50
5.4.2 Results.....	51
5.4.3 Noise Floor, Stability and Sensor Field Resolution.....	55
CHAPTER 6 SENSITIVITY ENHANCEMENT OF FREQUENCY MODULATED LORENTZ FORCE MEMS MAGNETOMETERS.....	60
6.1 Principle of Operation- Leverage Mechanism.....	60
6.2 Device Description.....	60
6.3 Lorentz Force Beam Design.....	62
6.4 Piezoresistive Beam Design.....	65
6.5 Device Fabrication.....	66
6.6 Measurement Results.....	69
6.6.1 Measurement Setup.....	69
6.6.2 Results.....	71
6.6.3 Noise Analysis.....	75
6.6.4 Temperature Compensation.....	79
CHAPTER 7 LOW POWER, WIDEBAND, CMOS COMPATIBLE MEMS VIBRATION SENSORS.....	80
7.1 Principle of Operation.....	80
7.2 Stress Sensing.....	80
7.3 Mechanical Design and Theoretical Analysis.....	81
7.4 Associated Terms and Mathematical Analysis.....	86
7.5 Initial Test Chip Fabrication.....	88

7.6 Preliminary Results.....	91
7.7 Capacitive and Magnetic Modulation for Extended Bandwidth.....	97
7.8 Design Refinements for Extended Operation Bandwidth.....	98
7.9 Post Process Fabrication.....	99
7.10 Measurement Results.....	102
7.11 Summary.....	103
CHAPTER 8 CONCLUSIONS AND FUTURE WORK.....	107
8.1 Contributions.....	107
8.2 Future Direction.....	109
REFERENCES.....	111
BIOGRAPHICAL SKETCH.....	118
CURRICULUM VITAE.....	119

LIST OF FIGURES

Figure 2.1	Schematic cross-sectional view of the process flow for the fabrication of the accelerometer.....	15
Figure 2.2	Figure 2.2(a). SEM View of the Tunneling Current Accelerometer. (b). Zoomed-in view of the gap between the tip and the counter electrode. (c). SEM view of the tunable electrodes.....	16
Figure 2.3	Schematic view of the test setup electrical connections for testing the tunneling accelerometer.....	17
Figure 2.4	$\ln(I/V^2)$ versus $1/V$ plot depicting linearity of the Fowler Nordheim Theorem fitted with a straight line.....	18
Figure 2.5	Tunneling current versus gap voltage for different probe bias voltages.....	18
Figure 2.6	Measured tunneling current for different probe bias voltages having constant gap control voltage.....	18
Figure 2.7	Measured tunneling current for different accelerations due to variation in tilt angle of the device.....	18
Figure 3.1	Simplified schematic view of a 3-bit digitally operated accelerometer.....	20
Figure 3.2	Flowchart showing algorithm for binary search in a 3-bit digital accelerometer.	23
Figure 3.3	(a). SEM view a fabricated digital accelerometer also showing device electrical connections for testing its performance; (b). Zoomed in view of the output electrode tip area and the parallel plate actuators. (c). Zoomed-in side view of the gap between the proof mass and the output electrode showing the gap narrowed down by gold deposition.....	26
Figure 3.4	Flowchart showing algorithm for binary search in a 2-bit digital accelerometer.	29
Figure 3.5	Simplified schematic of the 3-bit digitally operated rotational accelerometer....	31
Figure 3.6	SEM views of the fabricated digital rotational accelerometer.....	32
Figure 3.7	Measured sensor frequency response for polarization voltage of 10V along with finite element modal analysis of the structure showing the sensor's resonance mode shape.....	34

Figure 4.1	Simplified schematic of a 3-bit coupled switch accelerometer with digitized binary output.....	36
Figure 4.2	SEM views of the two-bit digital accelerometer along with the zoomed-in views of the contact gap.....	39
Figure 5.1	(a). Finite element modal analysis of the resonator showing its in-plane resonance mode due to magnetic field actuation. (b). Expansion and contraction of the piezoresistive beam due to the alternating heating and cooling half cycles.....	44
Figure 5.2	Schematic diagram for the resonant magnetometer highlighting the interactions between different domains involved (Magnetic, Thermal, Mechanical and Electrical) and the resulting feedback loop. Amplification occurs when the feedback loop has a positive overall gain less than unity.....	46
Figure 5.3	SEM view of the 400kHz dual plate in-plane resonant magnetometer. Right- Zoomed-in view of the piezoresistor ($30\mu\text{m}\times 1.5\mu\text{m}\times 15\mu\text{m}$).....	50
Figure 5.4	Finite element modal analysis of the resonator showing the in-plane resonance mode and the measurement setup and its electrical connections.....	51
Figure 5.5	Resonant responses of the device with different bias currents under constant magnetic field intensity of 3.5 nT for bias currents in the range 5.164mA-7.245mA. Inset shows the resonant response of the device at 5.164mA having a quality factor of ~680. Bottom: Resonant responses of the device with different bias currents under constant magnetic field intensity of 3.5 nT for bias currents in the range 7.008mA-7.245mA.....	52
Figure 5.6	Graph showing measured effective Quality Factor versus the bias current demonstrating the Q and vibration amplification effect. Inset- Network Analyzer response for piezoresistor bias current of 7.245 mA...	53
Figure 5.7	Graph showing the output voltage amplitude and the FOMS values versus the magnetic field intensity for different bias currents.....	54
Figure 5.8	Output spectrum of the sensor for an input magnetic field of 3.5nT along with its measured noise floor for a bias current of 5.164mA. Inset: Output noise spectrum for the sensor measured at the bias current of 5.164mA.....	56

Figure 5.9	Output spectrum of the sensor for an input magnetic field of 3.5nT along with its measured noise floor for a bias current of 7.245mA. Inset: Output noise spectrum for the sensor measured at the bias current of 7.245mA.....	56
Figure 5.10	Measured Allan Deviation for the sensor output at a DC bias of 7.25mA.....	58
Figure 5.11	Measured standard deviations of the resonance peak frequency compared with the 3dB bandwidth of the sensor for various bias currents.....	59
Figure 6.1	(a). Simple schematic showing the basic concept of the amplification mechanism. (b) (c) (d). Finite element static force analysis of the frequency modulated resonator showing the force amplification due to the leverage mechanism for three different beam structures (Type A, Type B and Type C).....	61
Figure 6.2	Schematic showing the bending of the Lorentz force beams and the piezoresistive beam due to the applied Lorentz Force F_l	63
Figure 6.3	Schematic view of the different types of piezoresistive beams used in this work.....	66
Figure 6.4	Process flow used for the fabrication of the Lorentz force magnetometer.....	68
Figure 6.5	SEM view of the fabricated structure along with the test electrical connections. The piezoresistive beam has three different designs- Type A, Type B and Type C. Zoomed in views of all the piezoresistors are shown on the right-hand side. All other parameters and dimensions remain the same throughout all three structures.....	69
Figure 6.6	Overall Frequency shift under a constant field of 0.3T for different Lorentz force and resonator bias currents for Type A design. Inset: The frequency shift at an I_g of zero due to the Lorentz force caused by the resonator bias current.....	71
Figure 6.7	Type B- Measured resonance responses under different magnetic field intensities for a fixed Lorentz force current of 8mA and resonator bias current of 27mA...	73
Figure 6.8	Type B- Resonance responses for different Lorentz force currents under constant field of 0.3T and resonator bias current of 11mA.....	73
Figure 6.9	Type B- Overall Frequency shift under a constant field of 0.3T for different Lorentz force and resonator bias currents. Inset: The frequency shift at an I_g of zero due to the Lorentz force caused by the resonator bias current.....	73

Figure 6.10	Type C- Measured resonance responses under different magnetic field intensities for a fixed Lorentz force current of 17mA and resonator bias current of 27mA. 74
Figure 6.11	Type C- Resonance responses for different Lorentz force currents under constant field of 0.3T and resonator bias current of 11mA..... 74
Figure 6.12	Type C- Overall Frequency shift under a constant field of 0.3T for different Lorentz force and resonator bias currents. Inset: The frequency shift at an I_g of zero due to the Lorentz force caused by the resonator bias current..... 74
Figure 6.13	(a) (b). Measured standard deviations of the resonance peak frequency at various bias currents for Type A, B and C designs..... 78
Figure 7.1	Schematic view of the single chip vibration sensor that utilizes a standard CMOS process to implement stress sensors. The thinned down silicon substrate turns vibrations into surface stress (compressive and tensile) that is detected by n-well or p-well silicon piezoresistors within the CMOS chip designed in a Wheatstone's bridge fashion..... 81
Figure 7.2	(a). Simple piezoresistive cantilever-based vibration sensor. (b). COMSOL modal analysis showing stress profile on application of a 1mg vibration at DC..... 82
Figure 7.3	(a). Simple piezoresistive cantilever-based vibration sensor with added mass. (b). COMSOL modal analysis showing stress profile on application of a 1mg vibration at DC..... 83
Figure 7.4	COMSOL modal analysis showing stress profile on application of a 1mg vibration at DC for a device with added mass and deep trench under the piezoresistor.... 84
Figure 7.5	(a). Resonance response of the vibration sensor with the attached mass and backside trench. (b). Trade-off between bandwidth and sensitivity of the device..... 84
Figure 7.6	(a). Device structure with multiple modes/trenches for wider bandwidth operation along with their respective mode shapes. (b). Resonance response of the device for a vibration of 1mg..... ..85
Figure 7.7	Multiple trenches on the back-side of the CMOS chip enabling wider bandwidth of operation..... 86
Figure 7.8	(a). Left: 2mm× 2mm CMOS chip. (b). Optical microscopic image of the CMOS Vibration Sensor..... 88

Figure 7.9	(a). Right: Trench created by laser on the back-side of the CMOS chip (b). Broken sample due to high intensity of laser.....	89
Figure 7.10	SEM view of the CMOS chip thinned down to ~80 μm	90
Figure 7.11	Experimental setup for the suspended thinned down CMOS chip.....	90
Figure 7.12	Measured output voltage for various angles/accelerations of the PCB with respect to the horizon for a silicon n-well piezoresistor.....	92
Figure 7.13	Measured output voltage for various angles/accelerations of the PCB with respect to the horizon for a SiCr piezoresistor.....	92
Figure 7.14	Experimental setup for measuring the effect of vibrations on CMOS vibration sensor.....	93
Figure 7.15	Frequency response of both sensors for 1g of vibration amplitude in the 200-300Hz frequency range.....	93
Figure 7.16	Experimental setup for the suspended thinned down CMOS chip.....	95
Figure 7.17	(a). Static and Frequency response for Sensor I for 1g of vibration..... (b). Static and Frequency response for Sensor II for 1g of vibration..... (c). Static and Frequency response for Sensor III for 1g of vibration.....	95 96 96
Figure 7.18	Shift in resonance frequency due to magnetic and capacitive modulation for Type I sensor.....	98
Figure 7.19	Optical image of the TI fabricated 7mm \times 4mm chip. Side A: Six sensors each having piezoresistors connected in a Wheatstone's bridge fashion having resistors varying from 1k-ohm to 100-kohm. Side B: Identical to Side A along with the addition of vias to increase the effect of stress due to vibrations acting on the piezoresistors. Center: Vibration Spectrometer- five cantilevers with different resonance modes covering a wide range of frequency.....	100
Figure 7.20	COMSOL Simulation showing an increase in stress on the piezoresistor on introductions of trenches around the piezoresistor.....	100
Figure 7.21	Eigenfrequency and mode shapes for 4 integrated cantilevers, each covering a small portion of the targeted frequency spectrum.....	101

Figure 7.22	Post CMOS micro-machining steps for the higher frequency cantilever arrays.....	101
Figure 7.23	SEM view of the post processed higher frequency chip showing the integrated cantilever array.....	102
Figure 7.24	Output voltage vs position on cantilever for different static forces applied to Cantilever 5.....	103
Figure 7.25	Image of the post processed and wire-bonded CMOS cantilevers (high frequency design) along with their response to vibrations at different frequencies. Each cantilever detects and measures the amplitude of vibrations at its resonance frequency where the vibration amplitude is amplified by the cantilever Q-factor.....	104
Figure 7.26	(a). Stress profile for the low frequency CMOS chip using Finite Element Static force analysis. (b). Eigenfrequency and mode shapes for 4 integrated cantilevers, each covering a small portion of the targeted frequency spectrum.....	106

LIST OF TABLES

Table 3.1	Mapping of the linear acceleration binary output to the range of the measured acceleration.....	24
Table 3.2	Measurement results of the linear accelerometer along with the expected values.....	29
Table 3.3	Measurement results of the rotational accelerometer versus the expected values.....	33
Table 4.1	Device Dimensions and electrical parameters of the self-computing coupled switch linear accelerometer.....	40
Table 4.2	Measurement results of the switched coupled accelerometer along with expected values.....	42
Table 5.1	Sensitivity, FOMS, Quality Factor and Sensor Resolution for the Magnetometer at Different Bias Currents.....	57
Table 6.1	Device Properties, dimensions and electrical parameters for the Lorentz force magnetometer.....	70
Table 6.2	Comparison of FM Lorentz Force Magnetometers.....	76
Table 7.1	CMOS MEMS Vibration Sensors Characteristics and Bandwidth of Operation.....	97
Table 7.2	Sensitivity, Q-Factor and bandwidth of operation for the five cantilevers.....	105

CHAPTER 1

INTRODUCTION

1.1 MICRO-ELECTROMECHANICAL SYSTEMS (MEMS)

Micro-Electro-Mechanical Systems, or MEMS, is a technology that in its most general form can be defined as miniaturized mechanical and electro-mechanical elements embedded on semiconductor chips that are made using the techniques of micro fabrication. Their size also makes it possible to integrate them into a wide range of systems. Feature sizes may be made with size on the order of the wavelength of light, thus making them attractive for many optical applications [1]. Microsensors (e.g., accelerometers for automobile air bag deployment and pressure sensors for biomedical applications) and micro-actuators (e.g., for moving arrays of micromirrors in projection systems) [2] are examples of commercial applications of MEMS.

MEMS researchers have demonstrated that many of the micromachined sensors have performed exceptionally better than their macro-scale counterparts. Not only is the performance better but their method of production has an advantage over the same fabrication techniques used in the integrated circuit (IC) industry- which can translate into lower per-unit device production cost. Such miniaturized microsystems thus have the advantage of portability, lower power consumption, less harm to the environment and practically more functionality in a smaller amount of space without any addition of weight. Needless to say, silicon based discrete microsensors found its way into a number of applications which include but are not limited to- accelerometers [3], gyroscopes [4], magnetometers for navigation purposes [5], pressure sensors [6], Inkjet printer heads [7], Pacemakers [8], and for Defense systems (Surveillance, arming and data storage) [9].

The following dissertation focuses on:

- Development of a new class of electromechanical self-computing digital binary output **MEMS accelerometers** or that can be operated directly by a digital processor without the need for an analog front end. Elimination of the analog front end for such digitally operated accelerometers can significantly lower the sensor power consumption by orders of magnitude.
- Achieve ultra-high sensitivities for Lorentz Force resonant **MEMS magnetometers** enabled by internal thermal-piezoresistive vibration amplification and via a mechanical leverage mechanism.
- Design and implement low-power chip scale **CMOS-MEMS vibration sensors** with ~1mg resolution over a wide frequency range of 0-10kHz.

1.2 MEMS ACCELEROMETERS

Inertial sensors are among of the first and most commercially successful MEMS devices. The first MEMS accelerometer was demonstrated in the early 1970's. In the 1990's, MEMS inertial sensors (accelerometers and gyroscopes) revolutionized the automotive air-bag system industry. Gradually, they started to find use in providing signals for stability control and anti-lock braking systems as well. In consumer electronic products such as laptops and smart phones MEMS inertial sensors are used for free fall detection, image stability and auto-screen rotation as well as gesture-based command functions. Micro-machined accelerometers are a highly enabling technology with a huge commercial potential. They provide lower power, compact and robust sensing. Multiple sensors are often combined to provide multi-axis sensing and more accurate data [10]. During recent years, MEMS inertial sensor technology has continued to evolve by entering the area of health care and ambient assisted living [11,12].

Over the past few decades, MEMS accelerometers based on different sensing mechanisms have been demonstrated. Some of the most popular detection mechanisms used in MEMS accelerometers include piezoresistive [13], piezoelectric [14], capacitive [15], and electron tunneling readout [16]. Most commercially successful MEMS accelerometers work based on capacitive detection, which involves measuring the change in the capacitance between stationary electrodes fixed to the substrate and movable electrodes on a suspended mass. The suspended mass, also called the proof mass, must be relatively large (typically in the millimeter range) to have adequate accelerometer sensitivity for most consumer applications. With aggressive power reduction in digital electronics in recent years, MEMS sensors remain one of the most power-hungry components in integrated systems. For example, Lee et al have demonstrated a wireless sensor network (WSN) for monitoring the health and performance of motors which includes MEMS sensors, two signal processors, and the communication modules. The total nominal power consumption of the WSN is as high as 35mW, out of which close to 62% (21.6mW) is the power required for operation of the MEMS sensors, with the wireless link and signal processing unit being responsible for only close to a third of the total power consumption [17].

When it comes to power consumption in MEMS accelerometers specifically, in most commercial accelerometers, an analog-front-end is required to detect and interpret the output. Such circuits (generally switched-capacitor circuits) should be capable of measuring capacitance changes in the femto-Farad to atto-Farad range and turning it into an analog voltage that in most cases needs to be turned into a digital output using an on-board analog to digital converter. This leads to power budget in the few mW to hundreds of μ W range [18-20]. Therefore, by eliminating the analog front end, significant power savings, in some cases close to zero static power

consumption, can be achieved. To achieve very low power consuming MEMS inertial sensors, a fully digital MEMS accelerometer by utilizing the concept of MEMS acceleration switches has been developed. This has been accomplished by designing digitally operated MEMS sensors comprising of acceleration switches that can perform quantitative acceleration measurements with the help of a microprocessor or a digital controller [21-22]. In an effort to further reduce the power consumption of MEMS inertial sensor and eliminate the need for the digital controller, a fully digital self-computing coupled switch MEMS accelerometer has also been developed and demonstrated.

1.3 MEMS MAGNETOMETERS

In simple words, a magnetic sensor is a device that has the capability to detect and quantify magnetic fields. Depending on the magnitude of the measured field, the requirement on the sensitivity is determined-e.g. If the value of the measured magnetic field is greater than the Earth's magnetic field, the sensitivity of the device need not be that aggressive.

Magnetic field sensors have numerous industrial, biomedical, and consumer applications such as Magnetoencephalography [23], Magnetic resonance imaging (MRI), magnetic anomaly detection and munitions fusing for military applications, mineral-prospecting [24], magnetic compass for GPS navigation systems [25], automotive sensors, respiratory measurements [26] and space research [27]. Various magnetic field measurement techniques exist covering different ranges of fields that need to be measured for different applications. Hall Effect sensors are a common category of magnetic field sensors which are capable of measuring magnetic fields in the upper nT to T range. Another category of magnetic field sensors is the Giant Magnetoresistance (GMR) sensor that works based on the principle of anti-ferromagnetic coupling. GMR's are

capable of detecting fields in the sub-micro Tesla range [28]. Fluxgate sensors that work based on the principle of magnetic saturation are quite popular. Although they can measure fields in the upper pT range, their high-power dissipation, large size and narrow operation range limits their use for very specific applications [29]. Search Coils (used widely as metal detectors) [30] and Superconducting Quantum Interface devices (SQUID) [31] also possess the capability to detect extremely small fields, down to the femto-Tesla range. However, search coils are quite bulky and unable to detect static magnetic fields, and SQUIDs on the other hand require cryogenic cooling and have a high sensitivity to electromagnetic interference, thus requiring a sophisticated infrastructure (e.g. liquid helium supply, glass fiber- reinforced epoxy Dewar vessels, and electromagnetic shielding). Sheng et. al have demonstrated a magnetometer with sub-femtotesla resolution by utilizing the principle of Scalar atomic magnetometry [32], the most sensitive magnetic sensor demonstrated to date.

While the above-mentioned magnetometers offer high sensitivities for fields smaller than a few nT's, they are not MEMS compatible and cannot undergo miniaturization. MEMS Magnetometers [33-36] have an edge over the abovementioned conventional counterparts due to their unique features such as small size, low cost, lower power consumption and simplicity of operation. Such properties offer unrivalled advantages, especially when it comes to medical applications, such as magneto-encephalography, where compact arrays of ultra-sensitive sensors are desirable.

Most MEMS magnetometers offering compact size and low cost operate based on measurement of Lorentz force resulting from magnetic fields. Lorentz force is the force acting on a current carrying conductor in presence of a magnetic field. Different detection mechanisms can

be used to turn this force into an electrical signal. One of the main challenges for such sensors is the relatively small amplitude of Lorentz force, especially when targeting magnetic fields in the μT range and below. The Limit of detection (LOD) for such sensors is simply not sufficient for most medical applications, which include detecting magnetic fields in the order of lower pT's to fT's inside the brain (Magnetoencephalography). Therefore, highly sensitive force sensors and/or force amplification mechanisms are required to demonstrate high sensitivities.

Resonant Lorentz force magnetometers are one of the most common categories of MEMS magnetometers that can be implemented on silicon without the need for any special magnetic materials. Hence, unlike magnetoresistive and fluxgate sensors, the external field that needs to be measured does not get distorted (due to hysteresis), thus requiring less sophisticated electronics for measurement. Such devices either make use of structural mechanical force amplification or take advantage of high Quality factors (Q) microscale resonant structures to turn small Lorentz Forces into measurable vibration amplitudes. Resonant systems with high quality factors can achieve large vibration amplitudes when actuated by small actuation forces. The vibration amplitude of a resonator at its resonance frequency is Q times larger than its displacement amplitude resulting from the same actuation force applied as a static force. Therefore, most of the MEMS-based Lorentz Force Magnetometers rely on actuation of a high-Q resonance mode of a MEMS resonator and measuring the resulting vibration amplitude. The vibration amplitude can be detected electronically as an output voltage via capacitive sensing [37,38] or piezoresistive readout [39-40].

A number of other approaches have been reported by researchers to amplify the Lorentz force and thus boost the sensitivity of such sensors. This includes using novel topologies wherein

the magnetometer shaped like a horseshoe was designed to boost the quality factor of the device, thus increasing the sensitivity [41]. Parametric amplification has also been used to increase the force-to-displacement transduction of a resonant sensor via artificially increasing the resonator quality factor through modulation of the spring constant of the device at twice its natural frequency. Sensitivity was amplified by 50X using this approach to $39\text{nT}/\sqrt{\text{Hz}}$ [42]. However, operation of such parametrically amplified devices as practical sensors is quite challenging due to sophisticated electronics required for their operation. Another technique to enhance sensitivity has been achieved by utilizing a multiple loop design for current recirculation in the device [43-44].

The previously demonstrated internal thermal-piezoresistive amplification within a DC biased microscale silicon beam has been used to reach much larger vibration amplitudes for the same Lorentz force actuation, consequently achieving much higher sensitivity [45]. Utilization of the thermal-piezoresistive internal amplification phenomenon to enhance the sensitivity of Lorentz Force MEMS magnetometers has been explained and discussed in Chapter 5.

However, the inherent bandwidth-sensitivity trade-off in an open loop operation (explained in Chapter 5), as well as sensitivity changes due to temperature, have led researchers to explore other techniques for Lorentz Force MEMS magnetometers. By operating the sensor at a frequency slightly lower than the mechanical resonance frequency packaged at a low pressure, the bandwidth- sensitivity concern has been resolved to some extent [46-48]. Alternatively, Lorentz force can be used to modulate the resonant frequency of a MEMS resonator [49,50]. Sensors with frequency modulated output are generally more desirable as frequency measurements offer significantly improved noise and interference robustness and the output can be directly fed to a digital counter without the need for extensive signal conditioning and analog to digital conversion.

However, the benefit of amplification by resonator Q-factor is not available for a frequency output resonant sensor and other means of amplifying the force are to be considered. In [51], the device design was perfected to make use of a fulcrum-lever based micro-leverage mechanism which increased the sensitivity of the sensor by 42X. Yet another method to enhance sensitivity in frequency modulated magnetometers is by utilizing quadrature frequency modulation (QFM), where an external force having the same frequency as, but in quadrature, the self-sustaining force creates a phase shift in the oscillation loop. The phase shift then results in a change in the oscillation frequency, since oscillation always occurs at the frequency that satisfies 0° phase shift around the loop [52].

This dissertation also focuses on a new design for frequency modulated MEMS magnetometers that utilizes a leverage mechanism to amplify the Lorentz force and uses it to distort and therefore modulate the frequency of a dual plate thermally actuated MEMS resonator [49]. Design optimization has been carried out to enhance the sensor's performance further which is discussed in Chapter 6.

1.4 CMOS-MEMS VIBRATION SENSORS

Measurement and spectral analysis of mechanical vibrations is required in various domestic, geophysical and industrial applications such as intrusion detection, identification of mechanical faults in machines, and monitoring structural health [53-55]. Undesirable vibrations can lead to accelerated aging and fatigue which could prove to be detrimental to the life of the machine. In addition, the vibrating mechanisms of most machineries and structures are fundamentally well known, giving rise to the possibility of detecting many faults in accordance with the characteristics of the vibration responses. Vibration responses are processed and

interpreted in a variety of ways such as peak values and variance of the signal in the time domain, and power spectral analysis in the frequency domain [56]. Therefore, monitoring and detecting such vibrations could be crucial for many systems.

State-of-the-art micro fabricated vibration sensors based on capacitive [57] and piezoelectric mechanisms [58] have undergone several advances. Vibration sensed via piezoelectric mechanisms are accurate and reliable but are difficult to integrate with existing foundry processes, difficult to mass produce and have high source impedance, due to which their signals need to be carefully amplified. Also, piezoelectric vibration sensors provide an output transient charge in response to stress and therefore their detection at lower frequencies – especially DC – is challenging (extremely small currents). Capacitive sensors have the advantage of no exotic materials, low noise, and compatibility with CMOS readout electronics. However, since very small changes in capacitance are detected, such systems require a sophisticated analog front end and are incapable of handling high frequency measurements above $\sim 200\text{Hz}$. Other mechanisms to sense vibrations include geophones [59], tunneling [60-61], and optical sensors [62-63]. Vibration sensors based on tunneling mechanisms are shown to have low noise floor, but due to the small allowable displacement at the tip require a very stiff feedback loop, which reduces the useful bandwidth and dynamic range. Existing vibration sensors are also discrete elements with relatively large sizes ($\sim 1\text{cm}$) and require supporting electronics.

The piezoresistive effect that operates on the principle that the electrical resistance changes with deformation is an alternative phenomenon that can be utilized to overcome such challenges, especially when it comes to integration with CMOS technology. N-well piezoresistive gauges [64, 65] are usually insensitive to environmental degradation, are easily available in any existing

CMOS technology, are easy to miniaturize and package and have a straightforward detection mechanism. Depending on the particular semiconducting material properties, piezoresistive effects allow direct and convenient signal transduction methods for electrical and mechanical properties.

Currently, no low cost, low power, and compact vibration sensor solution exists that can provide frequency distribution data for the measured vibrations. In this dissertation, building blocks of a low-power miniaturized vibration spectrum analyzer with a resolution of 1mg over a wide frequency range (0-10kHz) using an existing Texas Instruments CMOS process has been built and implemented, without adding any complex post processing fabrication steps.

The dissertation is organized in 8 chapters. The outline of the chapters is given below:

Chapter 1: Discusses the importance of MEMS technology and introduces the sensors covered in the dissertation- MEMS Accelerometers, MEMS Magnetometers and CMOS-MEMS Vibration Sensors.

Chapter 2: Discusses the operating principle for a new digital output inertial sensor along with initial characterization efforts.

Chapter 3: Presents the implementation of the acceleration switch sensors for low power, binary output linear and rotational accelerometers with the use of a digital controller.

Chapter 4: Takes the project one step further to eliminate the digital controller and show as a proof of concept, a zero-static power self-computing binary output accelerometer.

Chapter 5: Discusses the operating mechanism and results for sensitivity enhancement of an amplitude modulated Lorentz force MEMS magnetometer via internal thermal piezoresistive amplification phenomenon.

Chapter 6: Addresses problems associated with amplitude modulation and presents a new design for sensitivity enhancement of frequency modulated Lorentz Force MEMS Magnetometers.

Chapter 7: Discusses design, optimization, fabrication and measurement results for building blocks of a low power, wideband vibration spectrum analyzer.

Chapter 8: Briefly summarizes the contributions of this dissertation and gives recommendations for future direction.

CHAPTER 2

ULTRA-LOW POWER DIGITALLY OPERATED MEMS ACCELEROMETERS¹

2.1 PRINCIPLE OF OPERATION

Acceleration switches are simple devices with an output that can be high (ON) or low (OFF) depending on the predetermined acceleration threshold of the device and the acceleration the device is subjected to [66]. Most acceleration switches are comprised of a suspended mass anchored to a substrate with flexible tethers. If the device is subjected to an acceleration higher than its threshold value, the suspended mass will come in contact with a fixed electrode closing the circuit and signaling that the acceleration threshold has been reached. Hence, such devices require close to no power for operation and their output can be directly fed to a digital processor without any further processing. However, an acceleration switch can only indicate whether the applied acceleration is higher or lower than the set threshold and cannot provide quantitative information about how much acceleration is applied to the device at each moment. In fact, an acceleration switch can be referred to as a single bit digital accelerometer. However, since a threshold accelerometer triggers at a single threshold, an array is necessary to cover a wide acceleration range [67-70] making implementation of high resolution accelerometers extremely complex.

A variety of acceleration switches have already been demonstrated for various applications like air-bag activation in automobiles [71] and shock monitoring systems [72]. Tunable

¹©2015 IEEE. Portions Adapted, with permission, from V. Kumar, X. Guo and S. Pourkamali, “Single-Mask Field Emission Based Tunable MEMS Tunneling Accelerometer”, IEEE Nano, May 2015.

acceleration switches using the concept of pre-stressed bimorph micro-beams have been reported wherein the gaps between the bimorph beam and fixed electrode can be varied by adjusting the ‘snap-on’ voltage [73]. In [74], a set of comb drives has been utilized to increase the gap size and thus increase the acceleration threshold of the device.

The following section focuses on the initial characterization effort for such designs using tunneling current as a mechanism for detecting the acceleration range. The above-mentioned concept of acceleration switches (based on contact) has also been utilized to develop both linear and rotational digital MEMS accelerometers with and without the need for a digital controller (micro-processor) which will be discussed in Chapters 3 and 4.

2.2 MEMS TUNNELING ACCELEROMETER

2.2.1 BACKGROUND AND MOTIVATION

Simmons et. al. [75] developed a model for the description of the current-voltage behavior of tunneling junctions. As per the model, electron tunneling can only be observed when the applied bias is smaller than the barrier height. In other words, electron tunneling exists only when the gap between electrodes is nearly the order of 10 Å. A feedback loop is required to maintain a constant tunneling gap between the tip and the electrode. The current-voltage relationship for such a system is given by:

$$I_t \propto V_b \exp(\alpha_i \sqrt{\varphi} x_{tg}) \quad (2.1)$$

Where I_t is the Tunneling Current, V_b is the Tunneling Bias Voltage, α_i is a constant (1.025 Å-1eV-0.5), φ is the Effective height of tunneling barrier and x_{tg} is the gap between the probe tip

and the counter electrode. One of the challenges for the operation of a sensor in the direct tunneling mode is the fabrication process where the gaps need to be fabricated in the order of Å.

In the other case when the applied bias exceeds the barrier height, the electron transport mechanism changes from direct tunneling to field emission (cold emission) tunneling, the Simmons Equation for such a regime can be written as:

$$\ln\left(\frac{I}{V^2}\right) \propto \frac{-4d\sqrt{2m}\phi^2}{3hq} \frac{1}{V} \quad (2.2)$$

where I is the tunneling current, V is the tunneling bias voltage, d is the gap between tip and counter electrode, m is the Electron Effective Mass, and ϕ is the Effective height of tunneling barrier. It is evident from the equation that in case of the field emission mechanism, $\ln(I/V^2)$ depends linearly on I/V for a fixed gap. A change in the gap between the electrode tip and the counter electrode due to acceleration modulates the tunneling current passing through the gap. The change in tunneling current can be measured to determine the acceleration.

2.2.2 DEVICE DESCRIPTION AND FABRICATION

Monocrystalline silicon with a relatively thick coating of gold was used as the structural material for the accelerometers. Figure 2.1 shows the fabrication process used to fabricate the devices on an SOI substrate having a 15 μm thick device layer and 1μm thick buried oxide layer. The fabrication procedure utilizes a two-mask micromachining process. The accelerometer silicon skeleton was first defined in the SOI device layer via deep reactive ion etching (DRIE) all the way down to the buried oxide layer as shown in Figure 2.1(a). The substrate backside was then patterned and etched to avoid any potential stiction issues for the large proof masses. Devices were then released by removing the buried oxide layer in hydrofluoric acid (HF) as shown in Figure

2.1(b). To further narrow down the gap between the proof mass and the output electrode tip, a thick layer of gold with slight sidewall coverage was sputtered on the fabricated devices. The sputtered gold on the sidewalls also provides a high-quality metal-metal electrical contact between the proof mass and the output electrode tip (Figure 2.1(c)). Thickness of the deposited gold on the sidewalls was thoroughly monitored to adjust the gap size between the contact tip and the proof mass in the deep submicron range without the need for nanolithography or any sophisticated processing.

The fabricated accelerometer as shown in Figure 2.2 consists of three parts: the tuning and the tunneling electrode (E1 and E2 respectively), the proof mass that is connected to electrode E1 and an array of parallel plate electrostatic actuators ($200\mu\text{m} \times 5\mu\text{m} \times 15\mu\text{m}$ each) that control the gap between the tip and the counter electrode as shown in Figure 2.2. By varying the voltage between the tip and the counter electrode as shown in Figure 2.2. By varying the voltage between the proof mass and the actuator electrodes, the gap between the two tunneling electrodes

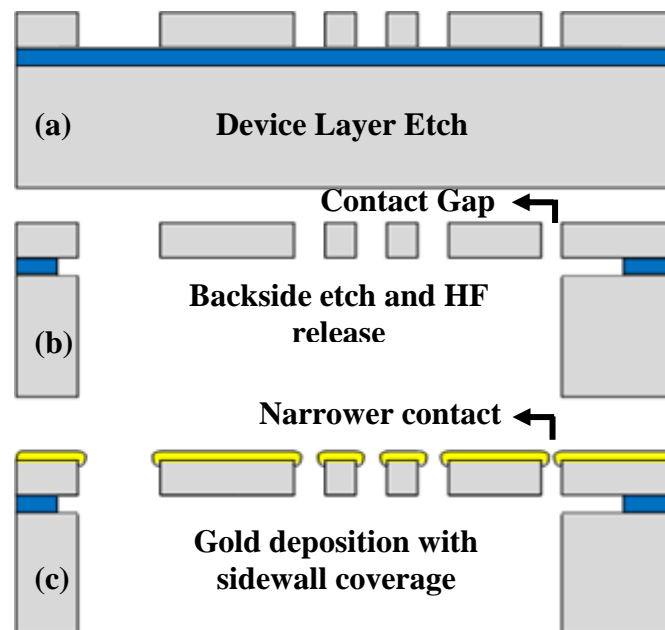


Figure 2.1. Schematic cross-sectional view of the process flow for the fabrication of the accelerometer.

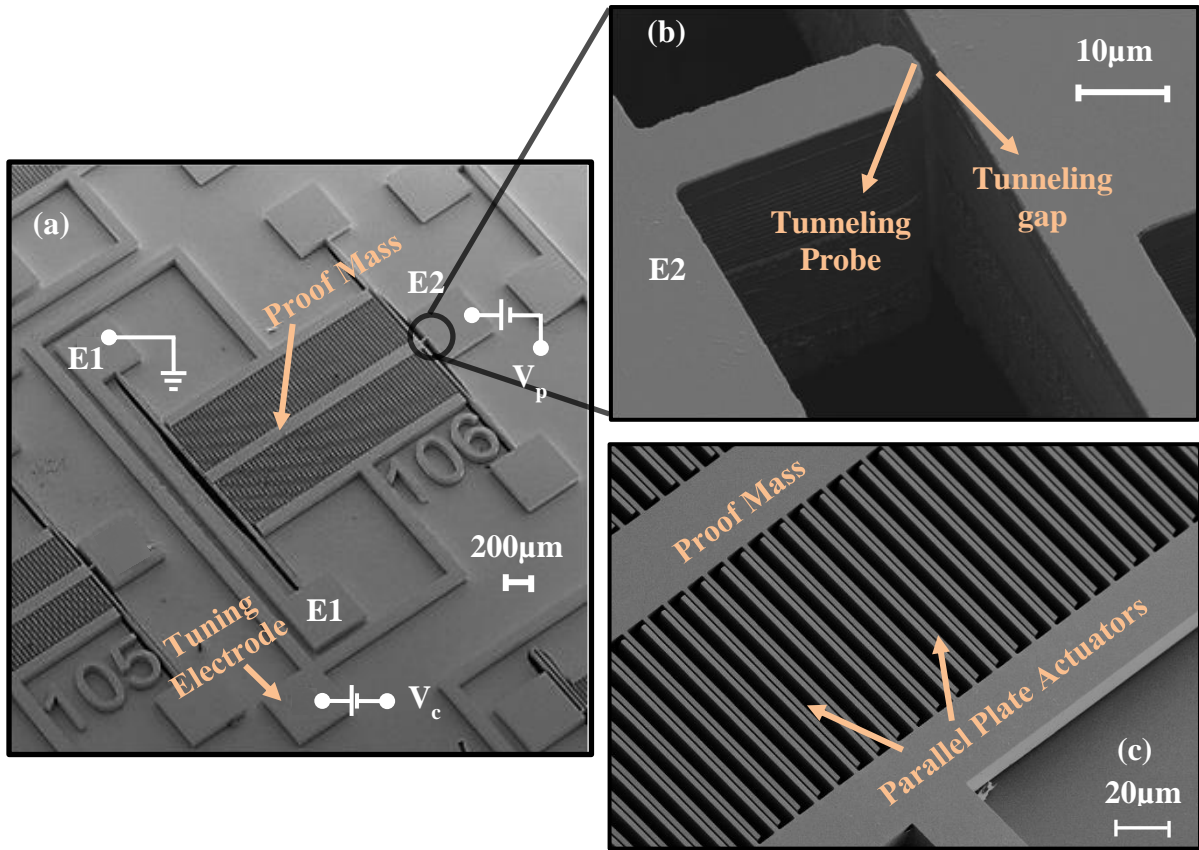


Figure 2.2.(a). SEM View of the Tunneling Current Accelerometer.
 (b). Zoomed-in view of the gap between the tip and the counter electrode.
 (c). SEM view of the tunable electrodes.

can be controlled. The application of a bias voltage between the two tunneling electrodes causes a tunneling current to flow through the nanoscale gap. A change in the gap between the electrode tip and the counter electrode due to acceleration of the proof mass modulates the tunneling current passing across the nanoscale gap.

2.2.3 MEASUREMENT SETUP AND RESULTS

To test the device of Figure 2.2 as a Field Emission Mode Tunneling Accelerometer, the device was wire bonded on to a PCB and two independent bias voltages were applied simultaneously to the electrode array (V_c) and the tunneling probe electrode (V_p) (Figure 2.3) with

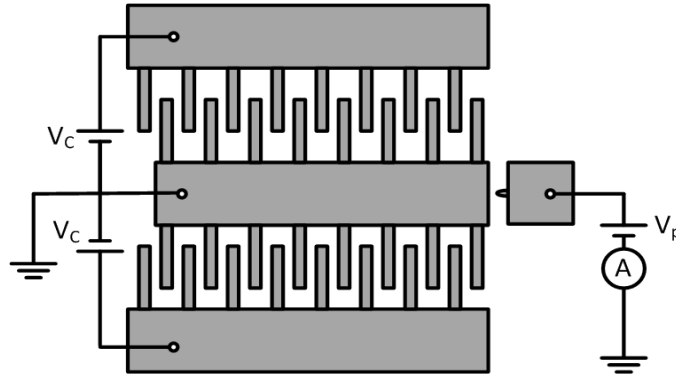


Figure 2.3. Schematic view of the test setup electrical connections.

the accelerometer body grounded. The bias voltage applied to the parallel plate actuators, V_c , controls the gap between the probe and the counter electrode (proof mass). The current voltage characteristics of the accelerometer were plotted by varying the bias voltage between the tunneling electrodes for a fixed gap. The current and thus resistance of the gap was also measured by varying the gap for a fixed bias voltage. To subject the device to different accelerations and study the effect of acceleration on the gap and therefore tunneling current, the PCB was tilted to various angles with respect to the horizontal direction. The resulting acceleration at each angle can then be calculated by $a = (g/\sin \varphi)$ where g is the acceleration due to gravity and φ is the angle between the device and the horizontal surface on which it rests.

Figure 2.4 shows the current-voltage characteristics of the tunneling gap for a fixed gap of $\sim 43\text{nm}$ which was achieved by applying a voltage of 9V to the parallel plate electrodes (V_c). The final gap size was determined by subtracting the displacement that occurred due to the application of V_c from the total gap size as seen in SEM pictures. From the linearity of the $\ln(I/V^2)$ versus $1/V$ graph, it is evident that the sensor follows the Fowler Nordheim tunneling theorem thus

proving the existence of a field emission tunneling current across the gap upon application of the bias voltage. A maximum current of 12.5 μA was obtained for a bias voltage of 6V.

To investigate the dependence of the tunneling current to the gap and the probe bias voltage independently, the gap between the tip and the counter electrode was varied by varying V_c while the bias voltage V_p was kept constant at 5.35V. The experiment was repeated for different values of V_p (5.35V-6.85V) and the results are illustrated in Figure 2.5. Figure 2.6 shows the tunneling

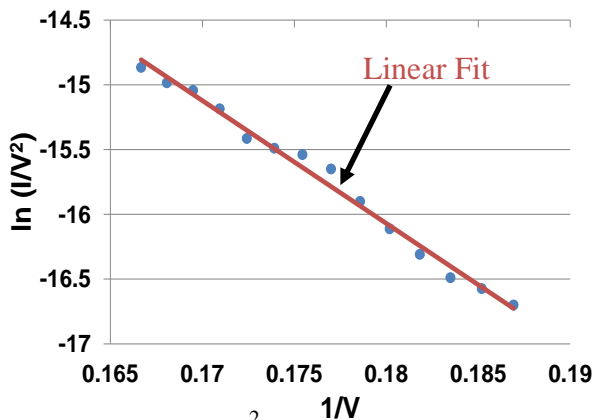


Figure 2.4. $\ln(I/V^2)$ versus $1/V$ plot depicting linearity of the Fowler Nordheim Theorem fitted with a straight line.

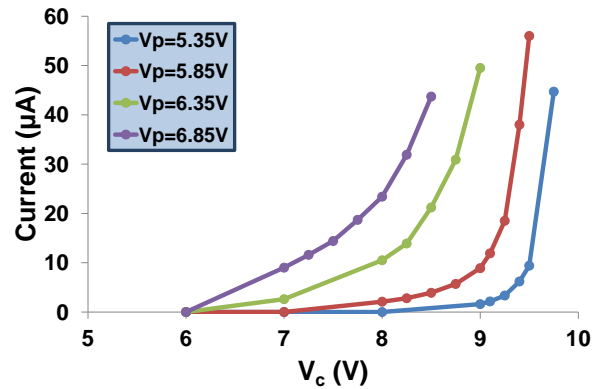


Figure 2.5. Tunneling current versus gap voltage for different probe bias voltages.

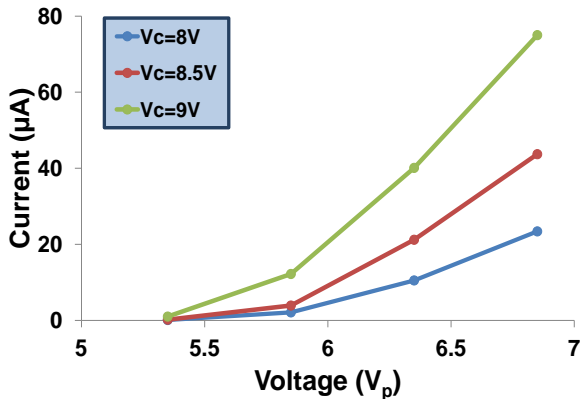


Figure 2.6. Measured tunneling current for different probe bias voltages having constant gap control voltage.

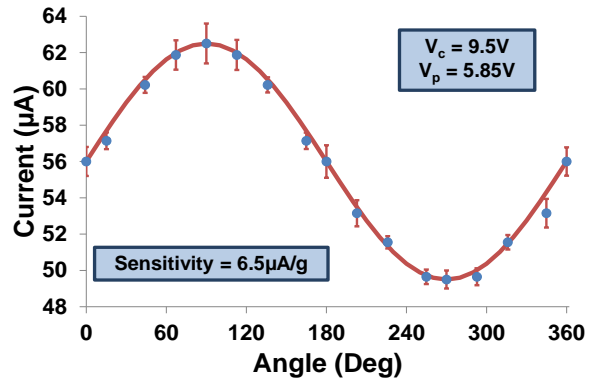


Figure 2.7. Measured tunneling current for different accelerations due to variation in tilt angle of the device.

current amplitudes for different probe bias voltages at a fixed gap. The PCB was then tilted to various angles, thus causing the tunneling gap to change due to the gravitational force acting on the proof mass of the structure. Figure 2.7 shows the variation in tunneling current due to variation in the acceleration due to the tilt of the setup. A sensitivity of $6.5 \mu\text{A/g}$ has been achieved for the accelerometer in the field emission mode for a gap of $\sim 40\text{nm}$.

In brief, a tunable MEMS tunneling accelerometer based on the field emission principle was demonstrated. The other purpose in doing so was to characterize the accelerometer structure parameters like tether stiffness, reliability, fabrication tolerances on the widths of the beams, and capacitive gaps to understand and implement them in the design for binary output accelerometers discussed in the next chapter.

CHAPTER 3

BINARY TUNABLE INERTIAL SENSORS WITH USE OF DIGITAL CONTROL^{2,3}

3.1 LINEAR ACCELEROMETER

3.1.1 DEVICE DESCRIPTION

Figure 3.1 shows a simplified schematic view of a single axis 3-bit accelerometer operating based on the principle of acceleration switches with digitally tunable threshold. The structure consists of a number of electrostatic tuning electrodes that can apply an assistive force to the proof-mass, thus changing its acceleration threshold over a wide range. The bulky proof mass moves back and forth in the horizontal direction because of the applied acceleration. The proof mass is

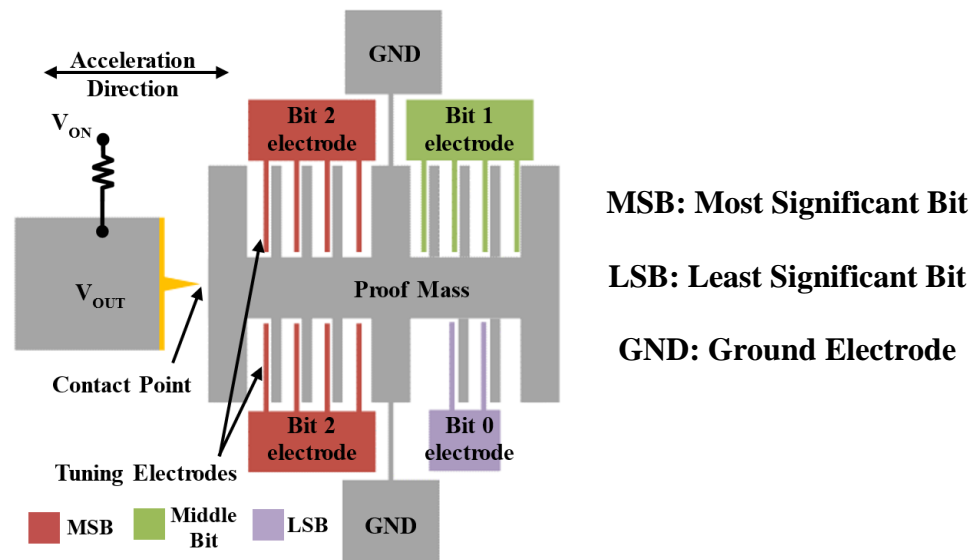


Figure 3.1. Simplified schematic view of a 3-bit digitally operated accelerometer.

²©2016 IEEE. Portions Adapted, with permission, from V. Kumar, R. Jafari and S. Pourkamali, “Ultra-Low Power Digitally Operated MEMS Accelerometer”, IEEE Sensors Journal, Vol 16, Issue 24, Dec 2016.

³©2017 IEEE. Portions Adapted, with permission, from V. Kumar, A. Ramezany, S. Mazrouei, R. Jafari and S. Pourkamali, “A 3-bit digitally operated MEMS rotational Accelerometer” IEEE MEMS, Jan 2017.

connected to ground (GND). The stationary output electrode V_{OUT} which is biased with a bias voltage (V_{ON}) through a large resistor has a metallic tip that comes in contact with the proof mass once the acceleration exceeds the threshold, hence setting the output electrode voltage to zero. Application of an assistive force to the electrostatic tuning electrodes which pulls the proof mass towards the metallic tip will lower the acceleration threshold (and thus the gap between the proof mass and the metallic tip) and vice versa. In this manner, having an arrangement of multiple electrostatic actuators with appropriate electrode finger size and number around the proof mass and selectively turning them ON or OFF, a binary search can be performed to find the value of the applied acceleration. The accelerometer utilizes a MEMS acceleration switch with a number of electrostatic tuning electrodes that can tune the gap size changing its acceleration threshold over a wide range and add digital control ability via electrostatic tuning to turn them into multi-bit digital accelerometers.

3.1.2 DESIGN CONSIDERATIONS

The mass of the proof mass and stiffness of the tethers should be chosen in a way that when the device is subjected to full-scale acceleration and all the electrode voltages are set to zero, the proof-mass displacement is equal to the gap size between the metallic tip and the proof mass, i.e.,

$$K x = m A_{fs} \quad (3.1)$$

where K is the overall stiffness of the tethers, x is the gap size between the metallic tip and the proof mass, m is the mass of the proof mass and A_{fs} is the full-scale acceleration.

The other design component for such devices is the electrostatic electrodes. The main challenge in working with such electrostatic electrodes is that the forces and thus the displacements

generated by them are very small for small bias voltages. The parallel-plate electrostatic force is given by:

$$F = \frac{n\varepsilon AV^2}{2d^2} \quad (3.2)$$

where n is the number of electrodes, ε is the permittivity of free space (8.854e-12 F/m), A is the electrode area, V is the bias voltage and d is the electrostatic gap size. Larger forces can thus be generated by having multiple electrostatic electrodes and larger electrode area for tuning the gap size and thus, the acceleration range. Parallel plate actuators are highly nonlinear and get pulled in and snap together when the displacement resulting from application of the bias voltage, is more than one-third of the initial gap size. Therefore, the electrostatic gap size d should at least be 3X larger than the metal-electrode gap x in order to avoid severe nonlinearity and pull-in.

3.1.3 DESIGN SPECIFICATIONS

The actuator associated with the most significant bit (MSB), which is Bit 2 in this case (Figure 3.1), has twice the number of identical parallel plate actuator fingers compared to the next most significant bit (Bit 1). In other words, the combined Bit 2 electrodes in Figure 3.1 provide an actuation force which is exactly twice that of Bit 1 electrode when turned on. Similarly, the number actuator fingers go down by a factor of two from each more significant bit to the next less significant bit and the least significant bit (Bit 0) has the minimum number of actuator fingers. Therefore, in a 3-bit design, if the MSB actuator is designed to have 8 electrode fingers, the middle bit will have 4 finger electrodes (2X smaller than MSB) and the LSB actuator will have 2 finger electrodes (4X smaller than the MSB). The number of electrodes, electrostatic actuator gap size, and electrode areas are to be chosen so that upon application of the ON voltage to the MSB actuator, a force equal to 50% of the full-scale acceleration force is applied to the proof mass.

3.1.4 BINARY SEARCH FOR ACCELERATION MEASUREMENT

Figure 3.2 shows a sample flow-chart for performing a binary search in the previously explained 3-bit accelerometer. The binary search to find the acceleration begins by activating the MSB electrode (Bit 2 electrode), i.e., biasing it with a predetermined voltage. This effectively reduces the gap size between the proof mass and the metallic tip and lowers the acceleration threshold of the switch to $0.5A_{fs}$. If the switch closes when the MSB is activated, i.e., the proof mass and the metallic tip come in contact due to the activation of MSB alone, the acceleration is larger than 50% of the full-scale acceleration. In this case, the first digit (MSB) in the binary acceleration output is “1”. In this case, the MSB electrode is turned OFF and the next bit, Bit 1 electrode, is turned ON. Now, if the Bit 1 electrode alone is enough to keep the switch closed, the

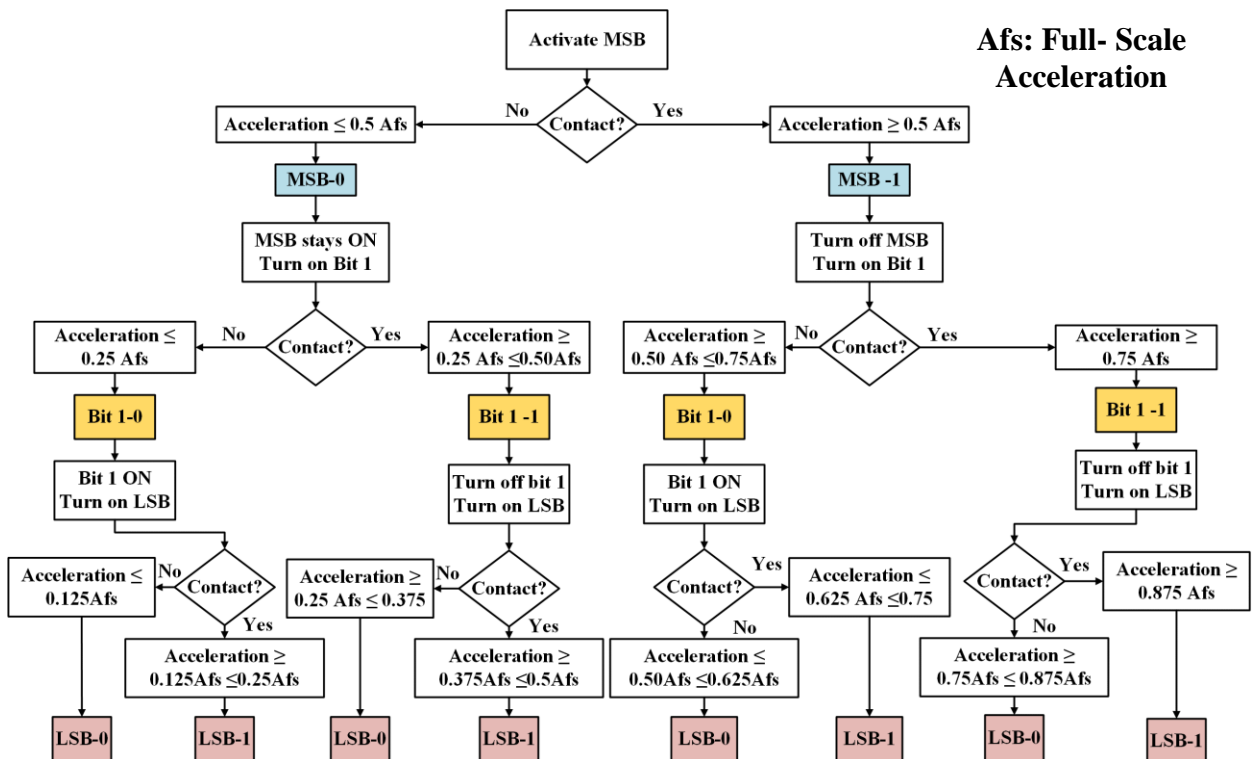


Figure 3.2. Flowchart showing algorithm for binary search in a 3-bit digital accelerometer.

acceleration is above or equal to 75% of the full-scale acceleration and the second digit (Bit 1) in the binary acceleration output will be “1” as well. If there is no contact, the acceleration would be between 50% and 75% of full scale acceleration and Bit 1 in the binary output would be “0”. In this case, Bit 1 electrode stays “ON” and the LSB electrode (Bit 0 electrode) is now activated. If activation of this electrode closes the switch, the acceleration would be between 62.5% and 75% of full scale acceleration, i.e., a binary output of “101”. If not, the acceleration would be between 50% and 62.5% of full scale acceleration (binary output of “100”). In the case where the Bit 2 electrode doesn’t initiate contact, the MSB bit in the response is “0” and the associated electrode stays “ON” while the electrode associated with the next bit is activated. If with all actuators ON, contact still does not occur, then acceleration applied to the device is below 12.5% of full-scale

Table 3.1. Mapping of the linear Acceleration Binary Output to the Range of the Measured Acceleration.

MSB	Bit 1	LSB	Acceleration Range
0	0	0	$a \leq 0.125A_{fs}$ *
0	0	1	$0.125A_{fs} \leq a \leq 0.25A_{fs}$
0	1	0	$0.25A_{fs} \leq a \leq 0.375A_{fs}$
0	1	1	$0.375A_{fs} \leq a \leq 0.5A_{fs}$
1	0	0	$0.5A_{fs} \leq a \leq 0.625A_{fs}$
1	0	1	$0.625A_{fs} \leq a \leq 0.75A_{fs}$
1	1	0	$0.75A_{fs} \leq a \leq 0.875A_{fs}$
1	1	1	$a \geq 0.875FSg$

* A_{fs} : Full-Scale Acceleration

and the binary output is “000”. The mapping of the binary output of such a 3-bit accelerometer to the applied acceleration is as shown in Table 3.1. The same concept and operation procedure can be enhanced to higher number of bits to realize accelerometers with higher resolutions, e.g. 4-bit, 8-bit, etc.

3.1.5 DEVICE FABRICATION

Device fabrication for the sensors remains the same as explained in Section 2.2.2. Figure 3.3 (a), (b) and (c) show SEM views of the accelerometer structure fabricated using the described fabrication sequence. Regular lithography and plasma etch constraints restrict the gap size between the proof mass and the metallic tip to $\sim 1.5\mu\text{m}$. By depositing a thick layer of gold with side wall coverage, gap sizes as small as 270 nm were achieved as shown in Figure 3.3(c).

In the current design, eight identical electrostatic actuator finger sets are included in the device shown in Figure 3.3(a) allowing operation of the device as a 3-bit accelerometer with 4 of the electrode sets associated with the most significant bit, 2 electrode sets for the middle bit and 1 electrode set for the least significant bit while the remaining electrode could be used for tuning the device operating range.

3.1.6 MEASUREMENT SETUP AND RESULTS- DETERMINATION OF ELECTRODE VOLTAGES

For the specific device tested in this work, due to the relatively small proof mass ($5.5\text{e-}9$ Kg) and high stiffness of tethers (~ 5 N/m), a very high bias voltage would be required to bring the proof mass in contact with the output electrode for accelerations less than 1g that could easily be applied to the device by tilting it. The alternative is to use sophisticated high-g test equipment for lower bias voltages. Due to the unavailability of such equipment and for ease of measurement, five

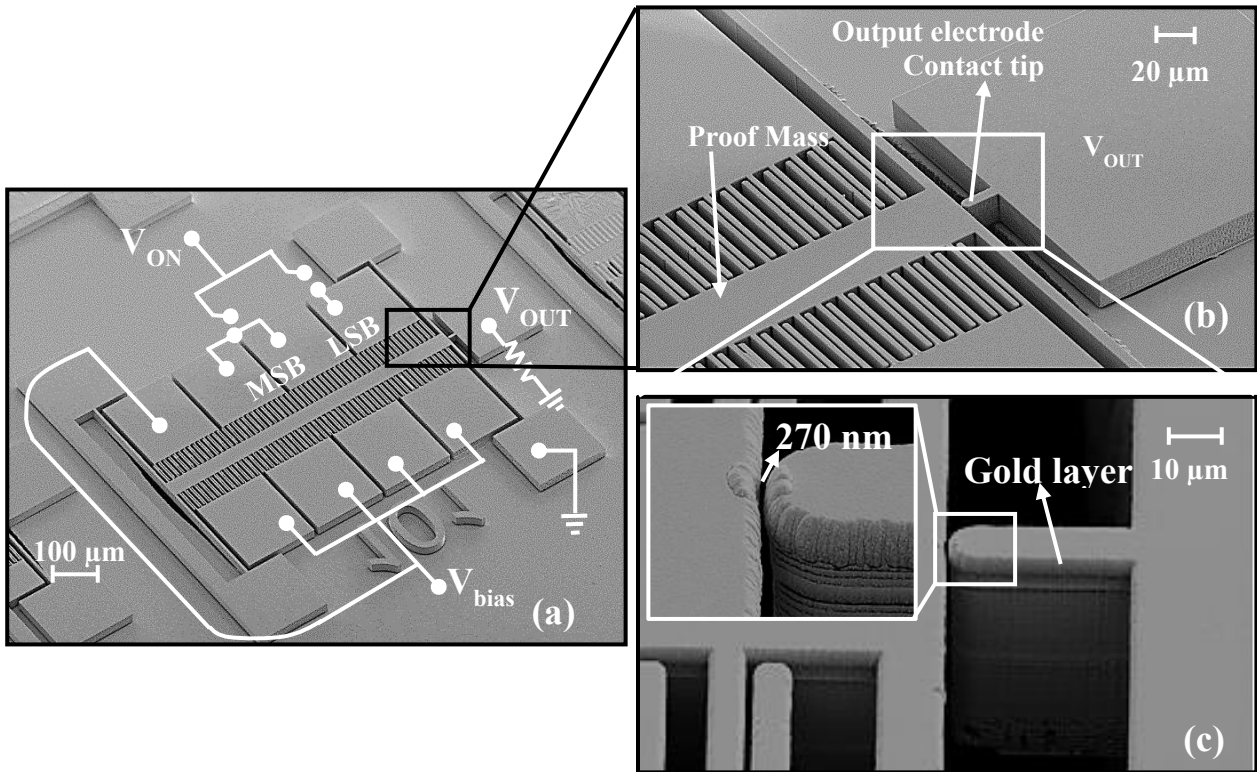


Figure 3.3. (a). SEM view a fabricated digital accelerometer also showing device electrical connections for testing its performance;
 (b). Zoomed in view of the output electrode tip area and the parallel plate actuators;
 (c). Zoomed-in side view of the gap between the proof mass and the output electrode showing the gap narrowed down by gold deposition.

of the available eight actuators were used as tuning electrodes to bring the proof mass closer to the output electrode tip and the full-scale acceleration of the device was set to 1.33g. This effectively altered the design from a 3-bit accelerometer to a 2-bit accelerometer in which five of the electrode sets were used as tuning electrodes, two of the electrode sets were used as the MSB electrodes and the remaining electrode was used as the LSB electrode.

To calibrate the device for a 0-1.33 g operation, i.e., to determine the bias voltages for the electrodes, the device was placed on a printed circuit board and subjected to an acceleration of 1g, which is the acceleration required for a “11” output. In order for the proof mass to make contact

to the fixed electrode at 1g, the gap size needs to be reduced to $\sim 12\text{nm}$ (based on the tether stiffness and mass of proof mass). The voltage that needs to be applied to the five electrodes to tune the gap size from $\sim 270\text{nm}$ to $\sim 12\text{nm}$ is calculated to be $\sim 52\text{V}$. On measurement, a bias voltage (V_{bias}) applied to the 5 tuning actuators was gradually increased until contact was detected between the proof mass and the metallic tip. It was determined that by applying a voltage (V_{bias}) of 47.2V to each of the five actuators (Figure 3.3(a)), which closely agrees with its theoretical value. This small variation in the theoretical and measured value could be attributed to the fact that the gold deposition added more mass to the device and reduced the gap size between the capacitive electrodes as well. In this case, while the other 3 actuators are OFF, an acceleration of 1g would bring the proof mass in contact with the output electrode. The contact was identified by monitoring the current at the output electrode. A very large resistor was connected from the output electrode to ground to avoid high currents flowing through the device upon contact. The minimum voltage of the tuning electrodes required to achieve contact under 1g is the bias voltage to be maintained during device operation. The device was then subjected to an acceleration of 0.66g , which is half the full-scale acceleration, with the bias voltages to the five electrodes turned “ON”. Since the applied acceleration is less than 1g, there will be no contact between the proof mass and the metallic tip. With the tuning voltage V_{bias} left “ON”, another independent bias voltage (V_{ON}) was applied to the two MSB electrodes, and the voltage was gradually increased to detect contact at the output electrode. Once again when the contact was observed, the voltage corresponding to contact (5.7V) was determined to be the operating voltage for the MSB electrodes. Since the LSB actuator has exactly half the number of fingers as that of the MSB, the voltage given to the MSB electrodes required for making contact would be the same as the voltage needed by the LSB

electrode to make contact at 0.33g when the MSB electrode is kept “ON”, i.e., 25% of full scale acceleration. Thus, to validate the pre-determined voltages, the voltage found for the MSB electrodes was given to the LSB electrode with the other 7 electrodes turned “ON” as well. Upon application of an acceleration of 0.33g, contact was observed, thus validating all of the pre-determined voltages. After determining the bias and operating voltages, the device shown in Figure 3.3(a) was tested in the zero to 1g range simply by tilting the Printed Circuit Board to various angles with respect the horizontal direction. This sets the “11” binary output of the accelerometer to 1g, i.e., full-scale acceleration of 1.33g.

Device performance was validated by monitoring the output while turning different bits ON or OFF as followed in the flowchart shown in Figure 3.4. For the device tested in this work, the control signals for altering the states of the MSB and LSB were applied manually instead of using a controller for its operation. Results of the above-mentioned tests are tabulated in Table 3.2 showing that the device can distinguish between acceleration in the ranges of 0-0.38g (00 binary output), 0.38g-0.67g (01 binary output), 0.67g-1g (10 binary output), and $\geq 1g$ (and 11 binary output), which are very close to the theoretically expected ranges. Although the device has a full-scale acceleration of 1.33g and was never tested at accelerations higher than 1g, the transition point from output of 10 to 11, which is to occur at 1g (75% of full-scale), was successfully detected. Also, it should be noted that the MSB, LSB (State) values in Table 3.2 indicate the required ON/OFF state for the two actuator electrodes to maintain contact over the associated acceleration range. The binary acceleration output of the sensor that is to be provided by the digital processor is the exact opposite of the MSB, LSB actuator state.

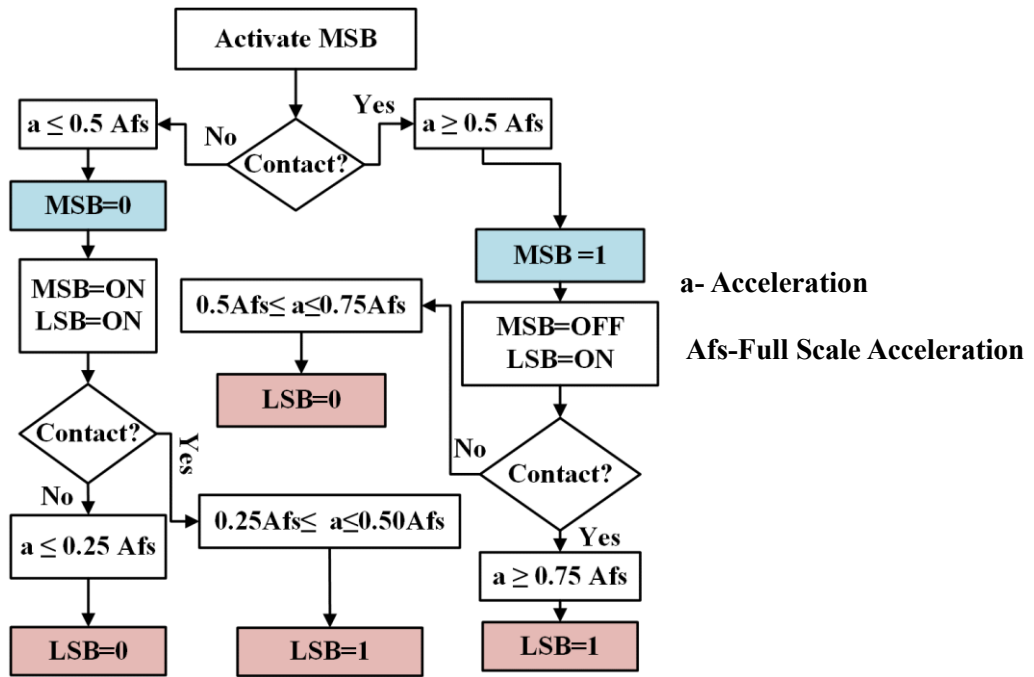


Figure 3.4. Flowchart showing algorithm for binary search in a 2-bit digital accelerometer.

Table 3.2. Measurement results of the linear accelerometer along with the expected values.

MSB, LSB (State)	Acceleration (Theoretical) (g)	Acceleration (Measured) (g)	Binary Acceleration Output
00	≥ 1	≥ 1	11
01	$1 \geq g \geq 0.66$	$1 \geq g \geq 0.67$	10
10	$0.66 \geq g \geq 0.33$	$0.67 \geq g \geq 0.38$	01
11	$0.33 \geq g \geq 0$	$0.38 \geq g \geq 0$	00

3.1.7 OPERATING POWER CONSUMPTION

The device itself is just a passive switch operating as a result of the acceleration it is subjected to. In addition to the power consumed by the MEMS sensor, the digital processor

responsible for turning “ON” and “OFF” the electrodes will require some power for its operation as well. During each measurement cycle, each actuator or electrode needs to be turned “ON” once. The overall electrode capacitance for all the eight electrodes in the device shown in Figure 3.3(a) is calculated to be 0.62pF. Assuming a conservative scenario where each electrode has 1pF of parasitic capacitance along with it, the total capacitance to be charged up to the system operating voltage and eventually depleted during each measurement cycle is 8.62pF. With an operating voltage of 5V, the required energy for each measurement cycle would only be 108pJ. For taking 100 measurements per second, i.e., a sampling rate of 100Hz, the consumed energy for operation of the sensor will be 10.8 nW of power consumption only, which is orders of magnitude lower than the power budget for a regular Analog front end for MEMS accelerometers.

3.2 ROTATIONAL ACCELEROMETERS

3.2.1 DEVICE DESCRIPTION

Figure 3.5 shows an alternative rotational mode structure that can be used as a gyroscope. As opposed to well established MEMS gyroscopes that provide an output proportional to the rotation rate, the output of this gyroscope is proportional to the rotational acceleration (time derivative of rotation rate). When the substrate of such device is subjected to a rotational acceleration, the suspended massive ring will slightly lag by bending the tethers due to its mass inertia. As a result, if the rotational acceleration is large enough, the metallic tip and stationary output electrode will contact each other setting the output voltage to “high”. Similar to the previously discussed accelerometer design, electrostatic forces from closely spaced parallel plate electrodes can tune the acceleration threshold of the device and be used to determine the applied acceleration via the same discussed strategy (by turning them ON and OFF one by one and

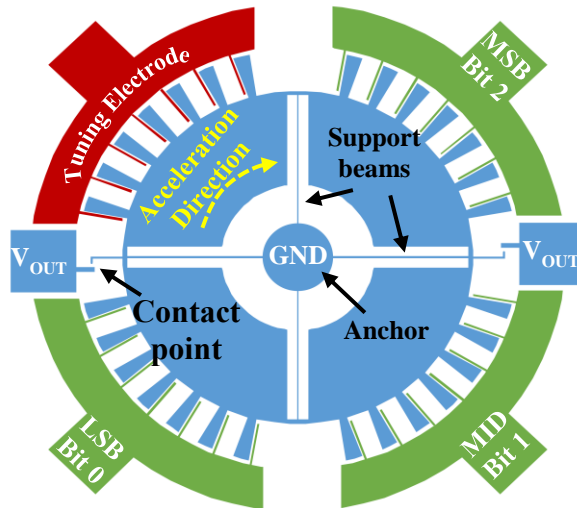


Figure 3.5. Simplified schematic of the 3-bit digitally operated rotational accelerometer.

performing a binary search). The output of such gyroscope should be integrated twice to provide angular position information (as opposed to mainstream gyroscopes requiring only one integration), which is undesirable and could lead to extra errors.

3.2.2 DEVICE FABRICATION

Device fabrication for the sensors remains the same as explained in Section 2.2.2. Figure 3.6 shows SEM views of the rotational accelerometer fabricated using the described fabrication sequence. Four identical electrostatic actuator finger sets (six $100\mu\text{m} \times 10\mu\text{m} \times 35\mu\text{m}$ fingers on each set) surround the silicon proof mass ($\sim 1\text{mm}$ in diameter) in the device shown in Figure 3.5 allowing the operation of the device as a 3-bit accelerometer. Three of the four electrode finger sets are associated with the most significant bit (MSB), the middle bit (MID) and the least significant bit (LSB), while the remaining fourth electrode set (tuning electrode) could be used for tuning the device operating range. A $1.5\mu\text{m}$ gap between the proof mass and the metallic tip was obtained after the mask-less sputtering the 200nm gold onto the device.

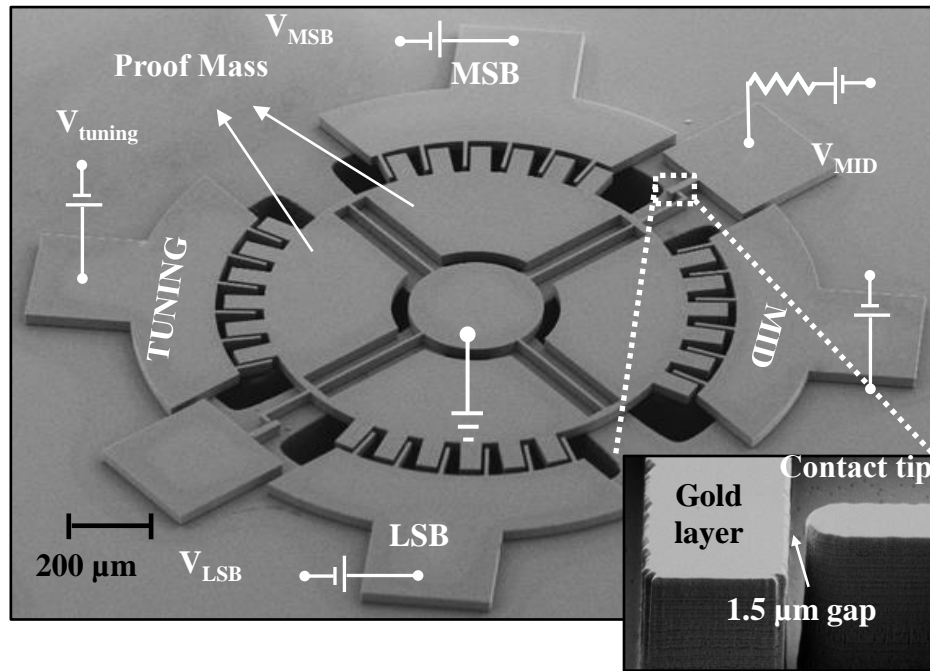


Figure 3.6. SEM views of the fabricated digital rotational accelerometer.

3.2.3 DEVICE PERFORMANCE

A DC motor capable of generating a maximum rotational acceleration of 392 rad/s^2 was utilized to apply different angular accelerations to the sensor. It was determined that a bias voltage of 57.4V is needed for the tuning actuator (while the other actuators are OFF) so that the proof mass comes in full contact with the output electrode when the device was subjected to maximum acceleration (full scale acceleration- A_{fs}). This sets the ‘111’ binary output of the accelerometer to 343 rad/s^2 ($0.875 A_{fs}$), i.e., full-scale acceleration of 392 rad/s^2 . Furthermore, it was determined that voltages of 26.00V, 18.40V and 13.04V are to be applied to the MSB, middle bit and the LSB actuators respectively to lower the threshold acceleration by 1/2, 1/4 and 1/8 of A_{fs} , respectively. Also, it is evident from the values of the bias voltages that Bit 2 provides a force $\sim 2X$ larger than the middle bit and $\sim 4X$ larger than the least significant bit. Device performance was validated by

applying different accelerations and monitoring the output while manually turning different actuators ON/OFF. Measurable device sensitivity in this case was limited by the minimum acceleration that the motor could provide reliably ($\sim 98\text{rad/s}^2$). For the device tested in this work, the control signals for altering the states of the three-bit electrodes were applied manually instead of using a controller for its operation. Results of the above-mentioned tests are tabulated in Table 3.3 showing that the device can distinguish between different accelerations in the desired range, which are very close to the theoretically expected ranges. Much better device sensitivity can be

Table 3.3. Measurement results of the rotational accelerometer versus the expected values. (Bit values in the Table indicate the ON/OFF (1/0) status of the actuator of the respective bit when contact occurs, which are opposite to that of the sensor digital binary output)

(MSB, MID, LSB) (State)	Acceleration Measured (A_{fs})	Acceleration Theoretical (A_{fs})
0 0 0	$a \geq 0.901$	$a \geq 0.875$
0 0 1	$0.901 \geq a \geq 0.765$	$0.875 \geq a \geq 0.75$
0 1 0	$0.765 \geq a \geq 0.629$	$0.75 \geq a \geq 0.625$
0 1 1	$0.629 \geq a \geq 0.502$	$0.625 \geq a \geq 0.5$
1 0 0	$0.502 \geq a \geq 0.361$	$0.5 \geq a \geq 0.375$
1 0 1	$0.361 \geq a \geq 0.205$	$0.375 \geq a \geq 0.25$
1 1 0	$0.205 \geq a \geq -$	$0.25 \geq a \geq 0.125$
1 1 1	-	$a \leq 0.125$

achieved by simply increasing the tuning actuator bias voltage (e.g. 70.5V for 8rad/s²). By changing the value of V_{bias} and V_{ON} , the accelerometer full-scale value can be tuned to a wide range of accelerations. Also, it should be noted that the MSB, MID and LSB values in Table 3.3 indicate the required ON/OFF state for the two actuators to maintain contact over the associated acceleration range. The binary acceleration output of the sensor that is to be provided by the digital processor is the exact opposite of the MSB, MID, LSB actuator state.

3.2.4 RESONANCE RESPONSE

To estimate the settling time required for each measurement step, the mechanical resonance frequency of the device was also measured under vacuum. Two out of the four electrodes were utilized to act as the AC input and the AC output electrode while the anchor/proof mass is biased

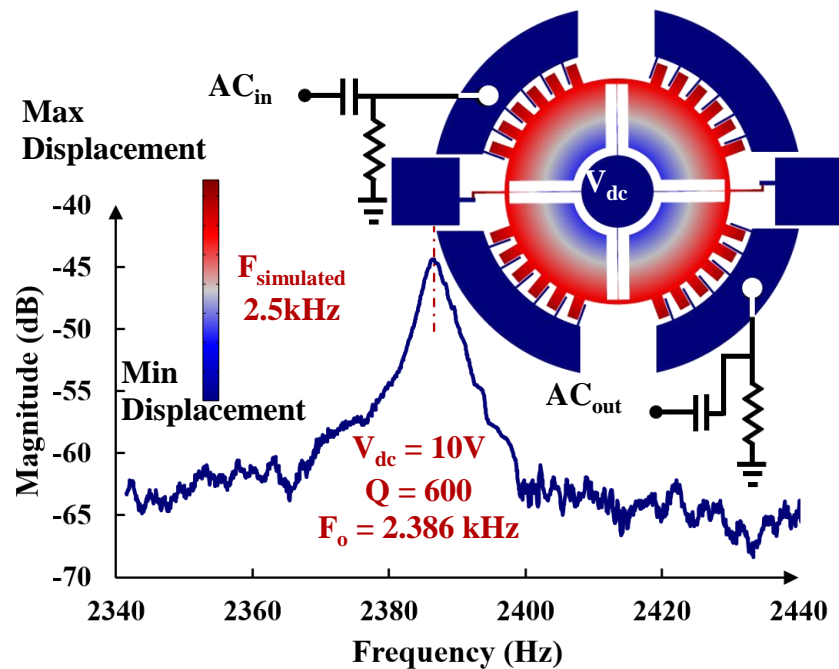


Figure 3.7. Measured sensor frequency response for polarization voltage of 10V along with finite element modal analysis of the structure showing the sensor's resonance mode shape.

with a DC voltage (Vdc). The resonance frequency for the device tested in this work was measured to be 2.386kHz (with a quality factor of ~600 when operated in ~20mTorr of pressure). This agrees with its simulated frequency value as shown in Figure 3.7. This value of frequency corresponds to a ~1.6ms settling time, i.e., ~4.8ms for a 3-bit measurement, consequently allowing a maximum measurement frequency of ~200Hz.

CHAPTER 4

BINARY TUNABLE INERTIAL SENSORS WITHOUT USE OF DIGITAL CONTROL⁴

4.1 SELF-COMPUTING COUPLED SWITCH INERTIAL SENSORS

(ELIMINATES DIGITAL CONTROLLER FOR OPERATION)

Figure 4.1 shows a highly simplified schematic of a 3-bit coupled switch accelerometer comprised of three acceleration switches. Each acceleration switch corresponds to one of the bits of the binary output and consists of a mass-spring combination and a stationary output electrode.

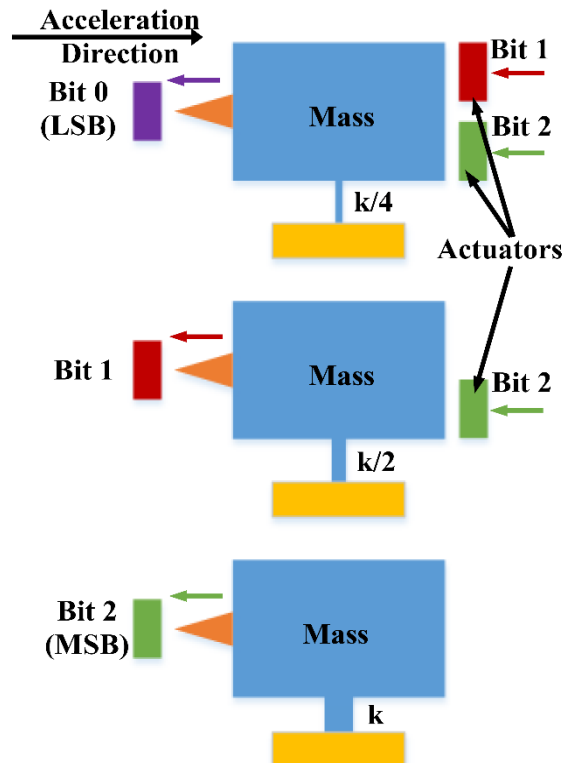


Figure 4.1. Simplified schematic of a 3-bit coupled switch accelerometer with digitized binary output.

⁴©2016 IEEE. Portions Adapted, with permission, from V. Kumar, X. Guo, and S. Pourkamali, "Ultra-Low Power Self-Computing Binary Output Digital MEMS Accelerometer", IEEE MEMS, Jan 2016.

The switches are to be designed so that the acceleration threshold of each switch is 2X larger or smaller than the next corresponding switch. The highest and the lowest acceleration thresholds belong to the switches associated with the Most Significant Bit (MSB) and the Least Significant Bit (LSB) respectively. Each corresponding bit after the MSB has an acceleration threshold 2X smaller than the previous bit, i.e., in Figure 4.1, Bit 1 has an acceleration threshold 2X smaller than the MSB (Bit 2) switch and the LSB (Bit 0) switch has an acceleration threshold 4X smaller than the MSB switch. The output of every switch is electrically connected to and therefore controls an electrostatic actuator acting on every switch associated with bits with lower significance. For instance, in Figure 4.1, the MSB bit controls an actuator acting on Bit 1 switch and another actuator acting on the LSB switch, whereas Bit 1 only controls an actuator acting on the LSB switch. The tether spring constant and mass of the MSB switch are to be chosen so that the acceleration threshold of the MSB switch is half of the full-scale acceleration ($0.5A_{fs}$). If the applied acceleration in the direction shown in Figure 4.1 has an intensity higher than half of the full-scale acceleration, the MSB switch will turn ON by making contact to its electrode on the left. As a result, the electrostatic actuator electrodes on the right-hand side of switches for Bit 1 and Bit 0, which are electrically connected to the output of the MSB switch, will turn ON, pulling their masses away from the contact electrodes, hence increasing the threshold for those switches. In other words, when the MSB turns ON, the actuators acting on Bit 1 and the LSB switches turn ON, effectively subtracting half the full-scale acceleration force from the acceleration force acting on the lower bits by generating a counteracting force. If the remaining acceleration is larger than the threshold of the Bit 1 (4X smaller than full scale acceleration), Bit 1 also turns ON leading to subtraction of another $0.25A_{fs}$ from the last switch. Depending on the intensity of the remaining

acceleration, the LSB will now turn ON or OFF. In this way, the electromechanical system automatically computes a digitized binary output without involvement of any electronics. Basically, the device itself is just a passive switch requiring energy only for charging and discharging the actuators which would be given to it by the acceleration it is subjected to. Such devices can eliminate the need for the readout circuitry all together leading to stand-alone fully electromechanical accelerometers with digital binary output and close to zero power consumption.

4.2 DEVICE FABRICATION

Device fabrication for the sensors remains the same as explained in Section 2.2.2. Figure 4.2 shows SEM views of the 2-bit coupled switch accelerometer fabricated using the described fabrication sequence. The device consists of two acceleration switches coupled to one another providing a 2-bit resolution binary digital output. In addition to the array of coupling parallel plate actuators connected to the output of the MSB switch that acts on the LSB switch, another array of similar parallel plate actuators has been embedded in each of the MSB and LSB switches for tuning purposes. Applying voltages to the tuning actuators can further bring the proof mass closer to the output electrode to reach the desirable acceleration threshold for each switch (V_1 and V_3 for the LSB and the MSB respectively).

4.3 MEASUREMENT SETUP AND RESULTS

For the specific device tested in this work, different magnitudes of tuning voltages were required due to the similar stiffness of tethers used for both the MSB and the LSB switches. Consequently, the tuning voltages were set so as to have a full-scale acceleration of 1g so that the device could be tested by holding the device at different angles, utilizing the Earth's gravity. Table 4.1 summarizes device dimensions and electrical parameters used in measurements. For the device

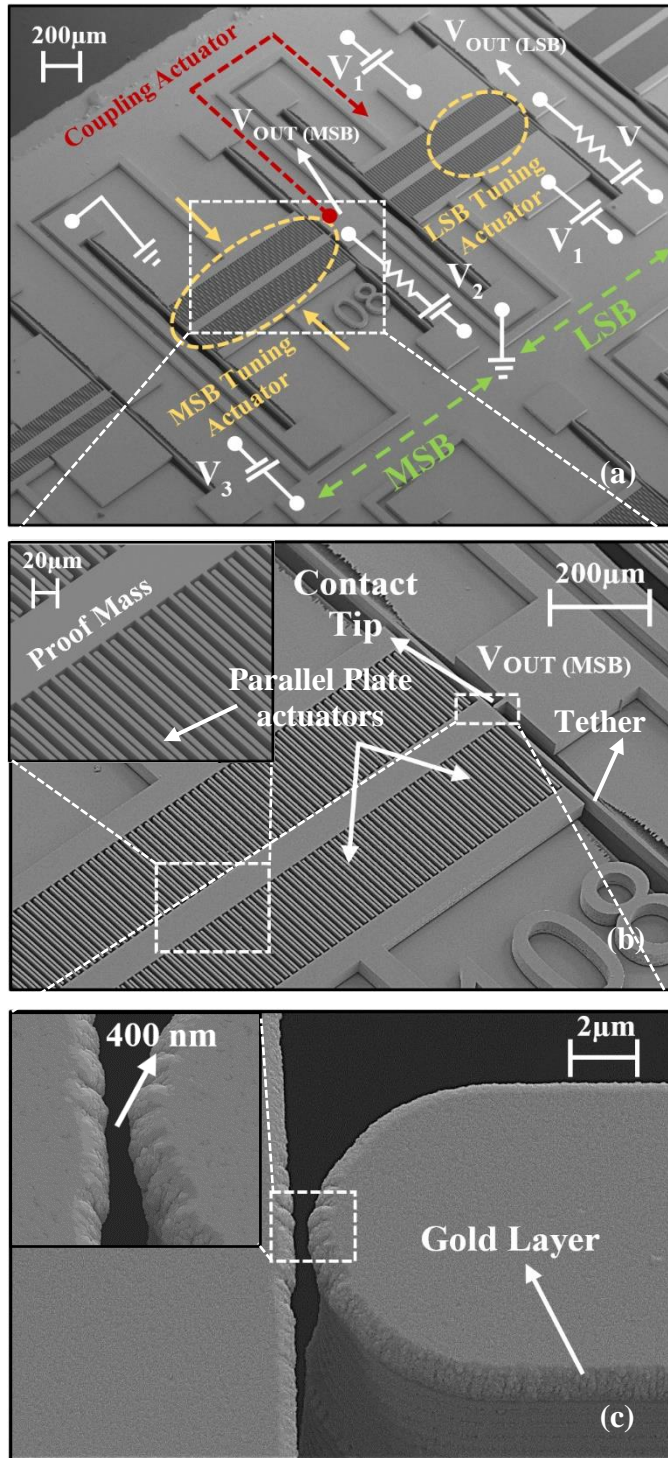


Figure 4.2. SEM views of the two-bit digital accelerometer along with the zoomed-in views of the contact gap.

Table 4.1. Device Dimensions and electrical parameters of the self-computing coupled switch linear accelerometer.

Parameter	Value
Stiffness of each tether	4.5 N/m
Proof mass on each bit	3.055e-9 Kg
Number of electrodes on the MSB	112
Number of electrodes controlled by the MSB on the LSB	56
Number of electrodes on the LSB	56
Length of each parallel plate actuator electrode	200 μ m
Width of each parallel plate actuator	5 μ m
Device Layer thickness	15 μ m
Capacitive gap between parallel plate actuators	3 μ m
Electrode Proof-mass gap on each bit	400nm
Output electrode voltage for LSB-V	5 V
LSB Tuning Voltage-V1	49 V
Coupling Actuator voltage/Output electrode voltage for MSB-V2	2.8 V
MSB Tuning Voltage-V3	10.8 V

in question, with the proof masses grounded, the actuation voltages V_1 , V_2 and V_3 are to be determined such that the MSB switch makes contact at 0.5g, while the LSB switch make contact at 0.25g when MSB switch is OFF, and at 0.75g when MSB switch is ON. In contrast to the

schematic demonstration in Figure 4.1, the force from the array of coupling parallel plate actuators connected to the output of the MSB switch does not oppose the acceleration force applied to the device but in fact helps it. In other words, the array of parallel plates of the coupling actuator helps the LSB in making contact when the MSB is OFF. To determine the required bias voltages, the device is first subjected to an acceleration of 0.75g. With V_2 and V_3 set to zero, V_1 should be just large enough for the LSB switch to make contact right at 0.75g. Leaving V_1 ON, the device is then subjected to 0.5g and V_3 is determined so that the MSB switch makes contact right at 0.5g. To determine V_2 , an acceleration of 0.25g was applied and V_2 was set to a value just large enough so that the LSB switch makes contact right at 0.25g. The contact made by the movable masses to the stationary electrodes is determined by reading the current at the output of the MSB and the LSB stationary electrode ($V_{OUT(MSB)}$ and $V_{OUT(LSB)}$).

Once the voltages have been determined, device performance was validated by rotating the device from 0g (0 degree with respect to the horizon) to 1g (90 degree with respect to the horizon) range. The MEMS device in Figure 4.2 was wire bonded to a printed circuit board and was subjected to different accelerations ranging between 0 and 1g by tilting the board to various angles while maintaining the tuning and coupling actuator voltages and monitoring the output of the MSB and LSB switches for each acceleration. Upon reaching 0.25g, contact was observed at the LSB switch turning the digital output from 00 to 01. Tilting the device further, upon reaching 0.5g, the contact was observed at the MSB switch, effectively negating the effect of the coupling actuator voltage V_2 , thus turning off the LSB (Digital output 10). Upon application of 0.77g, contact was observed at both the LSB and the MSB switch indicating a digital output of 11. The results are summarized in Table 4.2 showing that the device can distinguish between accelerations in the

ranges of 0-0.23g, 0.23g-0.5g, 0.5g-0.77g and >0.77g which are very close to the theoretically expected ranges. By changing the values of the tuning actuation voltages, the accelerometer can be tuned to measure any desired range of acceleration.

It was demonstrated that the concept of contact-based acceleration switches can be enhanced to perform higher resolution quantitative acceleration measurements. A tunable digitally operated MEMS accelerometer with a 2-bit resolution was successfully demonstrated. Also, the concept of utilizing electrostatically coupled acceleration switches as ultra-low power digital MEMS accelerometer was demonstrated. A coupled switch accelerometer consisting of two electrostatically tunable acceleration switches was fabricated using a 2-mask fabrication process and successfully tested as a binary output 2-bit digital accelerometer. The same device principle can be utilized to implement higher resolution (higher number of bits) binary output digital accelerometers. Elimination of the need for an analog front-end and signal conditioner can lead to significant power savings and leap forward towards ultra-low power MEMS inertial sensors.

Table 4.2. Measurement results of the Switched Coupled accelerometer along with expected values.

Acceleration (Theoretical)(g)	Acceleration (Measured) (g)	MSB	LSB
$g < 0.25$	$g < 0.23$	0	0
$0.25 \leq g < 0.5$	$0.23 \leq g < 0.5$	0	1
$0.5 \leq g < 0.75$	$0.5 \leq g < 0.77$	1	0
$g \geq 0.75$	$g \geq 0.77$	1	1

CHAPTER 5

SENSITIVITY ENHANCEMENT OF AMPLITUDE MODULATED OF LORENTZ FORCE MEMS MAGNETOMETERS⁵

5.1 INTERNAL THERMAL PIEZORESISTIVE AMPLIFICATION

The resonant structure of the device proposed in this work consists of a piezoresistive beam that is connected to two suspended mass plates on each side. In response to an alternating longitudinal force, in this case the alternating Lorentz force created by a DC current and an AC magnetic field, the structure can be actuated in its in-plane extensional resonance mode, wherein the piezoresistive beam undergoes consecutive compression and expansion as depicted in Figure 5.1(a). Consequently, due to the piezoresistive effect, the fluctuations in beam resistance (R_{ac}) created by the alternating compression and expansion can be detected through an output voltage. An alternating excitation force applied at the resonance frequency can induce vibration amplitudes Q_m times larger compared to a DC force creating a much larger output signal through the piezoresistor in response to the same external magnetic field, where Q_m is the mechanical quality factor of the resonant structure. MEMS magnetometers can take advantage of such resonance behavior to gain sensitivity amplification by a factor of Q_m .

The sensitivity of the magnetometers has been further improved significantly through the previously demonstrated “Internal Thermal Piezoresistive Amplification Effect” [76]. Internal amplification is a self-amplifying mechanism resulting from coupling of electro-thermal effects

⁵©2016 IOP. Portions Adapted, with permission, from V. Kumar, A. Ramezany, M. Mahdavi and S. Pourkamali, “Amplitude Modulated Lorentz Force MEMS Magnetometer with Pico-Tesla Sensitivity”, Journal of Micromechanics and Microengineering, Vol 26, Number 10, 105021, Sep 2016.

and piezoresistivity of the silicon beam. The alternating resistance R_{ac} created by the external magnetic field at resonance along with the DC bias current passing through the piezoresistor can induce an internal source of thermal actuation through Joule's heating. If such internal force is in

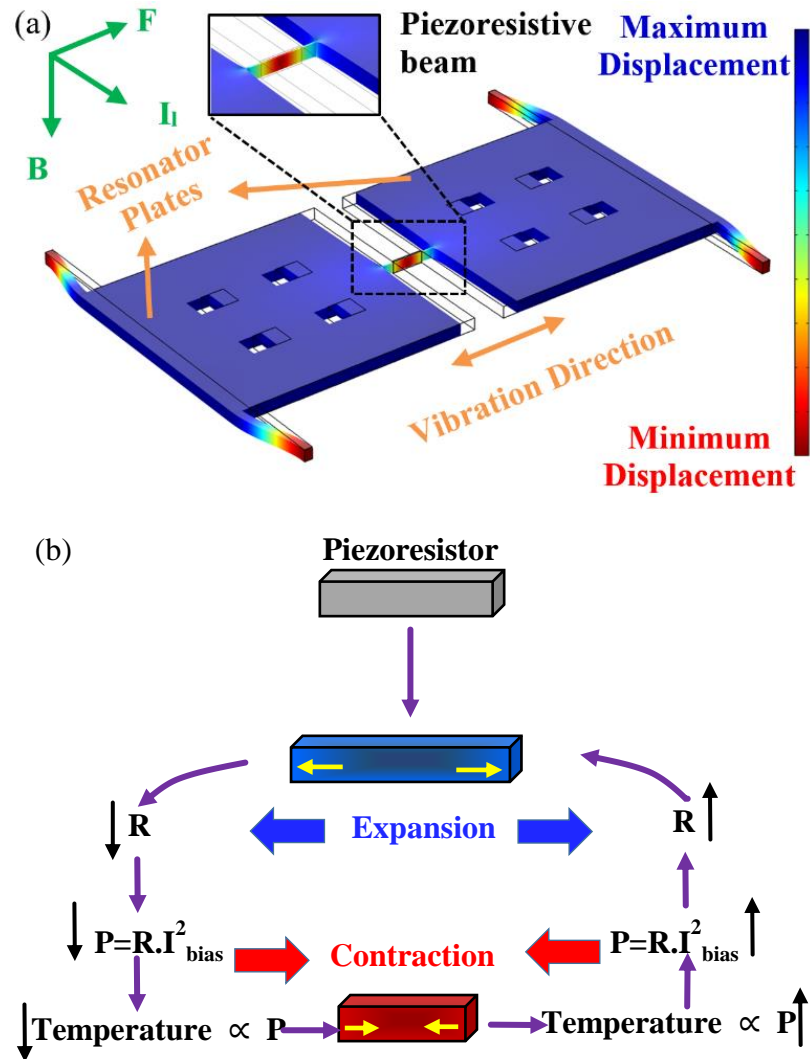


Figure 5.1.(a). Finite element modal analysis of the resonator showing its in-plane resonance mode due to magnetic field actuation.

(b). Expansion and contraction of the piezoresistive beam due to the alternating heating and cooling half cycles.

phase with the external Lorentz force, it can increase the vibration amplitude of the resonator by orders of magnitude through an internal positive feedback.

To elaborate, for an N-type doped silicon piezoresistor with a negative piezoresistive coefficient, the resistivity increases upon longitudinal contraction. If biased with a constant DC current, the contracted piezoresistive beam will heat up through Joule heating ($T_{ac} \propto P_{int} = I_{dc}^2 \times R_{ac}$), where T_{ac} is the temperature fluctuations created in the piezoresistive beam due to the internal fluctuating power P_{int} generated by the constant DC current I_{dc} and R_{ac}). Expansion, on the contrary, causes the piezoresistor to cool down due to the decrease in resistivity. At resonance as depicted in Figure 5.1(b), the drop-in temperature of the expanded piezoresistor helps contract the beam in the next half cycle, while the raise in temperature of the contracted beam assists the expansion in the next half cycle through thermal expansion.

Through this positive feedback loop the resonator absorbs power from the DC source and converts it into vibration amplitude, and therefore the modulated output voltage. Increasing the DC bias current passing through the beam (I_{dc}) augments the internal power (P_{int}) created by the Internal Thermal Piezoresistive Amplification. Consequently, a significantly larger vibration amplitude and output signal in response to the same input magnetic field can be achieved.

As the output signal at resonance frequency grows in response to increase in I_{dc} , the off-resonance output signal remains constant. Therefore, the effective quality factor Q defined as $\omega_0/(\omega - 3db)$ increases through the internal amplification. In other words, the electrical energy pumped into the system by the internal amplification can compensate for loss in the system and raise the effective quality factor. While the effective quality factor significantly improves by the internal amplification, the mechanical quality factor Q_m defined as the ratio of mechanical energy stored

in the piezoresistor to energy loss in the system per cycle, which is only a function of device geometry and physical properties, remains constant.

5.2 ELECTRO-THERMO-MECHANICAL MODEL

Figure 5.2 shows the schematic diagram of the resonant magnetometer. A magnetic field applied at the resonance frequency creates a vibration with amplitude X_L through Lorentz force.

$$H_L(s) = \frac{X_L}{B} = \frac{I_l L_l}{Ms^2 + bs + K} \quad (5.1)$$

where I_l and L_l are the DC current applied to the device for Lorentz force generation and length of the current carrying path as depicted in Figure 5.1, M the resonator effective mass, K the

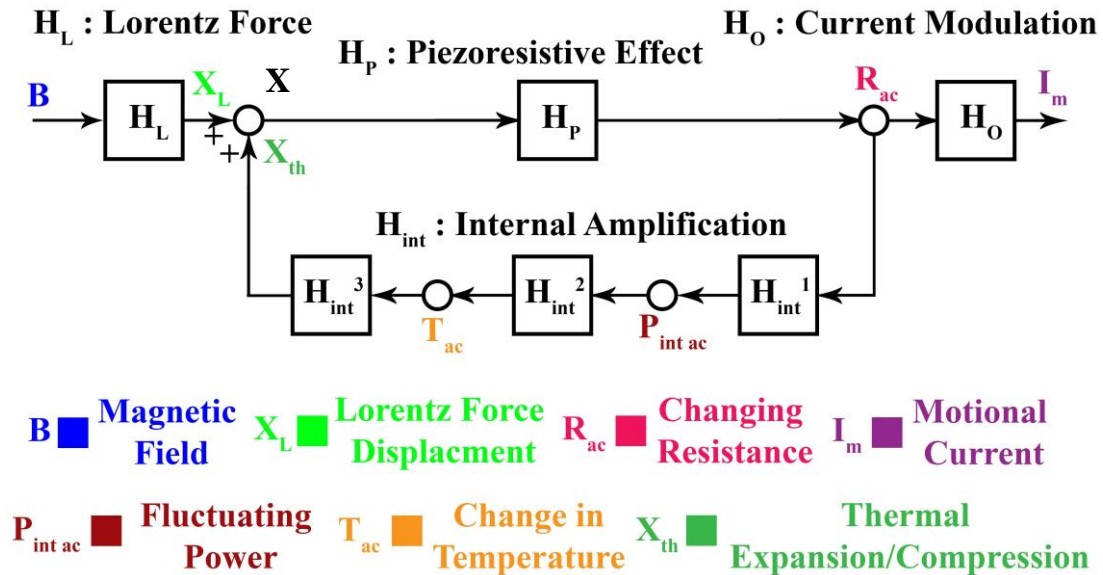


Figure 5.2. Schematic diagram for the resonant magnetometer highlighting the interactions between different domains involved (Magnetic, Thermal, Mechanical and Electrical) and the resulting feedback loop. Amplification occurs when the feedback loop has a positive overall gain less than unity.

piezoresistor stiffness, and b is the resonator damping factor. Due to the piezoresistive effect, the stress inflicted on the beam by the vibration will create a fluctuating resistance R_{ac} .

$$H_P = \frac{R_{ac}}{X} = \frac{2R_a\pi_l E}{L} \quad (5.2)$$

where R_a is the electrical resistance of the piezoresistor at rest, π_l is its longitudinal piezoresistive coefficient, E is the Young's modulus of the structural material, and L is the length of the piezoresistor.

The combination of the R_{ac} and the bias current passing through the piezoresistor I_{dc} forms a fluctuating internal thermal power source (Equation 5.3).

$$H_{int1} = \frac{P_{int\ ac}}{R_{ac}} = I_{dc}^2 \quad (5.3)$$

Through Joule's heating this source will cause fluctuations in the piezoresistor temperature (T_{ac}) according to equation (4), in which R_{th} and C_{th} are the thermal resistance and thermal capacitance of the piezoresistive beam respectively. At high enough frequencies where typically, the mechanical resonance period is much shorter than the thermal time constant i.e., $R_{th} C_{th} \omega \gg 1$, Equation 5.4 can be further simplified and will be independent of thermal resistance.

$$H_{int2}(s) = \frac{T_{ac}}{P_{int\ ac}} = \frac{R_{th}}{(1 + R_{th}C_{th}s)} \cong \frac{1}{C_{th}s} \quad (5.4)$$

Subsequently, thermal expansion turns the fluctuating temperature T_{ac} into displacement X_{th} through Equation 5.5 that will be added to the displacement created by the Lorentz force (α

thermal expansion coefficient, and A cross sectional area of the beam). Depending on the sign of the piezoresistive coefficient X_{th} and X_L can be in or out of phase. For n-type doped silicon as depicted in Figure 5.2, the internally generated displacement X_{th} adds to the externally generated X_L hence amplifying the vibration amplitude [76].

$$H_{int3}(s) = \frac{X_{th}}{T_{ac}} = \frac{\alpha AE}{Ms^2 + bs + K} \quad (5.5)$$

Eventually, the overall fluctuating resistance R_{ac} is translated into a change in output voltage v_{out} , which can be calculated as:

$$H_O = \frac{v_{out}}{R_{ac}} = \frac{R_l}{R_a} I_{dc} \quad (5.6)$$

where R_l is the load resistance. The overall transfer function of the resonant magnetometer defined as the ratio of output AC voltage to the input magnetic field can be calculated as:

$$H_T(s) = \frac{v_{out}}{B} = H_L \frac{H_P}{1 - H_P H_{int}} H_O \quad (5.7)$$

where $H_{int}(s) = H_{int1} H_{int2} H_{int3}$

At the resonance frequency, the overall transfer function will be:

$$H_T(j\omega_0) = -I_l L_l \cdot \frac{R_A \pi_l E C_{th} \omega_0 j}{\frac{EA^2 C_H \sqrt{ELA}}{\sqrt{2} Q_m} + 2\rho L \pi_l E^2 \alpha I_{dc}^2} \cdot \frac{I_{dc}}{R_a} R_l \quad (5.8)$$

in which Q_m is the mechanical quality factor defined as the energy stored in the structure over the energy loss per cycle and calculated as $Q_m = \frac{M\omega_0}{b}$. Equation 5.8 suggests that the motional current is 90° behind the actuating magnetic field. As the bias current increases, and the loop gain $H_P H_{int}$

at resonance approaches unity, the output voltage increases. In this fashion, the increase in the bias current I_{dc} will raise the output signal at resonance frequency above the feedthrough level progressively, improving the sensitivity and the effective quality factor until the device is pushed towards an ultimately unstable state. The effective quality factor Q of the device can be estimated by [77]:

$$Q = \frac{Q_m}{\left(1 + \frac{R_l \parallel R_a}{r_m}\right) \sqrt{2 + \left(1 + \frac{R_l \parallel R_a}{r_m}\right)^2}} \quad (5.9)$$

Where $r_m = 1/g_m$ and $g_m \propto I_{dc}^2$.

5.3 DEVICE FABRICATION AND DESCRIPTION

Dual plate monocrystalline silicon resonant structures were fabricated on an SOI substrate using a single mask micro-machining process. The 15 μm thick device layer (0.01 $\Omega\text{-cm}$ resistivity) was first patterned using standard photolithography. The silicon device layer was then etched using deep reactive ion etching (DRIE). The 2 μm buried oxide layer was removed by wet etching in Hydrofluoric acid. Holes on the resonator plates were provided to facilitate and accelerate removal of the buried oxide underneath the large resonator plates.

Figure 5.3 shows the SEM view of the fabricated structure. The 800 $\mu\text{m} \times 800\mu\text{m}$ resonator plates are connected by a 30 μm long, 1.5 μm wide piezoresistive beam. The set of comb-drives and parallel plate electrodes located around the resonator plates were included in the design for characterization purposes via capacitive actuation and sensing, if needed, and were not utilized when operated as a Lorentz Force magnetometer. The drive pads (D1 and D2) located on the two sides of the resonator plates are used for application of the Lorentz Force actuation DC current

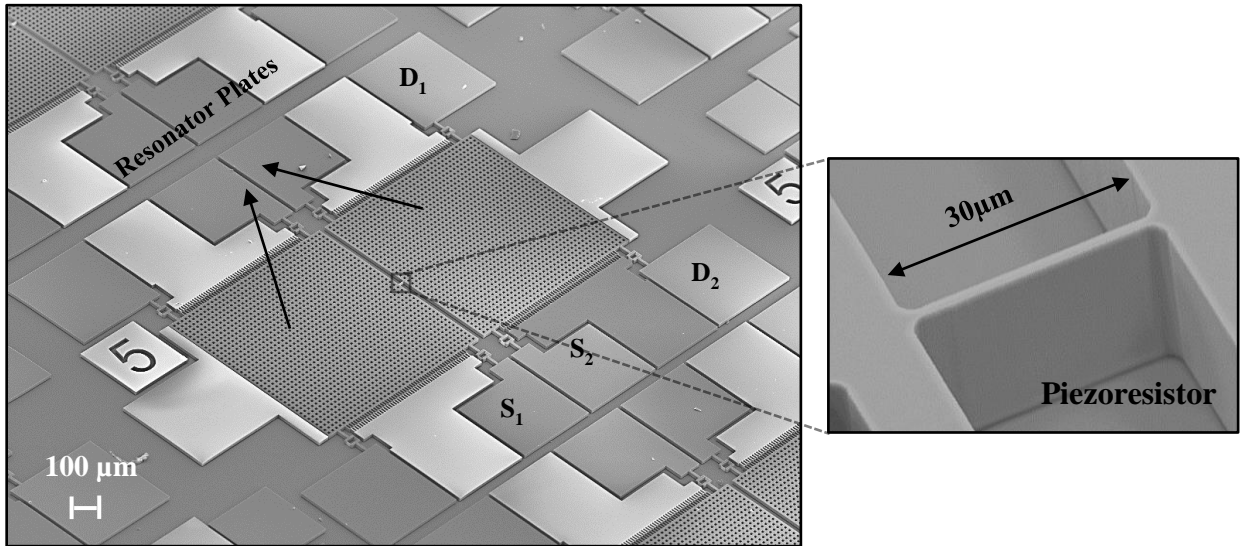


Figure 5.3. SEM view of the 400kHz dual plate in-plane resonant magnetometer.
 Right- Zoomed-in view of the piezoresistor ($30\mu\text{m}\times 1.5\mu\text{m}\times 15\mu\text{m}$).

(I_l). In addition to this, the piezoresistive beam is biased with a DC current (I_{dc}) (across pads S1 and S2).

5.4 MEASUREMENT RESULTS

5.4.1 TEST SETUP

Figure 5.4 shows the measurement setup and the electrical connections for testing the device as a Lorentz force magnetometer along with the mode shape of the in-plane resonance mode. To test the resonator as a Lorentz Force magnetometer, a relatively long current carrying wire was placed along the device, perpendicular to the piezoresistive beam. This wire acts as the source of the magnetic field for in-plane actuation of the resonator. The magnitude of magnetic field generated by the wire is a function of the current flowing through the wire and the distance between the wire and the device, given by $B = \frac{\mu_0 I_o}{2\pi r}$ where μ_0 is the magnetic permeability of free space ($4\pi \times 10^{-7} \text{N A}^{-2}$), I_o is the current flowing through the wire and r is the distance between

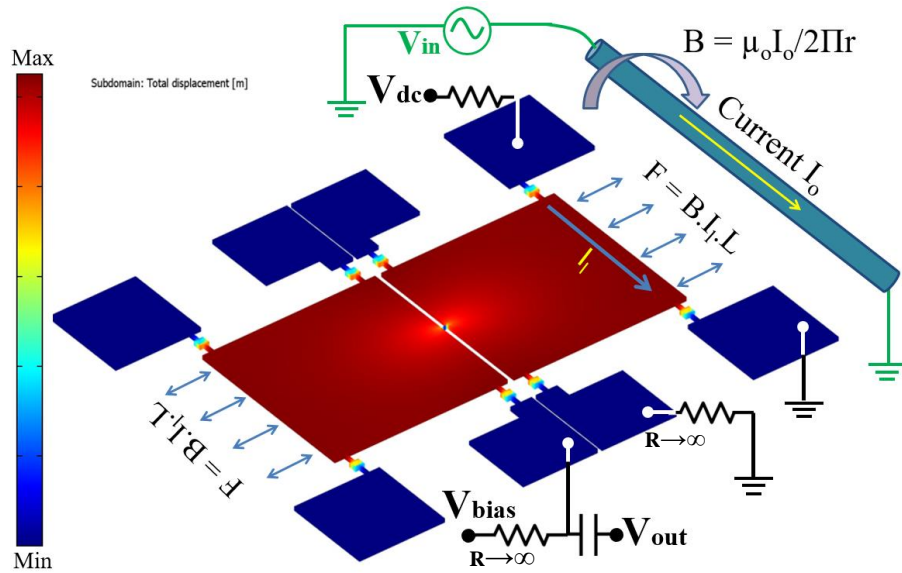


Figure 5.4. Finite element modal analysis of the resonator showing the in-plane resonance mode and the measurement setup and its electrical connections.

the wire and the device. A separate DC current was applied to the device for Lorentz force generation (V_{dc}), and an AC magnetic field at the device resonant frequency was used to actuate the device. To generate the AC field, the RF output of the network analyzer was connected to the wire as shown in Figure 5.4. One advantage of using an AC field for characterization of the device is that the device can operate impervious to the interference from Earth's magnetic field. The resonator frequency responses were obtained for different magnitudes of magnetic fields by changing the current and the distance of the wire from the device.

5.4.2 RESULTS

Figure 5.5 illustrates the resonant frequency response of the magnetometer for a field intensity of 3.5 nT for different piezoresistor bias currents (in the range 5.164mA-7.245mA). It is evident from the graph that the output signal amplitude increases by increasing the DC bias current given to the piezoresistive beam. An increase in the DC bias current through the internal

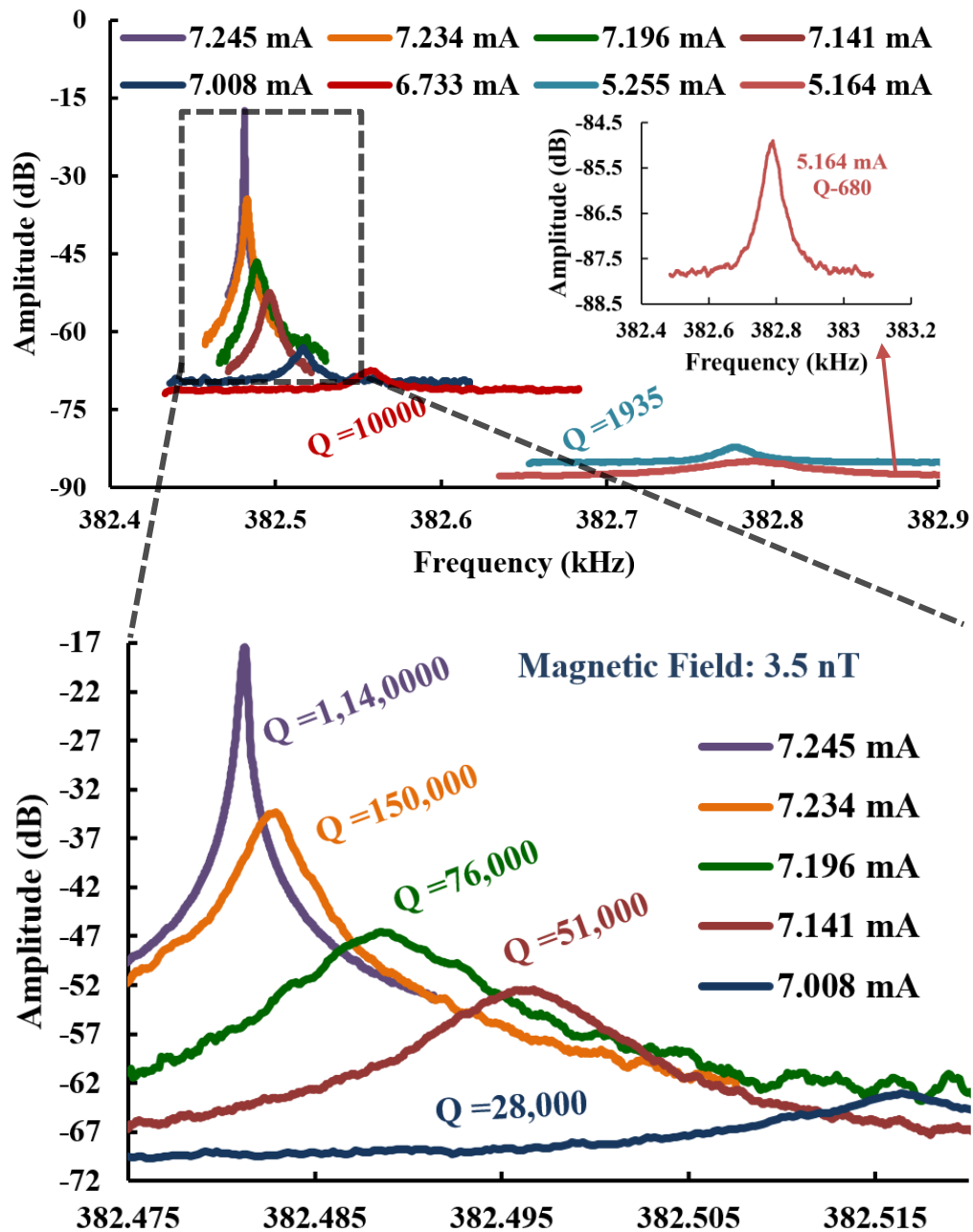


Figure 5.5. Resonant responses of the device with different bias currents under constant magnetic field intensity of 3.5 nT for bias currents in the range 5.164mA-7.245mA. Inset shows the resonant response of the device at 5.164mA having a quality factor of ~680.

Bottom: Resonant responses of the device with different bias currents under constant magnetic field intensity of 3.5 nT for bias currents in the range 7.008mA-7.245mA.

amplification increases the vibration amplitude, and therefore the output modulated signal at resonance.

Figure 5.6 shows the measured effective quality factor of the device for bias currents ranging from 5.164mA-7.245mA. It can be seen that the effective quality factor of the resonator increases from its intrinsic value of 680 at 5.164mA to 1.14×10^6 at 7.245mA under atmospheric pressure. The measured data has a close fit to the quality factors as predicted by the mathematical model in the previous section as shown in Equation 9. The inset in Figure 5.6 shows the frequency response of the device as seen on the network analyzer for the magnetometer operating at a DC bias current of 7.245mA with a magnetic field of 3.5nT. An output voltage amplitude of 7.55mV

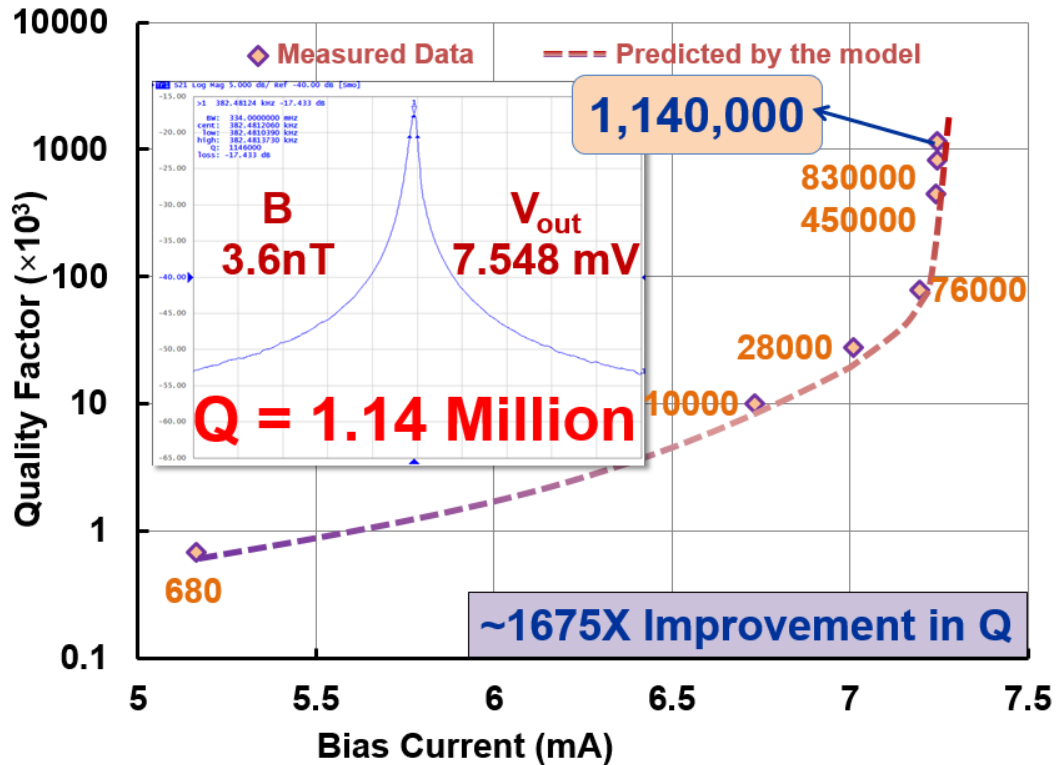


Figure 5.6. Graph showing measured effective Quality Factor versus the bias current demonstrating the Q and vibration amplification effect.

Inset- Network Analyzer response for piezoresistor bias current of 7.245 mA.

is measured in this configuration (peak level of -17.4 dB) leading to a maximum sensitivity of 2.107mV/nT.

Figure 5.7 illustrates the measured output voltage amplitudes (left y-axis) at resonance versus the magnitude of magnetic field for different piezoresistor bias currents. There is a ~2400X improvement in sensitivity (from 0.9 μ V/nT to 2.107 mV/nT) when the bias current is increased from 5.164 mA to 7.245mA. The increase in output amplitudes (and thus sensitivity) at higher currents is partly due to higher piezoresistive sensitivity (higher piezoresistor bias current) and partly due to internal vibration amplification (artificial Q-amplification). To demonstrate the effect of internal amplification alone, sensitivity figure of merit (FOMS) has been defined as sensitivity divided by the piezoresistor bias current. Figure 5.7 (secondary y-axis) illustrates the different

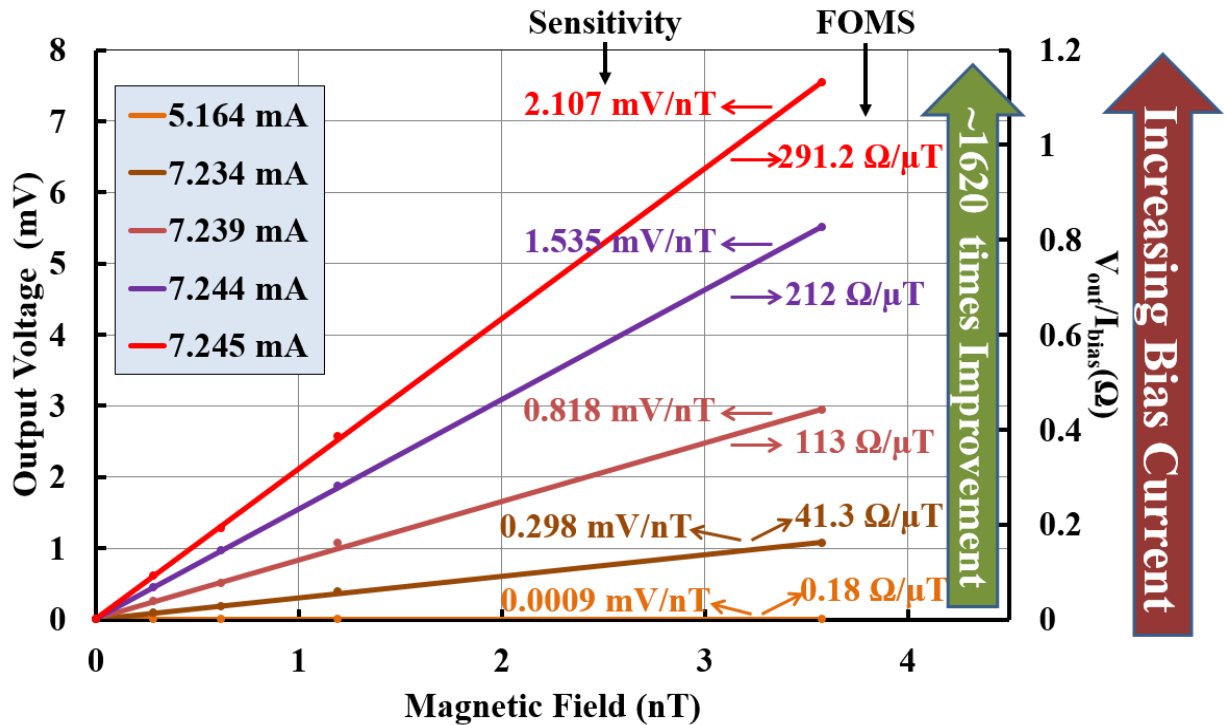


Figure 5.7. Graph showing the output voltage amplitude and the FOMS values versus the magnetic field intensity for different bias currents.

output voltage over their respective bias currents, the slope of which represents the FOMS, showing a ~1620X improvement as a result of internal amplification alone.

5.4.3 NOISE FLOOR, STABILITY AND SENSOR FIELD RESOLUTION

The internal thermal piezoresistive amplification effect can also amplify the thermo-mechanical noise. However, analysis shows that since amplification and filtering occur at the same time within the same component, i.e., the amplification factor itself has a narrow band response, it thus amplifies only the noise components within its narrow bandwidth [78]. Therefore, the overall signal to noise ratio of the sensor is expected to improve by increase in the amplification factor and reduction in the bandwidth. Hydrofluoric acid. Holes on the resonator plates were provided to facilitate and accelerate removal of the buried oxide underneath the large resonator plates.

The noise magnitude in this case is a function of both temperature and mechanical damping. To study and compare the amplification rate in noise and the output signal due to the effect of internal amplification, the noise floor was measured for various bias currents, and the increase in its amplitude was compared with the output signal amplitudes. Figure 5.8 and 5.9 show the output spectrum of the sensor in response to a 3.5nT magnetic field input (blue lines) given at DC bias currents of 5.164mA and 7.245mA, respectively, along with their measured output noise spectrum when the input AC magnetic field input is turned off (red dotted lines). At a bias current of 7.245mA, the sensor noise is measured to be $0.3\mu\text{V}/\sqrt{\text{Hz}}$ in contrast to the output of $377.39\mu\text{V}/\sqrt{\text{Hz}}$ for an input field of 3.5nT which corresponds to a sensor field resolution of $2.8\text{ pT}/\sqrt{\text{Hz}}$. When the bias current is increased from 5.1mA to 7.2mA, it is shown that the output signal due to the presence of a magnetic field is increased by a factor of $\times 1000$, while the noise signal added to the output by the device is increased by 50% (most likely due to increased thermal noise at higher

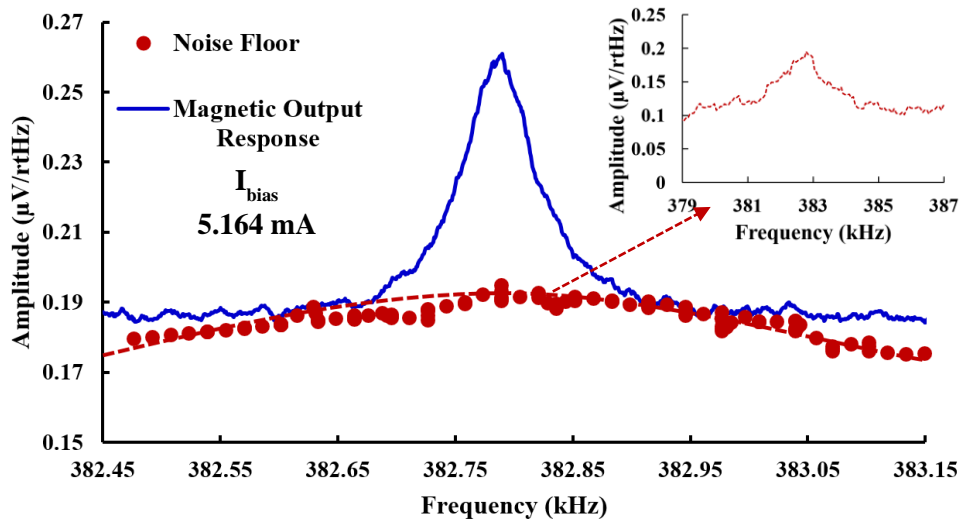


Figure 5.8. Output spectrum of the sensor for an input magnetic field of 3.5nT along with its measured noise floor for a bias current of 5.164mA.

Inset: Output noise spectrum for the sensor measured at the bias current of 5.164mA.

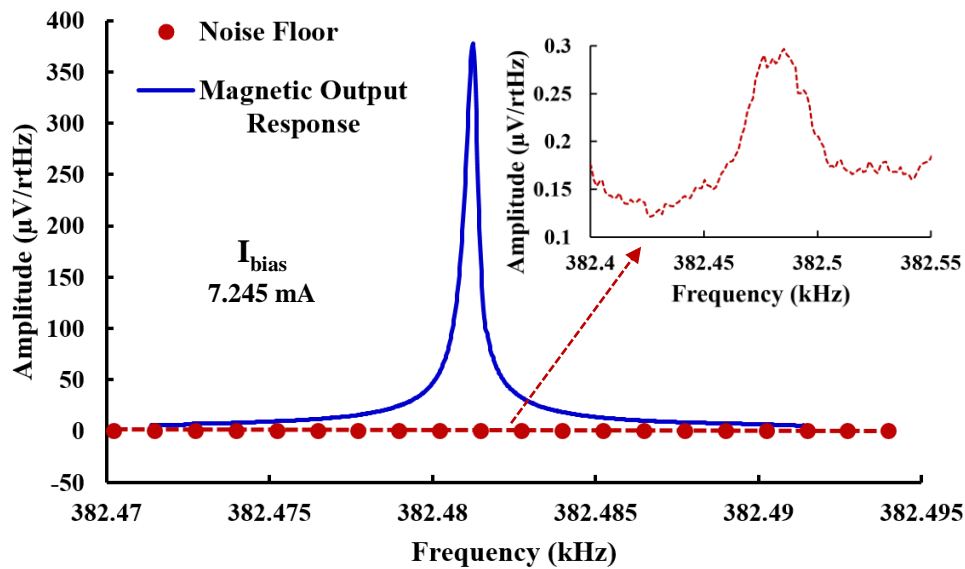


Figure 5.9. Output spectrum of the sensor for an input magnetic field of 3.5nT along with its measured noise floor for a bias current of 7.245mA. Inset: Output noise spectrum for the sensor measured at the bias current of 7.245mA.

bias currents). The measurement results are summarized in Table 5.1 which highlights the sensitivity, FOMS, effective Q, and Sensor field resolution for different bias currents.

Table 5.1. Sensitivity, FOMS, Quality Factor and Sensor Resolution for the Magnetometer at Different Bias Currents

Bias Current (mA)	Sensitivity ($\mu\text{v/nT}$)	FOMS ($\Omega/\mu\text{T}$)	Quality Factor	Resolution ($\text{pT}/\sqrt{\text{Hz}}$)
5.164	0.89	0.18	680	2340.3
6.733	17.87	2.7	1×10^4	264.64
7.141	90.73	12.7	2.8×10^4	61.71
7.196	145.44	20.2	7.9×10^4	39.34
7.236	542.05	74.9	28.5×10^4	10.72
7.239	818.23	113	45×10^4	7.11
7.243	1188	164	6.3×10^5	4.9
7.244	1535.7	212	8.3×10^5	3.79
7.245	2107.8	291.2	1.1×10^6	2.76

Although the device was never operated as an oscillator, to present a measure of random drift error in the resonance frequency of the sensor, the Allan deviation was measured at a bias current for which the device is pushed to self-sustained oscillation. Figure 5.10 shows the measured Allan deviation for the sensor operating at a bias current of 7.25mA slightly above 7.245mA for which the maximum sensitivity was reported with maximum quality factor of 1.1×10^6 . A minimum Allan deviation of less than 0.001 ppm change in frequency was achieved in less than 2 minutes.

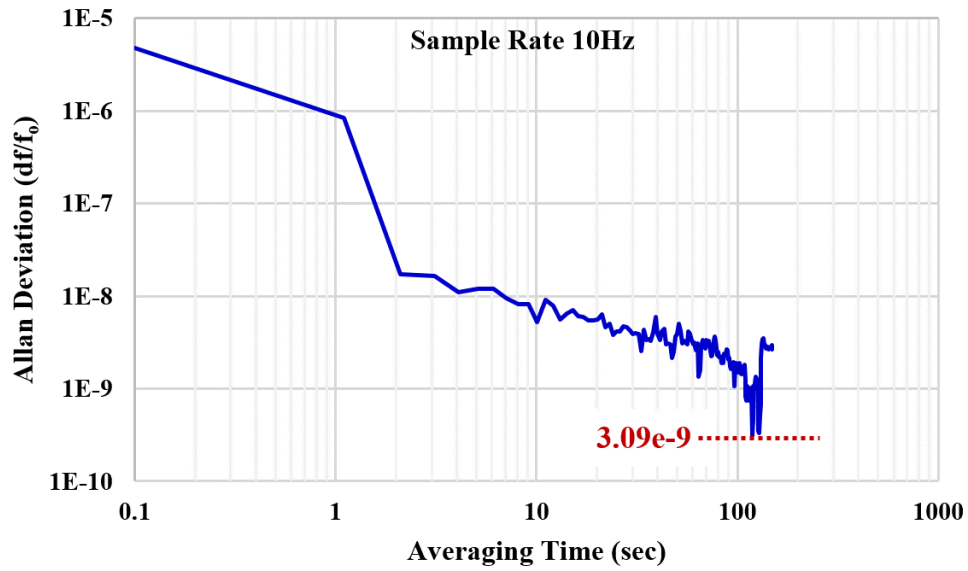


Figure 5.10. Measured Allan Deviation for the sensor output at a DC bias of 7.25mA.

At higher bias currents where the quality factor is extremely high, and the bandwidth is very small, the stability of the resonance peak is of utmost importance. Therefore, the stability of the resonance response for various bias currents was also measured. The resonance peak frequencies were monitored for 30 minutes with a large IFBW of 1kHz. Figure 5.11 illustrates the measured standard deviation of the resonance peak frequency compared with the -3dB bandwidth for various bias currents. As is evident from Figure 5.11 that the drift error in the peak frequency of the sensor is almost always less than the measured-3dB bandwidth at its respective bias current. As for the considerations of temperature on the resonance frequency itself, the large negative TCF (Thermal coefficient of Frequency) of single crystal silicon can be highly suppressed by doping the devices with high concentrations of an n-type dopant as demonstrated in [79].

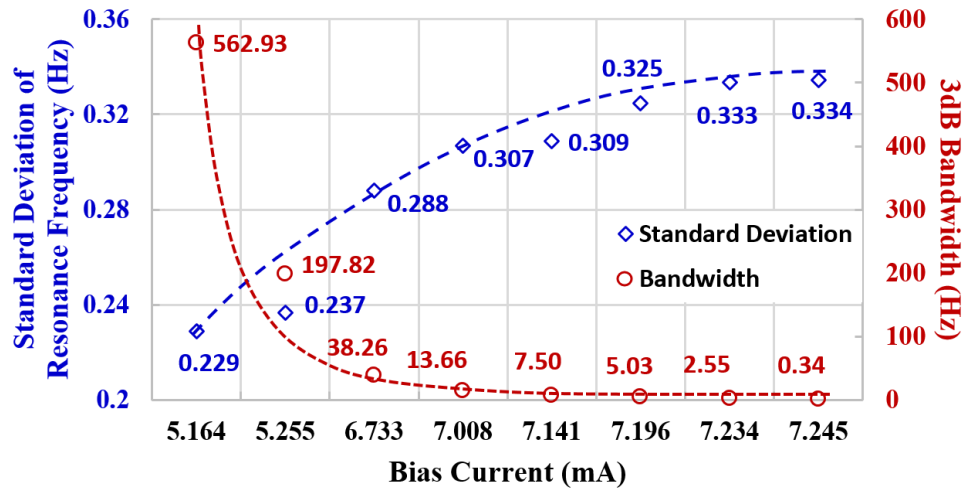


Figure 5.11. Measured standard deviations of the resonance peak frequency compared with the 3dB bandwidth of the sensor for various bias currents.

CHAPTER 6

SENSITIVITY ENHANCEMENT OF FREQUENCY MODULATED OF LORENTZ FORCE MEMS MAGNETOMETERS⁶

6.1 PRINCIPLE OF OPERATION-LEVERAGE MECHANISM

As discussed in the previous chapter, the existing problem in most Lorentz force magnetometers is that large forces are required to cause the slightest amount of distortion in the resonator structure and change its frequency significantly (due to the relatively large stiffness of the structure). Lorentz forces are generally very small and therefore amplification of the force is required to enhance the device sensitivity. For example, a magnetic field of $10\mu\text{T}$ acting on a $1500\mu\text{m}$ long beam, carrying a current of 10mA would create a Lorentz force of just 0.15nN leading to a displacement of less than 0.01 pm in the resonator (having a stiffness of ~ 9000), which is undetectable. To alleviate this problem, the resonator stiffness should be lowered as much as possible, and a Lorentz force generator with a high gain leverage mechanism is to be utilized. Figure 6.1(a) illustrates the amplification mechanism for boosting the lateral Lorentz force (F_l) into an amplified axial force (F_x).

6.2 DEVICE DESCRIPTION

Figure 6.1(b) illustrates the device structure and the finite element static force analysis of the frequency modulated resonator. The $60\mu\text{m}$ long, $2\mu\text{m}$ wide beam in the middle of the resonator connecting the $300\mu\text{m} \times 300\mu\text{m}$ resonator plates acts as the piezoresistor as well as the thermal

⁶©2017 IEEE. Portions Adapted, with permission, from V. Kumar, S. Sebdani and S. Pourkamali, “Sensitivity Enhancement of a Lorentz Force MEMS Magnetometer with Frequency Modulated Output”, Journal of Micromechanical Systems, Vol 26, Issue 4, Aug 2017.

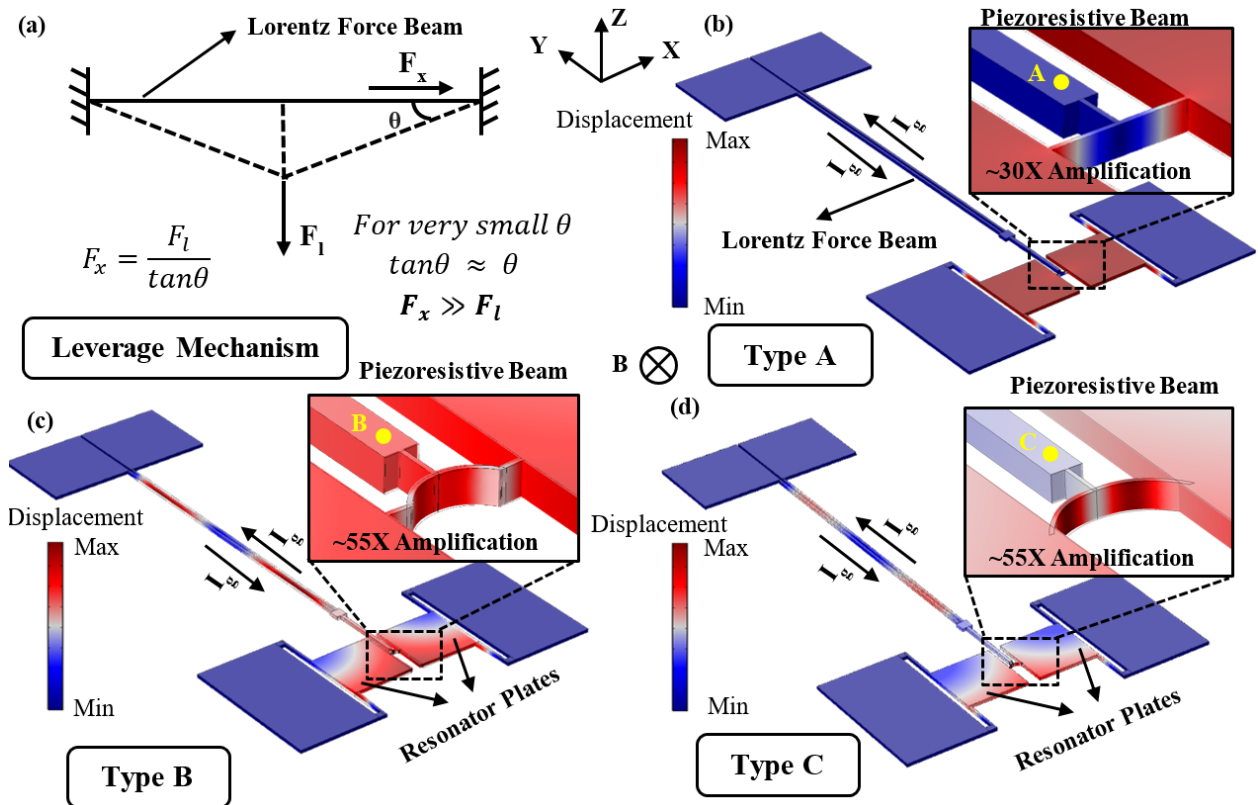


Figure 6.1(a). Simple schematic showing the basic concept of the amplification mechanism. (b) (c) (d) Finite element static force analysis of the frequency modulated resonator showing the force amplification due to the leverage mechanism for three different beam structures (Type A, Type B and Type C).

actuator [80]. To reduce the overall stiffness of the device, two curved designs of the piezoresistor (Type B and Type C) as opposed to a straight beam (Type A) have been utilized as shown in Figure 6.1(c) and 6.1(d). When the resonator resonates in its in-plane mode, the piezoresistor acts as a strain gauge that undergoes periodic tensile and compressive stress. Type A structure with the perfectly straight piezoresistive beam resonates in just one single axis ($\pm X$ axis) at its in-plane resonance mode, whereas Type B and Type C structures exhibit some movement in the $+Y$ axis as well due to the nature of the shape of the beams. The Lorentz force generator is comprised of two long silicon beams ($1500 \mu\text{m}$ each) located perpendicular to the piezoresistor. Upon introducing a

magnetic field perpendicular to the direction of current flowing through the beams, the beams bend laterally in opposite directions due to the presence of a Lorentz force. This Lorentz force is turned to an amplified axial force due to the leverage mechanism as described before, acting perpendicular to the piezoresistive beam, thus modulating the device stiffness and consequently, its resonance frequency. In addition to this, the Lorentz force acting on the long silicon beams deflects them in opposite directions such that the amplified axial forces add up, further enhancing the sensitivity.

Based on the finite element static force analysis for the specific design used in this work, a 1nN lateral force (in the positive and negative X direction) applied to the Lorentz force beam for the structure shown in Figure 6.1(b) has been translated to an amplified axial force (positive Y direction) of ~30nN at Point A in the inset of Figure 6.1(b). The axial force is thus ~30X larger than the lateral force caused by the magnetic field applied to the device, increasing the sensitivity significantly. In contrast, a 1nN lateral force applied to the Lorentz force beam for the structures shown in 6.1(c) and 6.1(d), the axial force has been amplified by ~55X at Point B and Point C as shown in the inset of Figure 6.1(c) and 6.1(d). This is mainly because of the much lower lateral stiffness of the piezoresistive beams of structures in Type B and Type C.

6.3 LORENTZ FORCE BEAM DESIGN

Figure 6.2 shows the schematic view of the bending of the Lorentz force beam and the piezoresistive beam due to an applied Lorentz Force F_l . To develop the relationship between the effect of the leveraged force on the piezoresistive beam based on the geometrical dimensions and the axial and lateral stiffness's of the structure, the deformation angle θ is assumed to be very small. Therefore, the deformed Lorentz force beam L_g can be written as:

$$L_g = L' + X_b \quad (6.1)$$

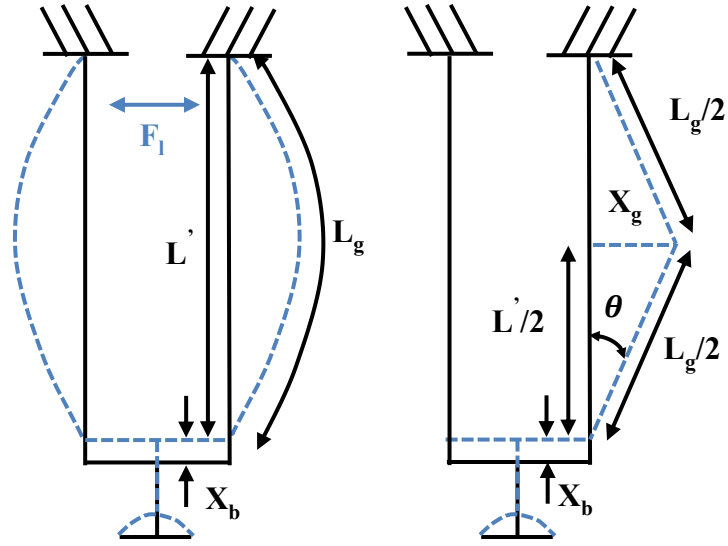


Figure 6.2. Schematic showing the bending of the Lorentz force beams and the piezoresistive beam due to the applied Lorentz Force F_l .

where X_b is the lateral displacement of the piezoresistive beam due to the applied force F_l . Due to the very small deformation angle θ ,

$$\left(\frac{L_g}{2}\right)^2 = \left(\frac{L'}{2}\right)^2 + X_g^2 \quad (6.2)$$

where X_g is the displacement in the Lorentz force beam caused due to the Lorentz Force F_l given by

$$X_g = \frac{F_l}{K_{lg}} \quad (6.3)$$

where K_{lg} is the lateral stiffness of the Lorentz Force beam. Substituting the value of X_g in Equation 6.2 and rearranging the terms, L' can be written as:

$$L' = 2 \sqrt{\left(\frac{L_g}{2}\right)^2 - \left(\frac{F_l}{K_{lg}}\right)^2} \quad (6.4)$$

The Lorentz force acting on two Lorentz force beams of length L_g can be given by:

$$F_l = 2 * BI_g L_g \quad (6.5)$$

Where B is the magnetic field intensity and I_g is the current flowing on the Lorentz force beams.

Substituting the value of F_l and L' in Equation 6.1:

$$L_g = 2 \sqrt{\left(\frac{L_g}{2}\right)^2 - \left(\frac{2BI_g L_g}{K_{lg}}\right)^2} + X_b \quad (6.6)$$

Thus, the lateral displacement X_b of the piezoresistive beam can be written as:

$$X_b = L_g - L_g \sqrt{1 - \left(\frac{4BI_g}{K_{lg}}\right)^2} \quad (6.7)$$

In addition to the displacement caused in the piezoresistive beam due to the Lorentz force F_l in the Lorentz force beams, another additional Lorentz force is created due to the current flowing in the piezoresistive beam itself which is given by:

$$F_{lp} = BI_{res} L_b \quad (6.8)$$

Therefore, the total displacement caused due to the presence of the magnetic field is given by:

$$X_{bTotal} = \left(L_g - L_g \sqrt{1 - \left(\frac{4BI_g}{K_{lg}}\right)^2} \right) + \frac{BI_{res} L_b}{K_{lb}} \quad (6.9)$$

The Lorentz force beam can be assumed to be a clamped-clamped beam whose lateral stiffness can be written as:

$$K_{lg} = \frac{16Ew^3t}{L_g^3} \quad (6.10)$$

Where E is the Young's modulus of the silicon, w and t are the width and thickness of the Lorentz force beam respectively. The displacement X_{bTotal} causes a change in the geometrical dimensions

as well as Young's modulus of the piezoresistive beam which consequently gets reflected in the overall stiffness of the piezoresistive beam given by:

$$K_{lb} = \frac{16Ew_b^3t}{L_b^3} \quad (6.11)$$

where w_b and L_b are the width and length of the piezoresistive beam, and t is the thickness of the structure. Assuming a linear relation between the frequency shift and the displacement of the piezoresistive beam, the change in frequency can be given by:

$$\Delta f = KX_{bTotal} \quad (6.12)$$

where K is a constant coefficient that depends on the stiffness of the piezoresistive beam among other factors, which can be determined experimentally. For a fixed magnetic field given to the Lorentz force beams, the value of the constant parameter K has been simulated to be 1.1×10^{10} Hz/m, 4.1×10^{12} Hz/m, and 7.2×10^{12} Hz/m for Type A, Type B, and Type C designs respectively. To estimate the input dynamic range of the magnetic field intensity for which the change in frequency is linear, Equation 6.9 was linearized mathematically. In a general case, if the term $(4BI_g/K_{lg})^2$ is less than 4.5×10^{-8} , the relationship between the output frequency shift and the input magnetic field is found to be linear with a 10% tolerance.

It is evident from Equation 6.9 and 6.12 that to maximize the sensitivity of the device, the length of the Lorentz force beam L_g needs to be maximized, and the Lorentz force stiffness K_{lg} and the piezoresistive beam stiffness K_{lb} need to be lowered.

6.4 PIEZORESISTIVE BEAM DESIGN

Figure 6.3 shows the schematic view of the different types of piezoresistive beams used in this work. A regular straight piezoresistive beam has been used to actuate the resonator in its in-plane

mode. To reduce the overall stiffness of structure, a curved beam, as opposed to a straight beam, was also designed. A lower stiffness beam has the advantage that the same amount of Lorentz force will cause a much larger displacement of the piezoresistive beam, modulating the stiffness further, consequently enhancing the sensitivity. However, reducing the stiffness increases the physical resistance of the structure, increasing the power consumption for the same operating current. Due to the inherent design of the Type C structure where the forces in the X and Y directions are equally distributed, coupling motions in both directions were observed distorting the in-plane resonance mode shape. To reduce the effect of the motion in the Y direction while maintaining the lower stiffness, Type B beam was designed as shown in Figure 6.3. Although coupling motions in X and Y directions will reduce the mechanical quality factor of the structure, it should be noted that the enhanced sensitivity is due to the influence of the much lower stiffness of the piezoresistive beam and the force amplification mechanism as explained earlier.

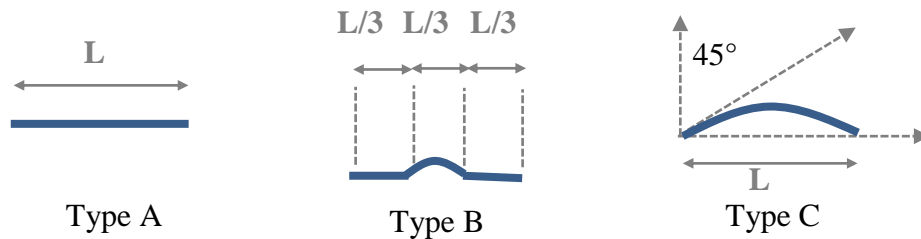


Figure 6.3. Schematic view of the different types of piezoresistive beams used in this work.

6.5 DEVICE FABRICATION

The monocrystalline silicon resonant structures of Figure 6.1 were fabricated on a SOI substrate (15 μm thick n-type 0.01 $\Omega\text{-cm}$ device layer, 2 μm thick buried oxide layer) using a three-mask micromachining process as shown in Figure 6.4. First, a thin layer of ~ 300 nm oxide was thermally grown on the silicon device layer. The oxide layer acts as an insulating layer between the Lorentz

force generator silicon beams and the metallic traces to be used for passing the Lorentz force current. This assures complete isolation between the Lorentz force current passing through the metal traces and the current used for thermal actuation of the resonator central beam. Due to the very low resistance of the metal traces, much higher currents can also be passed through the Lorentz force beams without increasing the power consumption to increase the device sensitivity. Photoresist (PR) is then patterned on the surface using Mask 1 to form the metal traces via lift-off. A 300 nm thick gold layer is deposited via e-beam evaporation and lift-off is performed leaving behind Lorentz force generator gold traces as shown in Figure 6.4(a). A thin layer of ~300nm low-temperature LPCVD oxide was then deposited to protect the metal layer during the fore-coming device layer etch step (Figure 6.4(b)). The silicon structure device layer patterns were then transferred onto the oxide mask (Mask 2). The handle layer was then patterned using Mask 3 from the backside and etched all the way to the buried oxide layer via Deep Reactive Ion Etching (DRIE) of silicon. The BOX layer was also dry etched from the backside as shown in Figure 6.4(c) to follow a fully dry process. The backside silicon etch not only allows access to the BOX layer using a dry process but also eliminates any stiction issues after device fabrication that such a long, low stiffness structure would be prone to. Finally, the device layer was etched via DRIE followed by dry etching of the oxide layer protecting the metal traces (Figure 6.4(d)).

Figure 6.5 shows the SEM views of all three fabricated magnetometers. The beam connecting the two resonator plates are fabricated with three different shapes with all other parameters in the structure remaining constant. Zoomed-in views of the 60 μ m long, 2 μ m wide piezoresistive beams are shown on the right-hand side which acts as the resonator thermal actuator in their respective structures. The long silicon beams covered with oxide isolated from the 300nm

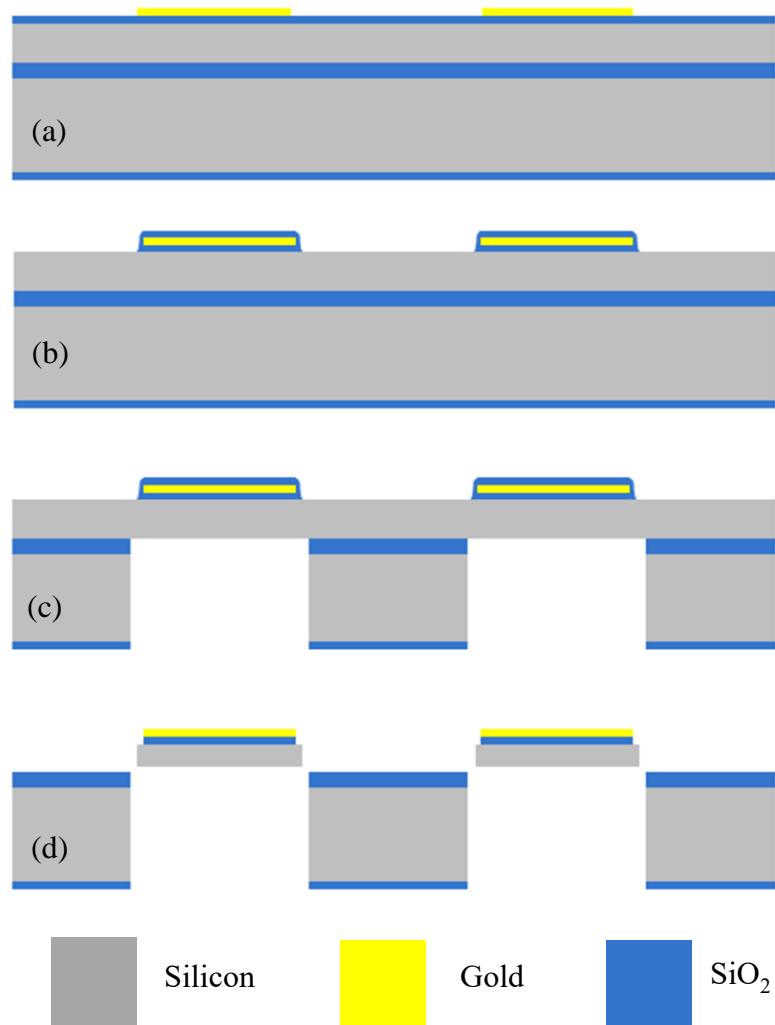


Figure 6.4. Process flow used for the fabrication of the Lorentz force magnetometer.

thick gold (Lorentz force beams) are 1500 μm each to increase the Lorentz force. Table 6.1 summarizes the force amplification factors due to the leverage mechanism, device dimensions, beam stiffness's in the in-plane and lateral directions, and the electrical parameters for all three designs tested in this work.

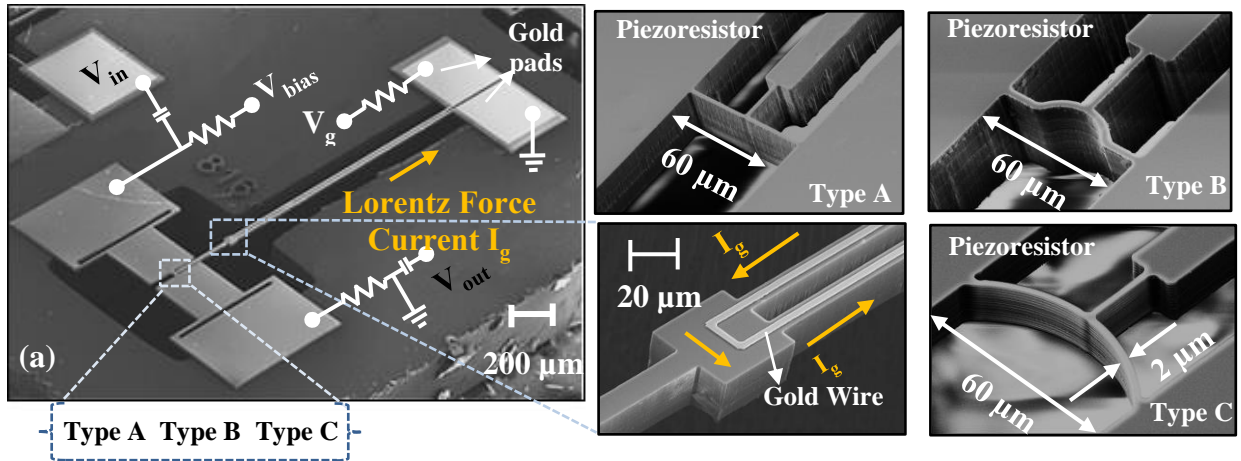


Figure 6.5(a). SEM view of the fabricated structure along with the test electrical connections. The piezoresistive beam has three different designs- Type A, Type B and Type C. Zoomed in views of all the piezoresistors are shown on the right-hand side.

6.6 MEASUREMENT RESULTS

6.6.1 MEASUREMENT SETUP

To test the fabricated device of Figure 6.5 as a frequency modulated magnetometer, a permanent magnet was used as the source of magnetic field. The magnetic field was varied by moving the magnet closer to/away from the device. Two separate, independent and non-interfering bias currents were provided to the device. V_{bias} along with an AC voltage V_{in} from the RF output of network analyzer was provided to the piezoresistive beam to actuate it in its in-plane resonance mode and V_g was applied across the gold trace for Lorentz force generation. Figure 6.5(a) shows the electrical connections used for testing the device. The ranges of currents for the thermal actuator and the Lorentz force current are summarized in Table I. The resonator frequency responses were obtained for different piezoresistor bias currents (I_{res}) and Lorentz force generator currents (I_g) for different magnetic fields generated by a strong permanent magnet kept at a specified distance from the device. The Lorentz force was thus varied not only by changing the distance of the magnet but also by changing the current in the Lorentz force beams.

Table 6.1. Device Properties, dimensions and electrical parameters for the Lorentz force magnetometer.

Parameter	Type A	Type B	Type C
Amplification Factor (Leverage mechanism)	 30	 55	 55
$K_{lateral}$ (beam) (N/m)	25906	13145	13297
$K_{extensional}$ (beam) (N/m)	101010	10152	9523
Resonator Plates ($\mu\text{m} \times \mu\text{m}$)	300×300	300×300	300×300
Piezoresistive Beam ($\mu\text{m} \times \mu\text{m}$)	60×2	60×2	60×2
Lorentz force beam length (μm)	1500	1500	1500
Gold Wire Width (μm)	4	4	4
Actuator current (I_{res}) (mA)	21-40	11-27	11-27
Gold Wire current (I_g) (mA)	0-10	0-8	0-17
Power required for Actuation (mW)	350-1000	120-730	145-875
Power required for Lorentz force generation (mW)	0-3	0-2	0-9

6.6.2 RESULTS

Figure 6.6 shows the measured frequency shifts under a fixed field of 0.3T for different resonator (I_{res}) and Lorentz force currents (I_g). The small shift in frequency observed at a Lorentz force current of 0mA is due to the Lorentz force generated by the resonator bias current itself. Due to the very large stiffness of the resonator beam, only shifts as small as ~22Hz were obtained for a resonator bias current of 40mA and a Lorentz force current of 10mA for an applied field of 0.3T. This translates to a sensitivity of 7.73ppm/mA.T for a baseline frequency of ~948kHz.

Figure 6.7 shows the resonant responses obtained from the device with Type B beam by applying different magnetic fields for a fixed resonator bias current of 27mA and Lorentz force current of 8mA, leading to a maximum frequency shift of ~7.6 kHz (~14,298 ppm) for a 0.3T field.

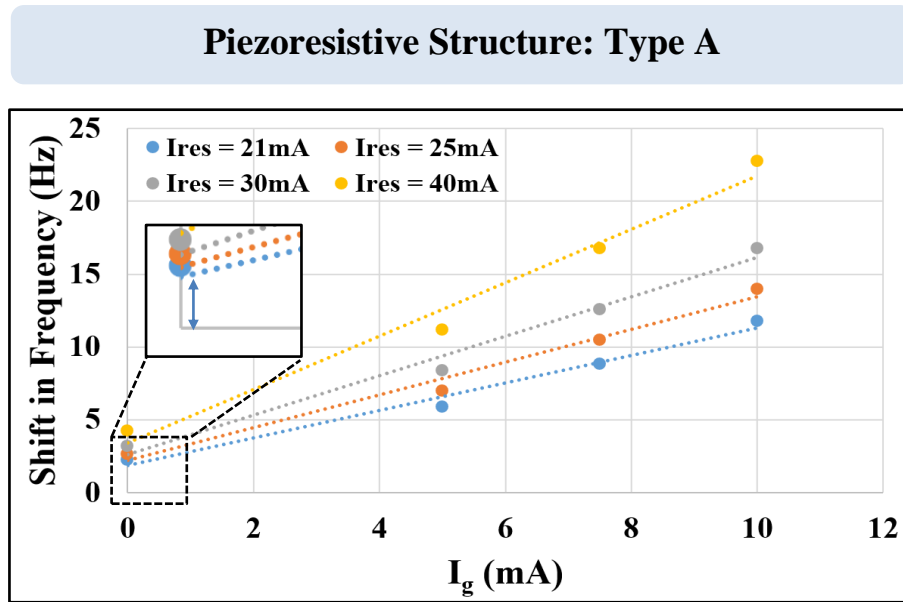


Figure 6.6. Overall Frequency shift under a constant field of 0.3T for different Lorentz force and resonator bias currents for Type A design.

Inset: The frequency shift at an I_g of zero due to the Lorentz force caused by the resonator bias current.

The frequency response was recorded for different magnetic fields by varying the distance of the magnet from the device. Figure 6.8 illustrates the frequency response of the same device for different Lorentz force currents while keeping the actuator bias current constant at 11mA. An increase in the Lorentz force current increases the Lorentz force and consequently the shift in the resonator frequency. It can be seen from Figure 6.7 and Figure 6.8 that different orientations of the magnetic poles result in opposite shifts due to change in the direction of the Lorentz force acting on the device. The sensitivity of the device is measured to be ~ 5957 ppm/mA.T with a baseline resonance frequency of ~ 532 kHz. Figure 6.9 shows the measured frequency shifts under a fixed field of 0.3T for different resonator (I_{res}) and Lorentz force currents (I_g). Figure 6.10, 6.11 and 6.12 show the similar resonance responses of the structure having Type C piezoresistive beam as shown for the previous device. For a 0.3T magnetic field, a maximum frequency shift of 12.85 kHz ($\sim 36,800$ ppm) has been obtained from the completely curved piezoresistive beam device (Type C) operating at a fixed resonator bias current of 27mA and Lorentz force current of 17mA. The sensitivity of the device is measured to be ~ 7200 ppm/mA.T with a baseline resonance frequency of ~ 349 kHz which is $\sim 950X$ larger than the Type A structure. This is mainly because of the amplified Lorentz forces on the less stiff beam of the Type C structure.

The intrinsic quality factors for the Type A, Type B, and Type C structures were measured to be ~ 1452 , ~ 1328 , and ~ 1010 respectively. The decrease in the quality factor in the Type B and Type C designs is due to the presence of the coupling motions in the X and Y directions of the piezoresistive beams. Although the quality factors in Type B and Type C designs are $\sim 1.1X$ and $\sim 1.5X$ lesser than the Type A design, the sensitivity in Type B and Type C structures is $\sim 780X$ and $\sim 950X$ better than Type A. Therefore, the overall minimum detectable field in Type B and

Piezoresistive Structure: Type B

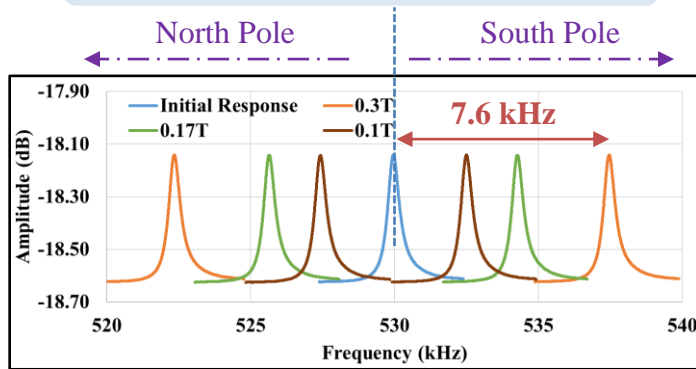


Figure 6.7. Type B- Measured resonance responses under different magnetic field intensities for a fixed Lorentz force current of 8mA and resonator bias current of 27mA.

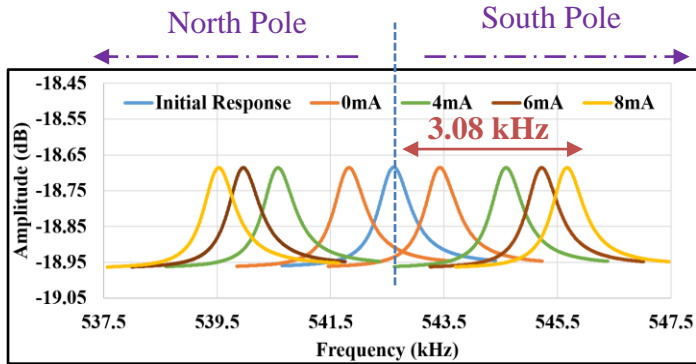


Figure 6.8. Type B- Resonance responses for different Lorentz force currents under constant field of 0.3T and resonator bias current of 11mA.

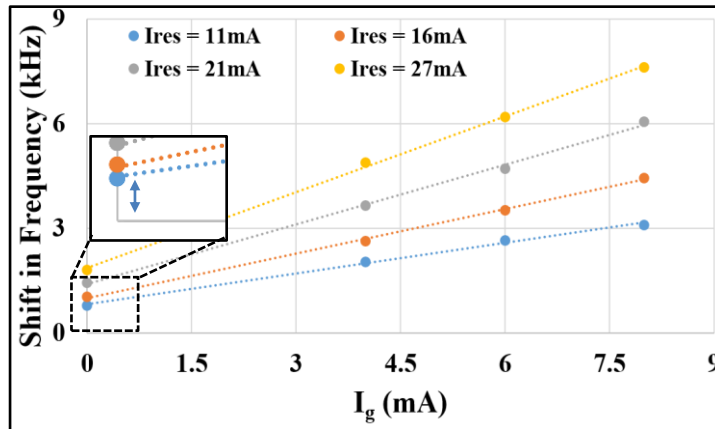


Figure 6.9. Type B- Overall Frequency shift under a constant field of 0.3T for different Lorentz force and resonator bias currents.
Inset: The frequency shift at an I_g of zero due to the Lorentz force caused by the resonator bias current.

Piezoresistive Structure: Type C

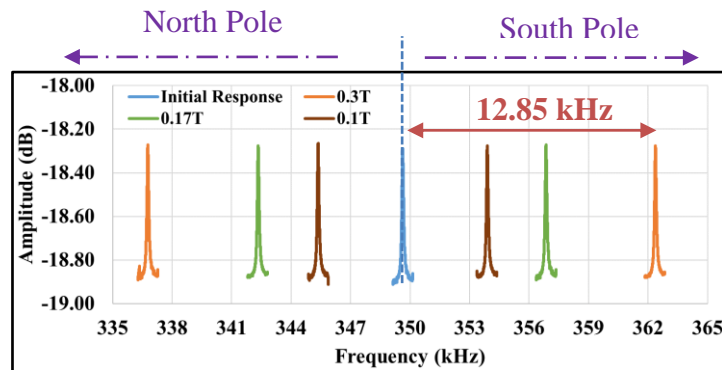


Figure 6.10. Type C- Measured resonance responses under different magnetic field intensities for a fixed Lorentz force current of 17mA and resonator bias current of 27mA.

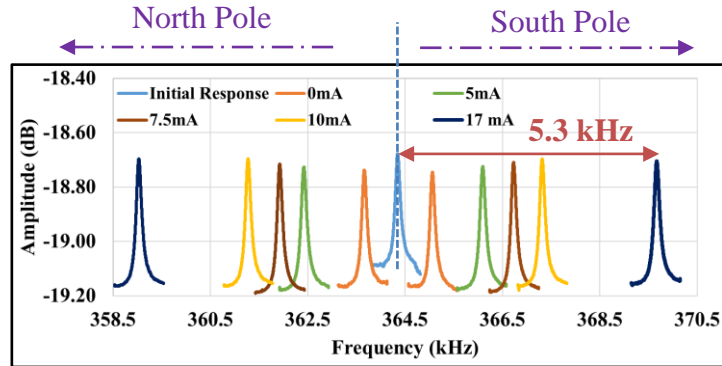


Figure 6.11. Type C-Resonance responses for different Lorentz force currents under constant field of 0.3T and resonator bias current of 11mA.

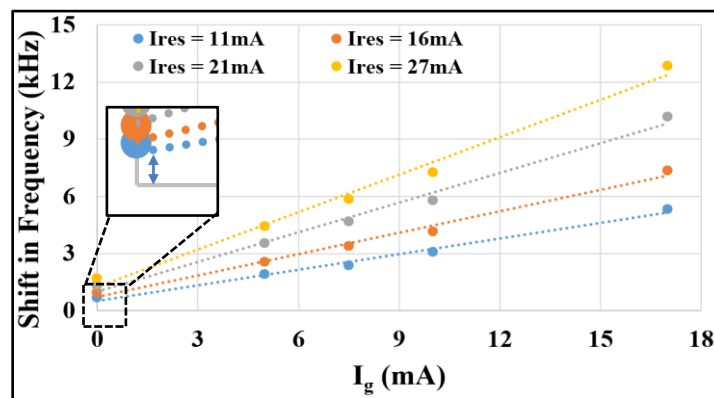


Figure 6.12. Type C- Overall Frequency shift under a constant field of 0.3T for different Lorentz force and resonator bias currents. Inset: The frequency shift at an I_g of zero due to the Lorentz force caused by the resonator bias current.

Type C structures is still ~700X and ~630X better than the Type A design. Based on the linearization of Equation 6.9, the input magnetic field intensity for which the output frequency will have a linear relationship with it for the Type C design (best sensitivity) is found to be between 0T and 0.5T. It should be noted that the sensitivities for all three different sensors were measured in the resonance mode of the device. An important criterion for putting such devices into self-oscillation is by obtaining higher gains (g_m) upon increasing the I_{res} current [81]. However, the device designs were not intended to achieve self-oscillation but only show as a proof of concept, the force amplification mechanism. Self-oscillation can be achieved by scaling down the dimensions of the piezoresistive beams to obtain larger vibration amplitudes (and thus higher g_m 's) for the same amount of bias current as shown in work [81]. Using a much larger load resistance (instead of the 50-ohm load used in this work) can also facilitate self-oscillation for the designs shown in this work.

The sensitivity values show a good agreement with its simulated finite static force analysis values as shown in Table 6.2. The slight change in sensitivities could be due to any errors that might have occurred during fabrication. Table II also compares this work to some of the other works on Lorentz force MEMS magnetometers with frequency modulated output.

6.6.3 NOISE ANALYSIS

To measure the drift in the resonance frequency due to thermal actuation, the short-term noise floor was measured for about 30 minutes by examining the output operating with a large IFBW of 400Hz in the absence of the external field. Figure 6.13(a) and (b) illustrate the measured standard deviation in the resonance frequency of the device for different resonator bias currents for Type A, B, and C. Type A device is most stable due to its perfectly symmetric structure. Type

Table 6.2. Comparison of FM Lorentz Force Magnetometers.

FM Sensor	PARAMETER		
This work Type A	fo	II Max	Measured Sensitivity
	948 kHz	10 mA	7.73 PPM/mA.T
	Measured Drift	Measured Noise	Simulated Sensitivity
	2.27 Hz	0.12 PPM/ $\sqrt{\text{Hz}}$ 1581 $\mu\text{T}/\sqrt{\text{Hz}}$	8.08 PPM/mA.T
This work Type B	fo	II Max	Measured Sensitivity
	532 kHz	8 mA	5960 PPM/mA.T
	Measured Drift	Measured Noise	Simulated Sensitivity
	6.83 Hz	0.64 PPM/ $\sqrt{\text{Hz}}$ 13.54 $\mu\text{T}/\sqrt{\text{Hz}}$	6324 PPM/mA.T
This work Type C	fo	II Max	Measured Sensitivity
	349 kHz	17 mA	7220 PPM/mA.T
	Measured Drift	Measured Noise	Simulated Sensitivity
	11.85 Hz	1.69 PPM/ $\sqrt{\text{Hz}}$ 13.81 $\mu\text{T}/\sqrt{\text{Hz}}$	7446 PPM/mA.T
Li et al. [26]	fo	II Max	Measured Sensitivity
	105 kHz	0.9 mA	5270 PPM/mA.T
	Measured Noise		
	0.5 $\mu\text{T}/\sqrt{\text{Hz}}$		

Table 6.2. (continued) Comparison of FM Lorentz Force Magnetometers.

FM Sensor	PARAMETER		
Zhang et al [24]	fo 47.2 kHz	Il Max 10 mA	Measured Sensitivity 21.5 PPM/mA.T
	Measured Noise 20PPB 9 μT		
Li et al [25]	fo 21.9 kHz	Il Max 4 mA	Measured Sensitivity 6750 PPM/mA.T
	Measured Noise 0.5 PPM/√Hz 20 μT/√Hz		

B and Type C designs are less stable due to their imperfect in-plane resonance mode and any asymmetry in the piezoresistive beam that might have occurred during fabrication. The Brownian limited resolution for such a design is given by [52]:

$$B = \frac{\sqrt{4k_b T b}}{IL} \quad (6.13)$$

where k_b is the Boltzmann constant ($1.38E-23 \text{ m}^2\text{kgs}^{-2}\text{K}^{-1}$), T is the absolute temperature, I is the bias current, L is the length of the beam and b is the damping coefficient. The theoretical Brownian limited resolution for the Type-C beam is found to be $\sim 0.18\text{PPM}$ for a 1 Hz bandwidth which is $\sim 10\text{X}$ smaller than the measured noise floor. Therefore, it is believed that the electronic noise dominates the noise floor in the setup. One of the prominent factors contributing to the electronic

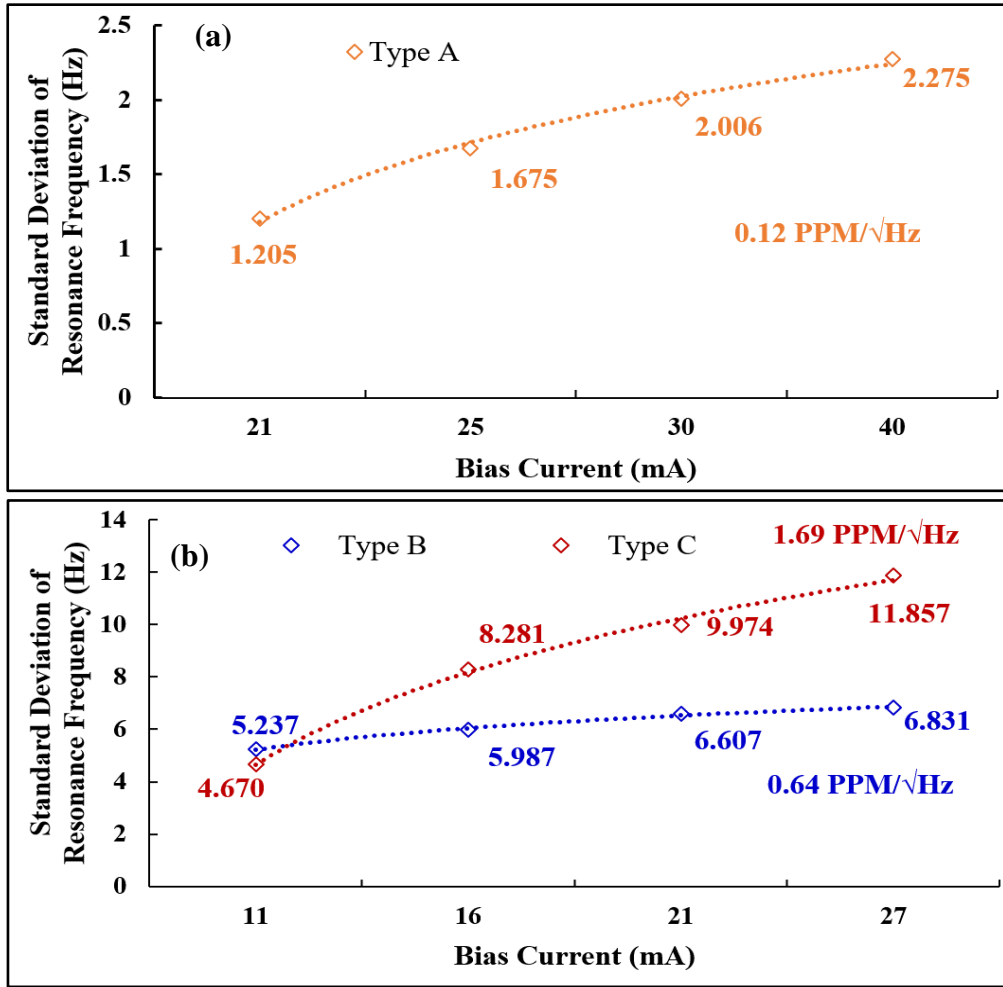


Figure 6.13.(a) (b). Measured standard deviations of the resonance peak frequency at various bias currents for Type A, B and C designs.

noise is the physical resistance of the piezoresistive beam. Since the Type C beam has a larger resistance than the Type A and Type B design, the Type C structure exhibits the largest noise floor among the three structures (in terms of PPM/ $\sqrt{\text{Hz}}$). However, when this value is converted to a $\mu\text{T}/\sqrt{\text{Hz}}$ value, due to the very slight difference between the sensitivities of Type B and Type C design, the noise floor for the Type B design is slightly lesser than the Type C in design (in $\mu\text{T}/\sqrt{\text{Hz}}$). One possible reason for only a slight improvement in the Type C design when compared

to the Type B design is the larger coupling motion in the Y direction for the Type C design which gives it a slightly more distorted resonance mode.

6.6.4 TEMPERATURE COMPENSATION

Axial loading due to temperature variations is clearly an issue in the Type B and Type C designs. If we increase or decrease the operating temperature, an extra component of force will be created in the Lorentz force beams due to the presence of the gold and oxide layers. The combination of the layers will cause an extra component of stress in the Lorentz force beams which will contribute to the sensitivity/resolution of the sensor. Due to the opposing nature of the effect of TCF of gold and the oxide layer on silicon, the combined TCF of the gold-oxide layer can be optimized (by adjusting the thickness of the deposited gold and oxide layers) to cancel out the effect of the TCF of the silicon layer. However, the stiffness of the gold-oxide layer needs to be considered as well and the best optimal thickness combination needs to be utilized to negate the effect of TCE (Temperature Coefficient of Young's Modulus) of the gold and oxide layers. Therefore, the only effect of temperature present would be the TCE of silicon, which is inherently exhibited in all silicon resonators and can be compensated for by doping the sensor with high concentrations of an n-type dopant as shown in work [79].

CHAPTER 7

LOW POWER, WIDEBAND, CMOS COMPATIBLE MEMS VIBRATION SENSORS

7.1 PRINCIPLE OF OPERATION

The proposed approach is based on utilizing the electronic chip itself as the mechanical component responding to vibrations in form of slight bending that leads to tensile and compressive stresses at different locations on the chip surface. Figure 7.1 shows a simplified view of the proposed chip assembly. To increase sensitivity of the sensors it may be needed that the processed CMOS chips are thinned down to $\sim 50\text{-}100\mu\text{m}$ in order to make them more compliant so that the stress induced on the surface due to vibrations increases. As shown in Figure 7.1, a flip-chip bonded substrate bridges between solder bumps on the two sides leaving behind a cavity at the center of the chip. An additional mass may or may not be needed to be added to the backside of the chip for increased sensitivity. This mass can be a high density metallic piece simply glued or bonded to the backside of the chip or could be an electroplated thick film (tens of microns thick). The exaggerated view of Figure 7.1 shows bending of the chip due to vertical acceleration applied to the chip caused by vibrations. Bending of the chip in the shown direction induces tensile stress to the chip surfaces closer to the edge, and compressive stress to the surfaces towards the middle of the chip. This can be utilized to perform differential measurements in a Wheatstone bridge configuration to cancel the effect of temperature drift and other undesirable environmental parameters.

7.2 STRESS SENSING

The most conventional way to sense stress is by utilizing on-chip piezoresistors. Although any on-chip resistor can act as a piezoresistor, crystalline silicon offering much higher

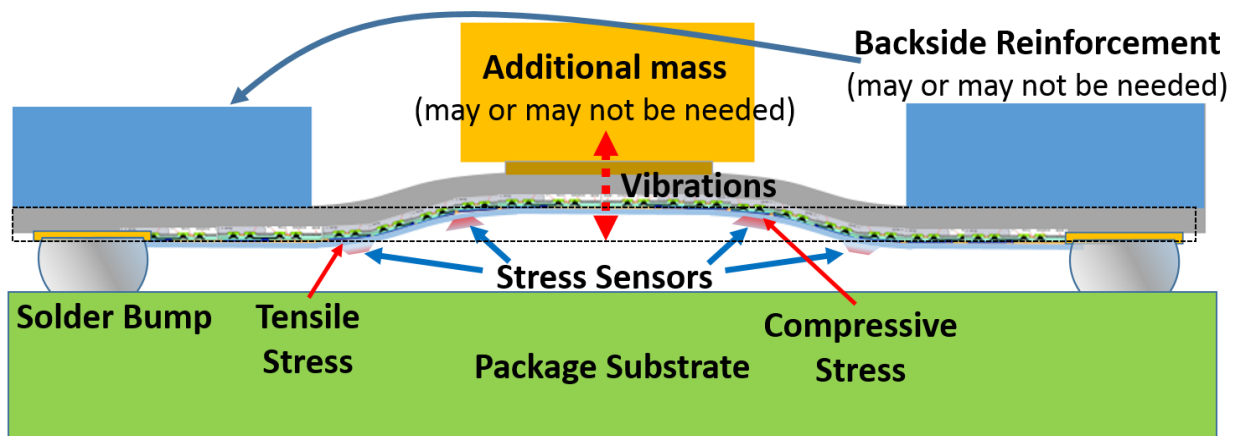


Figure 7.1. Schematic view of the single chip vibration sensor that utilizes a standard CMOS process to implement stress sensors. The thinned down silicon substrate turns vibrations into surface stress (compressive and tensile) that is detected by n-well or p-well silicon piezoresistors within the CMOS chip designed in a Wheatstone's bridge fashion.

piezoresistivity compared to polysilicon and metal alloys would be an ideal choice. Crystalline silicon piezoresistors can be formed in p-wells or n-wells within the CMOS chip, or using MOS transistor channels. The piezoresistors will be arranged in a Wheatstone bridge configuration with two resistors closer to the mounting edges of the chip and the other two closer to the central part of the chip where the maximum bending occurs. In this manner, the two-resistor pair will undergo opposite polarity of stresses due to vibrations and the output can be measured differentially.

7.3 MECHANICAL DESIGN AND THEORETICAL ANALYSIS

A suitable TI based CMOS process was thoroughly studied to envision the process flow, design rules and system requirements for fabricating the low power vibration sensor. Extensive simulations were performed to determine optimal chip dimensions, mounting and other design parameters. To gain hands-on experience with the chosen TI process, a simple test structure with piezoresistive material located at the maximum stress points was designed. The chip dimensions and other design parameters (resistor lengths and widths) were chosen taking into consideration

not just the sensitivity and bandwidth of the sensor but also the TI-CMOS process platform design specifications.

Figure 7.2 shows the COMSOL simulation of a very simple CMOS compatible test structure. The test structure is simply the entire CMOS structure with piezoresistors located close to the fixed end of the CMOS chip. On applying a vibration, the CMOS chip would bend, thus modulating the resistance of the piezoresistor. A $2\text{mm} \times 2\text{mm} \times 200\mu\text{m}$ silicon chip is chosen for this purpose so that the requirements of the TI fabrication process are met. On applying a vibration amplitude of 1mg at DC, a PPM shift of 1.2×10^{-4} is obtained for the device with the resonance frequency at $\sim 67\text{kHz}$. Figure 7.2(b) shows the stress profile for such a design and it is evident that the device is not sensitive enough to measure vibrations in the mg range.

To enhance the sensitivity of the device, a high-density mass (Copper mass assumed in simulations) was then added at the edge of the chip as shown in Figure 7.3. Adding the Copper mass not only reduced the resonance frequency of the device from $\sim 67\text{kHz}$ to $\sim 23\text{kHz}$, the

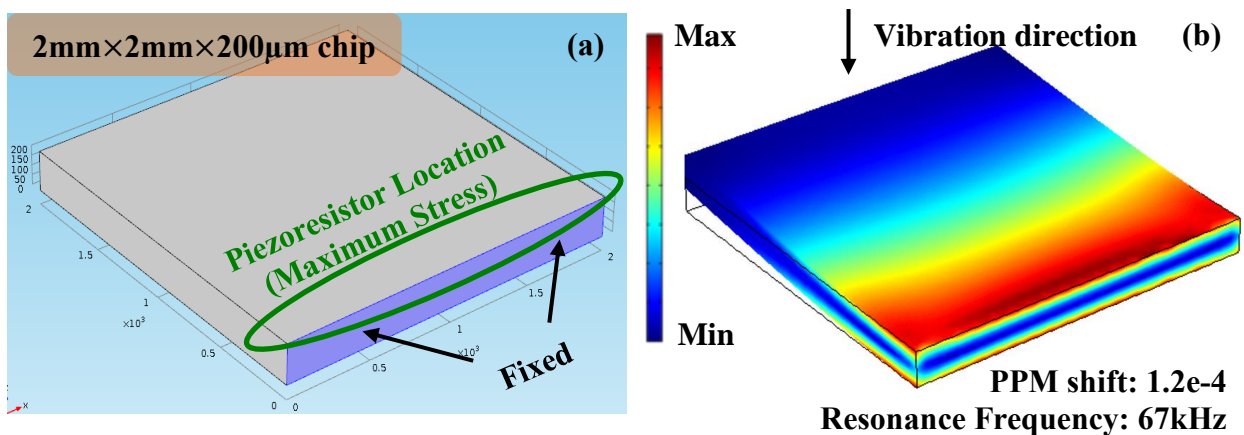


Figure 7.2.(a). Simple piezoresistive cantilever -based vibration sensor.
 (b). COMSOL modal analysis showing stress profile on application of a 1mg vibration at DC.

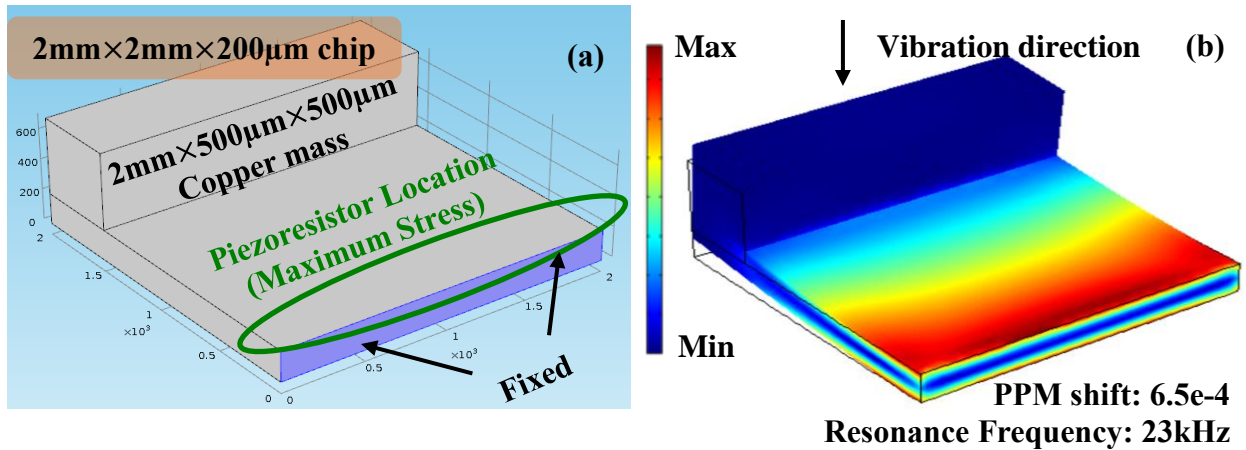


Figure 7.3.(a). Simple piezoresistive cantilever-based vibration sensor with added mass.
 (b). COMSOL modal analysis showing stress profile on application of a 1mg vibration at DC.

sensitivity of the device was improved by $\sim 4X$ to 6.5×10^{-4} PPM, which still isn't detectable by using regular electronics.

To boost the sensitivity of the device further, a deep trench was added on the backside of the electronic chip exactly underneath the piezoresistor where stress on the chip due to vibration would be maximum as shown in Figure 7.4. The sensitivity of the device was enhanced by $\sim 100X$ to 0.07PPM for a 1mg vibration at DC. In this case, although the sensitivity was significantly enhanced, the resonance frequency dropped to $\sim 450\text{Hz}$. The frequency response for the device shown in Figure 7.4 is illustrated in Figure 7.5(a). Although the device shows a decent measurable sensitivity for vibrations $< \sim 500\text{Hz}$, the sensitivity drastically reduces past the resonance frequency of the device. Thus, there is a tradeoff between the bandwidth and the sensitivity of the vibration sensor which exists in most traditional vibration sensors as well as shown in Figure 7.5(b). Thus, this technique of creating a single trench would have sufficient sensitivity only for a narrow bandwidth depending on the Quality factor of the sensor.

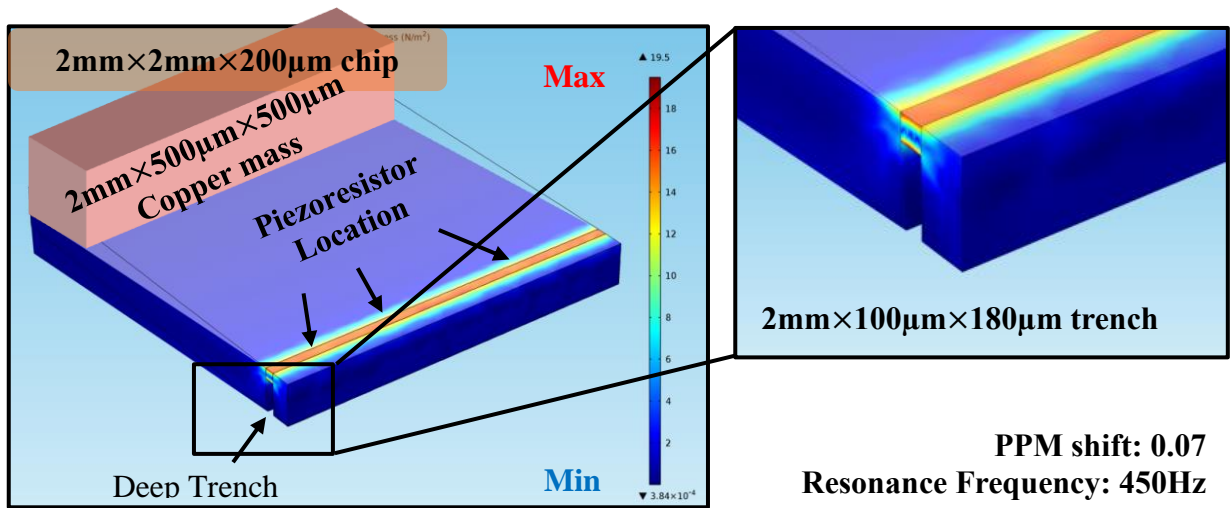


Figure 7.4. COMSOL modal analysis showing stress profile on application of a 1mg vibration at DC for a device with added mass and deep trench under the piezoresistor.

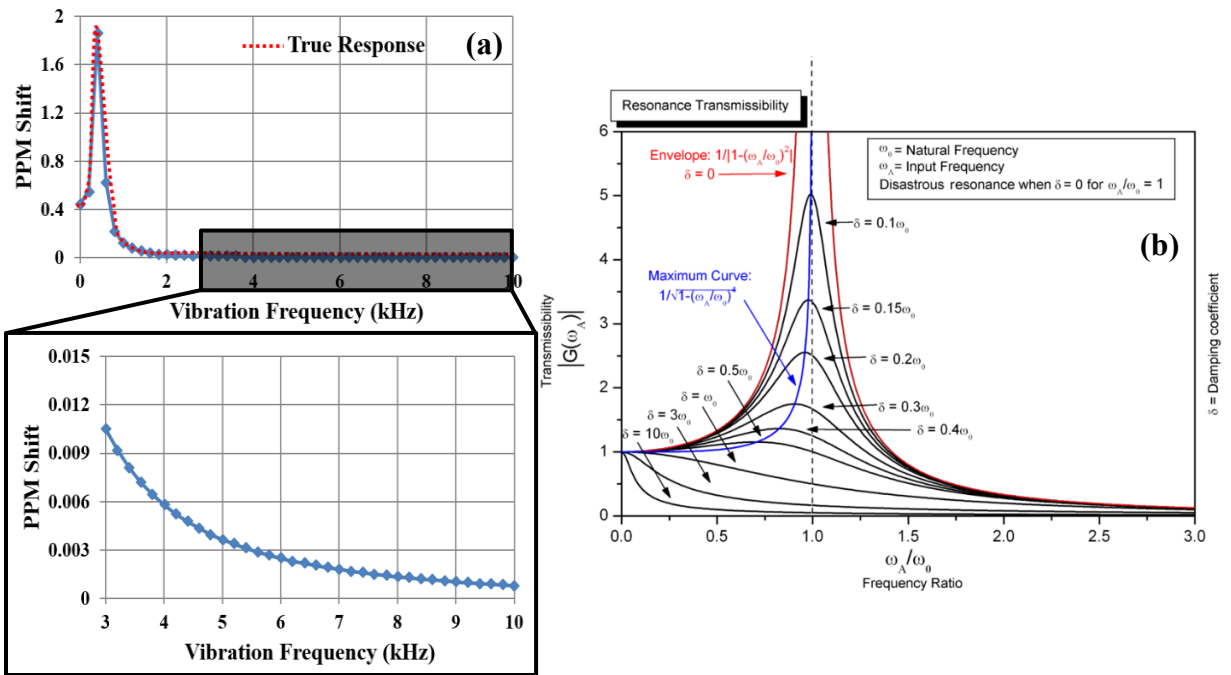


Figure 7.5(a). Resonance response of the vibration sensor with the attached mass and backside trench.

(b). Trade-off between bandwidth and sensitivity of the device.

One of the potential solutions for solving the bandwidth-sensitivity trade-off is by introducing multiple trenches on the backside of the CMOS chip. Figure 7.6(a) shows the structure of the device with two trenches positioned to have a wider bandwidth (two resonance modes as shown) as compared to devices shown in Figures 7.2 to Figure 7.4. Figure 7.6(b) shows the resonance response of the device for a vibration of 1mg applied to it. However, by implementing this technique, the sensitivity and the bandwidth would depend on the dominance/strength of its respective frequency mode. Another similar technique that could be implemented to increase the bandwidth of such sensors is by utilizing a masked etch process for the silicon back-side of the

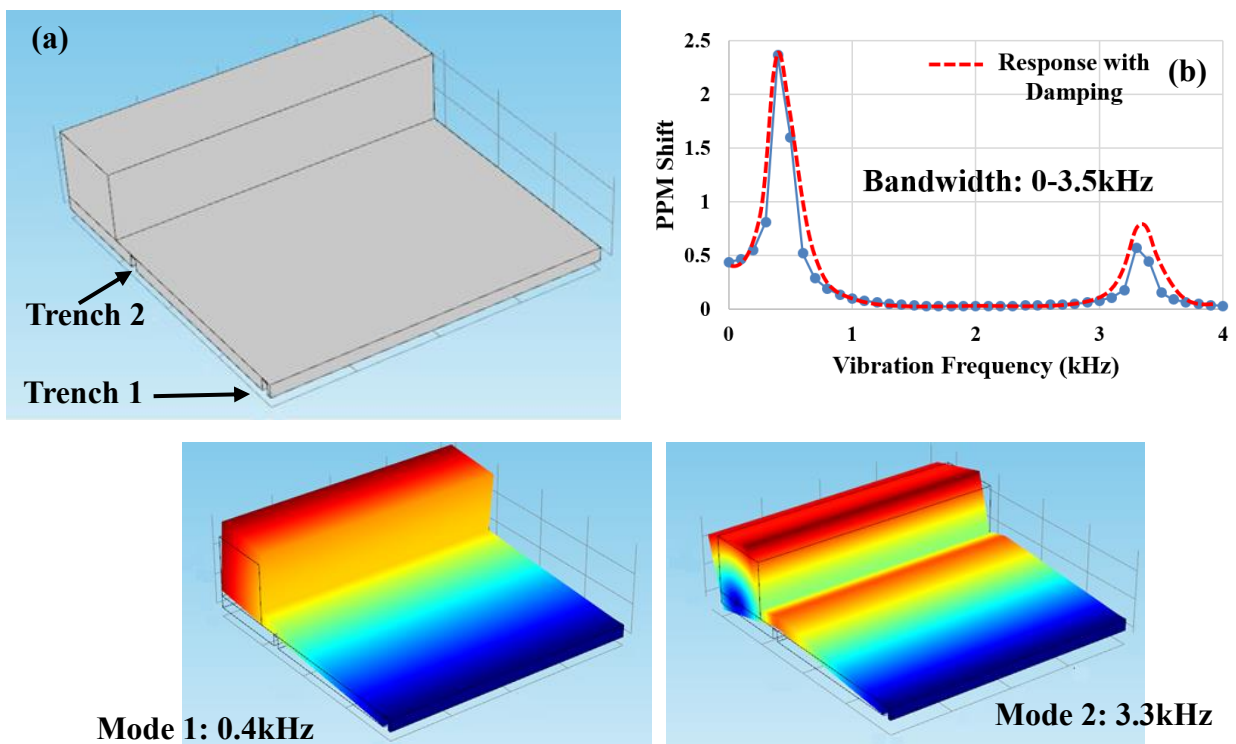


Figure 7.6.(a). Device structure with multiple modes/trenches for wider bandwidth operation along with their respective mode shapes.
 (b). Resonance response of the device for a vibration of 1mg.

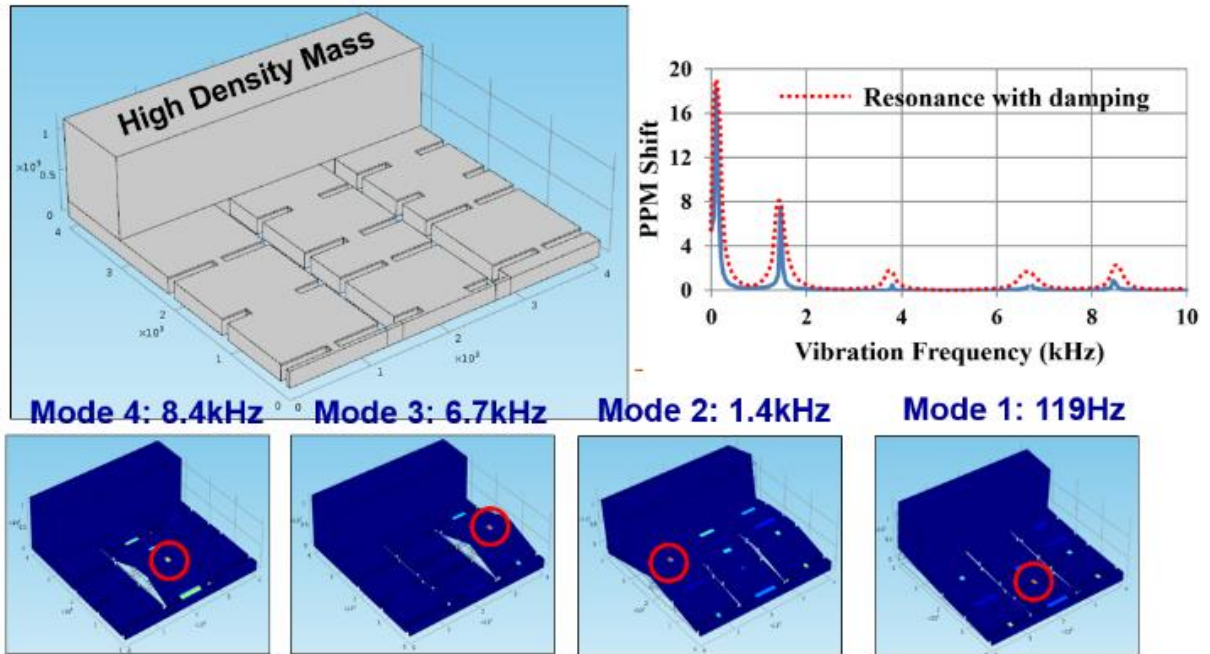


Figure 7.7. Multiple trenches on the back-side of the CMOS chip enabling wider bandwidth of operation.

CMOS chip. This would enable multiple resonance modes on the same chip increasing the bandwidth of the device as shown in Figure 7.7.

7.4 ASSOCIATED TERMS AND MATHEMATICAL ANALYSIS

Some associated terms to understand the dependence of the physical dimensions on the sensitivity of the sensor are explained in this section. They were then utilized to optimize the design of the sensor.

The stiffness of the cantilever k is given by

$$k = \frac{Ewt^3}{4L^3} \quad (7.1)$$

Where E is the Young's Modulus of Silicon (usually 130-170 GPa), w is the width of the cantilever, t is the thickness of the cantilever and L is the length of the cantilever.

The resonance frequency f for such a cantilever is given by

$$f = \frac{1}{2\pi} \sqrt{\frac{k}{m_c}} \quad (7.2)$$

Where m_c is the mass of the cantilever ($m_c = Lwt \times \text{Density of silcion}$)

Since we have an added mass at the free end of the cantilever which is much larger than the cantilever itself, the force due to acceleration/vibration can be considered as a point force. The maximum stress on a bent cantilever due to an applied point force F is given by

$$\sigma_{max} = \frac{6LF}{wt^2} \quad (7.3)$$

Where $F = ma$ where a is the amplitude of acceleration/vibration and m is the mass of the added mass ($m = L_m \times w_m \times t_m \times \rho$). Here, L_m is the length of the added mass, w_m is the width of the added mass, t_m is the thickness of the added mass and ρ is the density of the material of the added mass. The change in resistance of the Whetstone's bridge network can be written as

$$\Delta R = R\sigma_{max}\pi_l \quad (7.4)$$

Where R is the resistance and π_l is the piezoresistive coefficient of Silicon.

The change in the output voltage can be then written as

$$\Delta V = \Delta R \times I_{dc} \quad (7.5)$$

Where I_{dc} is the current passing through the resistor due to bias voltage V_{bias}

The sensitivity for the sensor can be defined as the ratio of the change in voltage to the applied acceleration which can be written as

$$\text{Sensitivity } S = \frac{\Delta v}{a} \quad (7.6)$$

Substituting the value of Δv from the previous equations, sensitivity S can be written as

$$S = \frac{6\pi_l m L V_{bias}}{wt^2} \quad (7.7)$$

It is evident from Equation 7.7 that sensitivity can be increased by increasing the mass of the added mass, length of the cantilever, the input bias voltage or by reducing the thickness or the width of the cantilever structure.

7.5 INITIAL TEST CHIP FABRICATION

Figure 7.8 shows the images of the CMOS chip (2mm×2mm×240μm) and the optical microscopic images of the vibration sensor fabricated at Texas Instruments in a standard CMOS process. Both silicon n-wells and Silicon-Chrome (SiCr) piezoresistors were utilized in Wheatstone's Bridge network. Although SiCr has a piezoresistive coefficient ~5-10X less than regular silicon n-wells (thus reducing the sensitivity), they are more temperature stable than

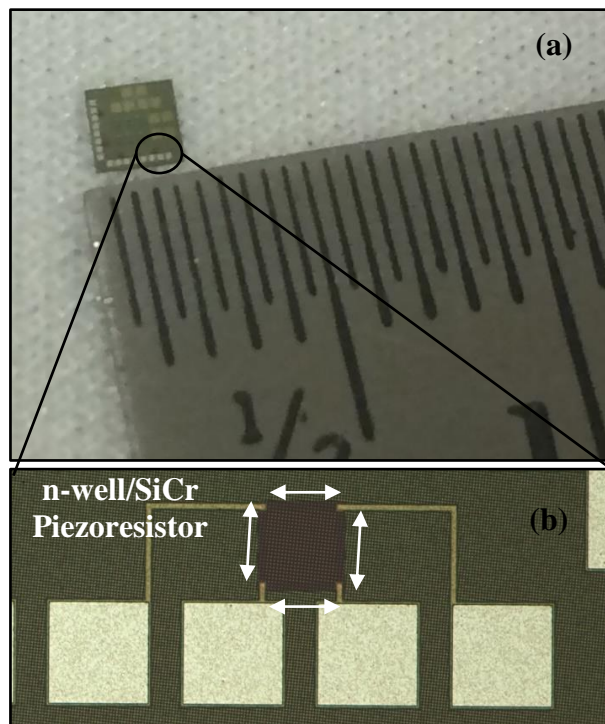


Figure 7.8.(a). 2mm× 2mm CMOS chip.
(b): Optical microscopic image of the CMOS Vibration Sensor.

silicon, thus allowing a wider temperature range of operation. Once the chips were received, markers were created on the backside of the CMOS chip exactly underneath the piezoresistors using FIB (Focused ion beam). Trenches were then created along this marker using a laser beam as shown in Figure 7.9. The sample needed to be exposed to the laser multiple times to thin down the sample to $\sim 80\ \mu\text{m}$. Due to the very high intensity of the laser, some samples would break during exposure rendering the process impractical and the sensors inoperable. Using a lower intensity would resolve this issue but the process would be extremely time consuming. To overcome such complications, the entire chip was thinned down to about $\sim 80\ \mu\text{m}$ using a mask-less DRIE (Deep reactive ion etching) process as shown in Figure 7.10.

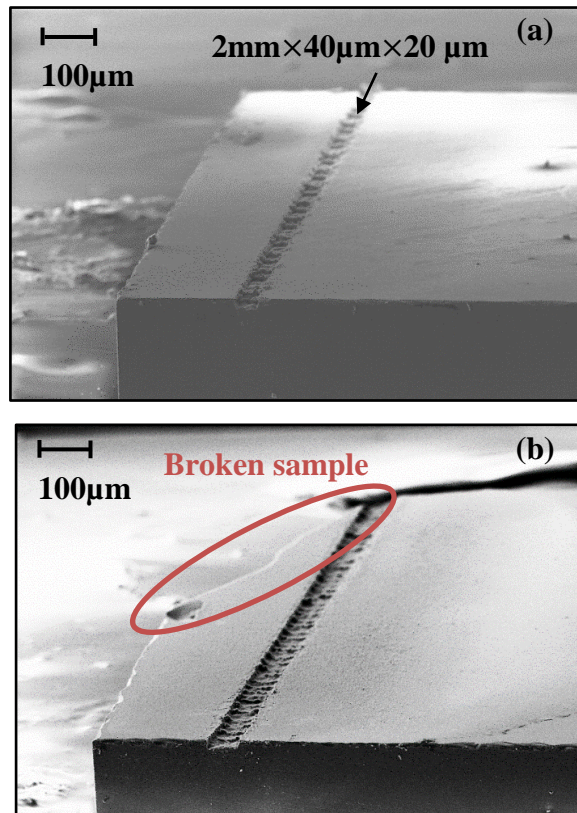


Figure 7.9.(a). Right: Trench created by laser on the back-side of the CMOS chip
(b). Broken sample due to high intensity of laser.

A bulky mass made of solder wire (~156mg) was then attached to the edge of the chip using high quality glue. The location and magnitude of the solder mass influences the resonance frequency of the chip. The chip was then carefully attached to the edge of a stiff object with glue and wire-bonded once the setup was dry as shown in Figure 7.11.

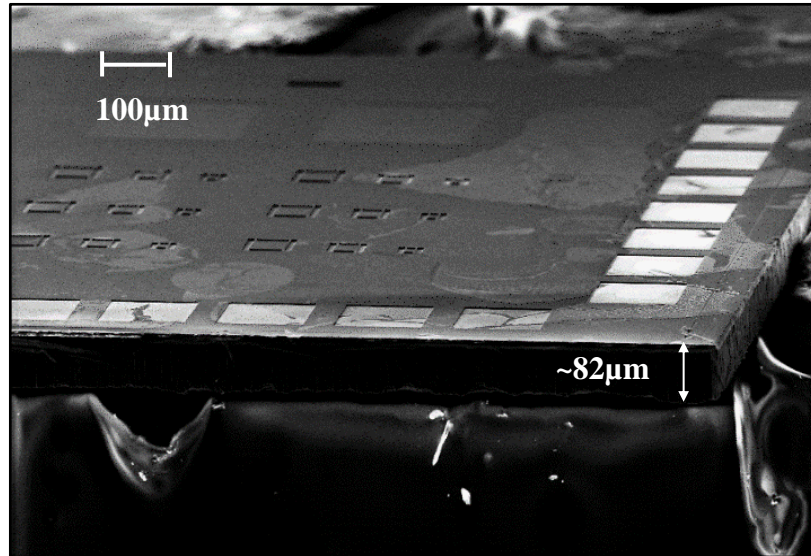


Figure 7.10. SEM view of the CMOS chip thinned down to ~80 μm.

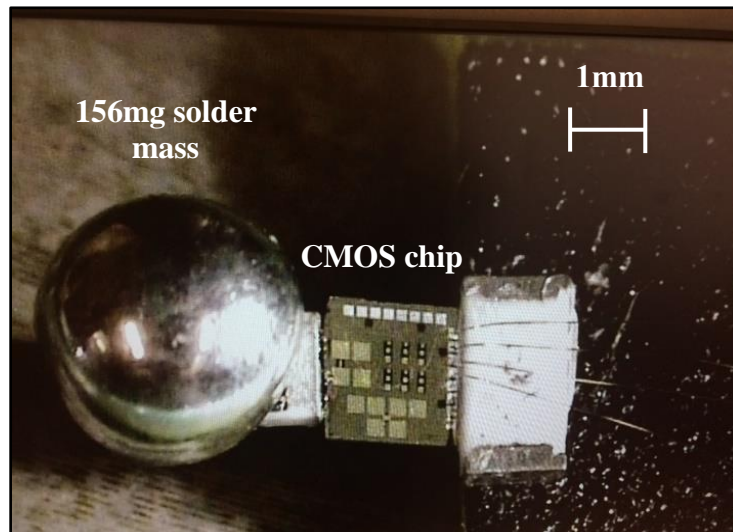


Figure 7.11. Experimental setup for the suspended thinned down CMOS chip.

7.6 PRELIMINARY TEST RESULTS

Static test was first performed by simply rotating the PCB (Printed Circuit Board) to different angles, thus varying the acceleration, i.e., vibration at 0Hz. Due to the very high noise floor level of the sensor, a 24bit ultra low noise analog to digital converter (ADS1232) was used to measure the changes in the output voltage. An internal power supply of 5V was given from the ADS1232 to the device. Figure 7.12 illustrates the measured output voltage changes for different angles of the PCB. A sensitivity of $\sim 4.5\text{mV/g}$ is obtained for such a design having n-well piezoresistors with a 156mg mass. A similar test was performed for the SiCr piezoresistors located on the same CMOS chip with the same attached mass. Although, temperature stability measurements were not performed, the sensitivity obtained from the SiCr vibration sensors was $\sim 0.9\text{mV/g}$ as shown in Figure 7.13.

To measure the effect of vibration on the CMOS chip, a speaker/sub-woofer was used to create sinusoidal vibrations at different frequencies using a PC. An off-the-shelf commercial Analog Devices Vibration sensor (ADIS16228) was used to measure the amplitude of the generated vibrations. Both the sensors were placed in a cardboard box for uniform vibrations to be transferred to the sensors. The entire experimental setup for the measurement of vibrations is shown in Figure 7.14.

The vibration amplitude generated by the PC was measured in g's for every frequency between 35Hz and 800Hz by using the Analog Devices sensor. The change in output voltage of the CMOS chip because of the vibrations on the piezoresistors was also recorded. The resonance peak of the device was obtained at $\sim 240\text{Hz}$ as shown in Figure 7.15. Since the output of the analog

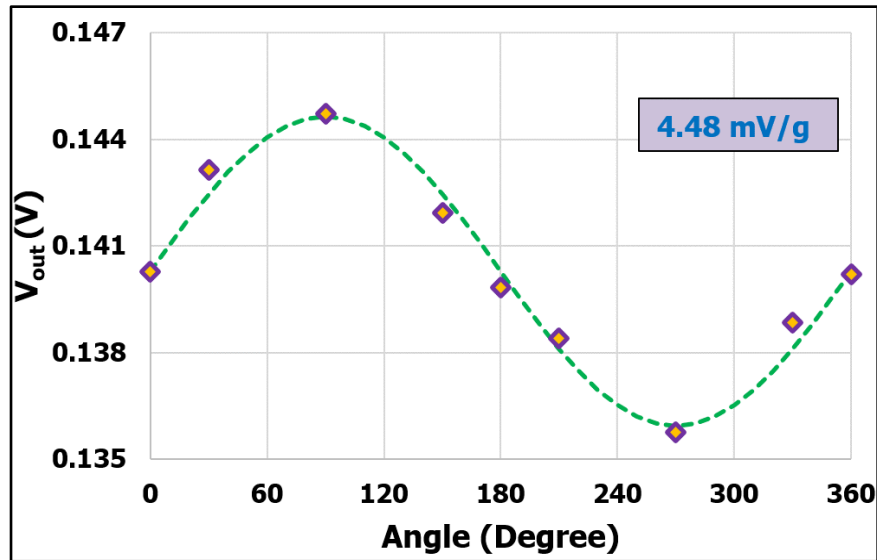


Figure 7.12. Measured output voltage for various angles/accelerations of the PCB with respect to the horizon for a silicon n-well piezoresistor.

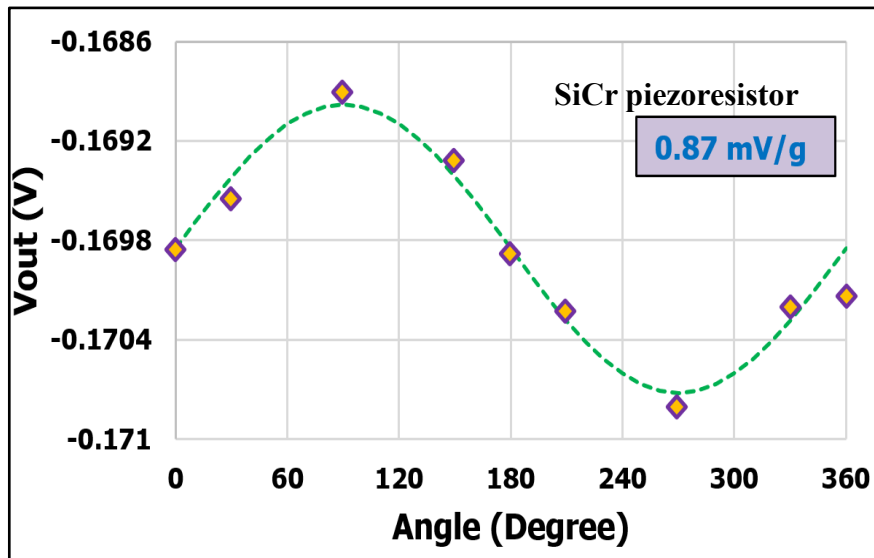


Figure 7.13. Measured output voltage for various angles/accelerations of the PCB with respect to the horizon for a SiCr piezoresistor.

devices sensor is in g's and the output of the TI fabricated CMOS chip is in mV's, 1g of measured vibration was assumed to be 1mV of output to compare the frequency responses of both the sensors. Figure 7.15 shows frequency response of both the sensors normalized to 1g of vibration.

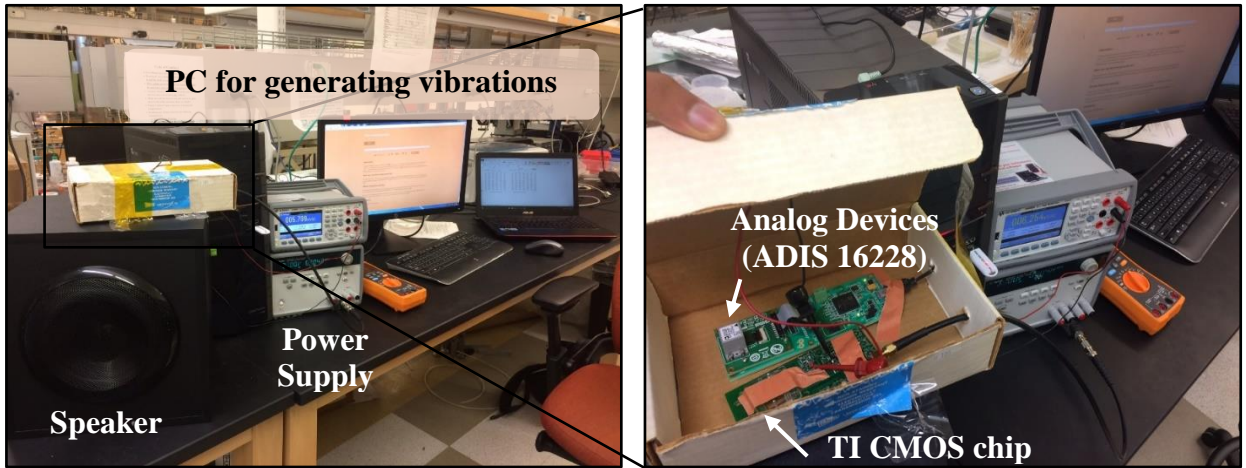


Figure 7.14. Experimental setup for measuring the effect of vibrations on CMOS vibration sensor.

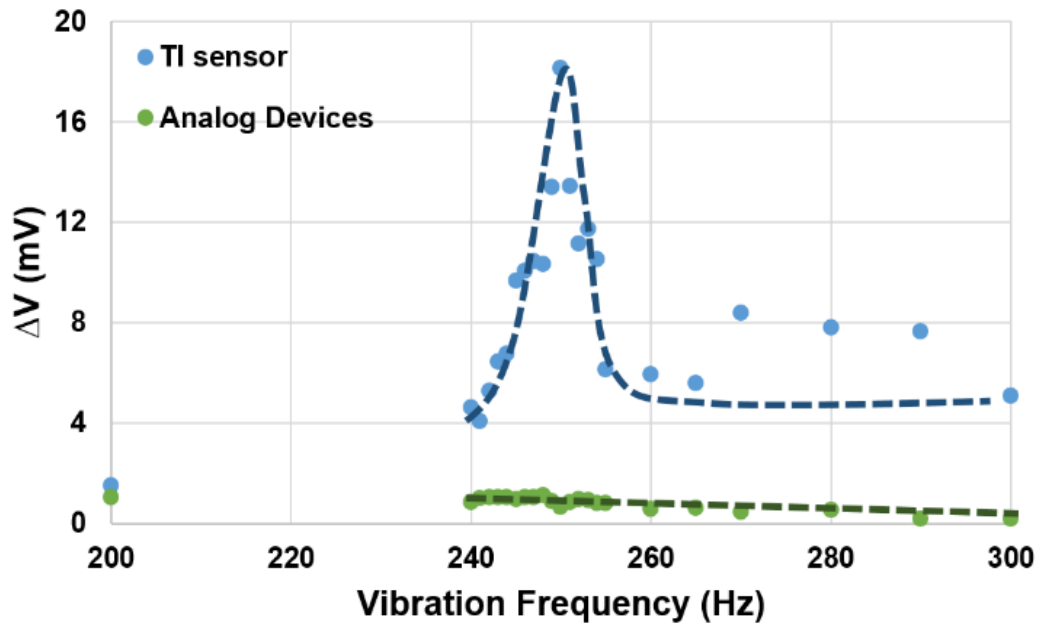


Figure 7.15. Frequency response of both sensors for 1g of vibration amplitude in the 200-300Hz frequency range.

Although a sensitivity of $\sim 18\text{mV/g}$ was obtained at the resonance frequency of the device, a sensitivity of only $\sim 4\text{-}6\text{ mV/g}$ was obtained past the resonance frequency up to 800Hz. To further

increase the bandwidth of the device and improve the sensitivity of the device, three different CMOS chips with different thickness of chip and mass combinations were used. Both static and frequency tests were once again performed for the sensor. ADS1232 was no longer used for the static tests as the sensitivity at 0Hz was significantly enhanced due to the much larger mass and the thinner CMOS chip. Figure 7.16 shows the 320mg added mass to the thinned down 60 μm CMOS chip. Figure 7.17 (a), 7.17 (b) and 7.17 (c) illustrates the static and the vibration response for the three different sensors for different bias voltages given to the device. As expected, the sensor with the thinnest chip and the largest mass provides the highest sensitivity and although the sensitivity gradually decreases as the resonance frequency is increased, the sensitivity is sufficient to measure 1mg of vibrations in its respective bandwidth of operation. Table 7.1 summarizes the different CMOS chips used in this work along with their resonance frequencies, sensitivities and bandwidths.

Although the preliminary results show a highly sensitive CMOS compatible vibration sensor, the bandwidth of such devices was limited to $\sim 50\text{-}100\text{Hz}$. Magnetic and Capacitive modulation techniques have been explored to increase the bandwidth of such sensors which have been discussed Section 7.7. Another potential solution that has been explored for a wider bandwidth of operation is to have an array of cantilevers operating at frequencies within a vicinity of each other. This has been discussed in Section 7.8.

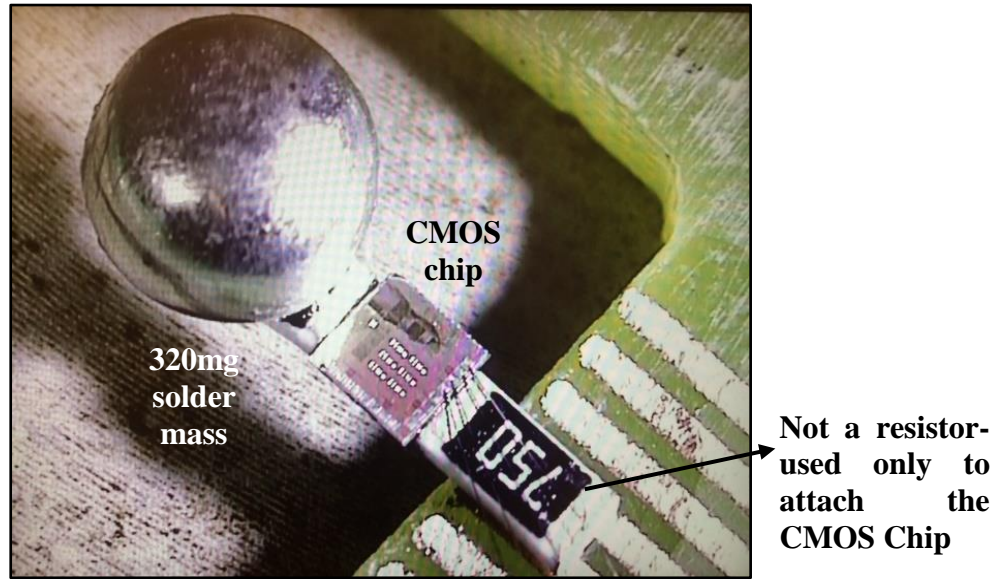


Figure 7.16. Experimental setup for the suspended thinned down CMOS chip.

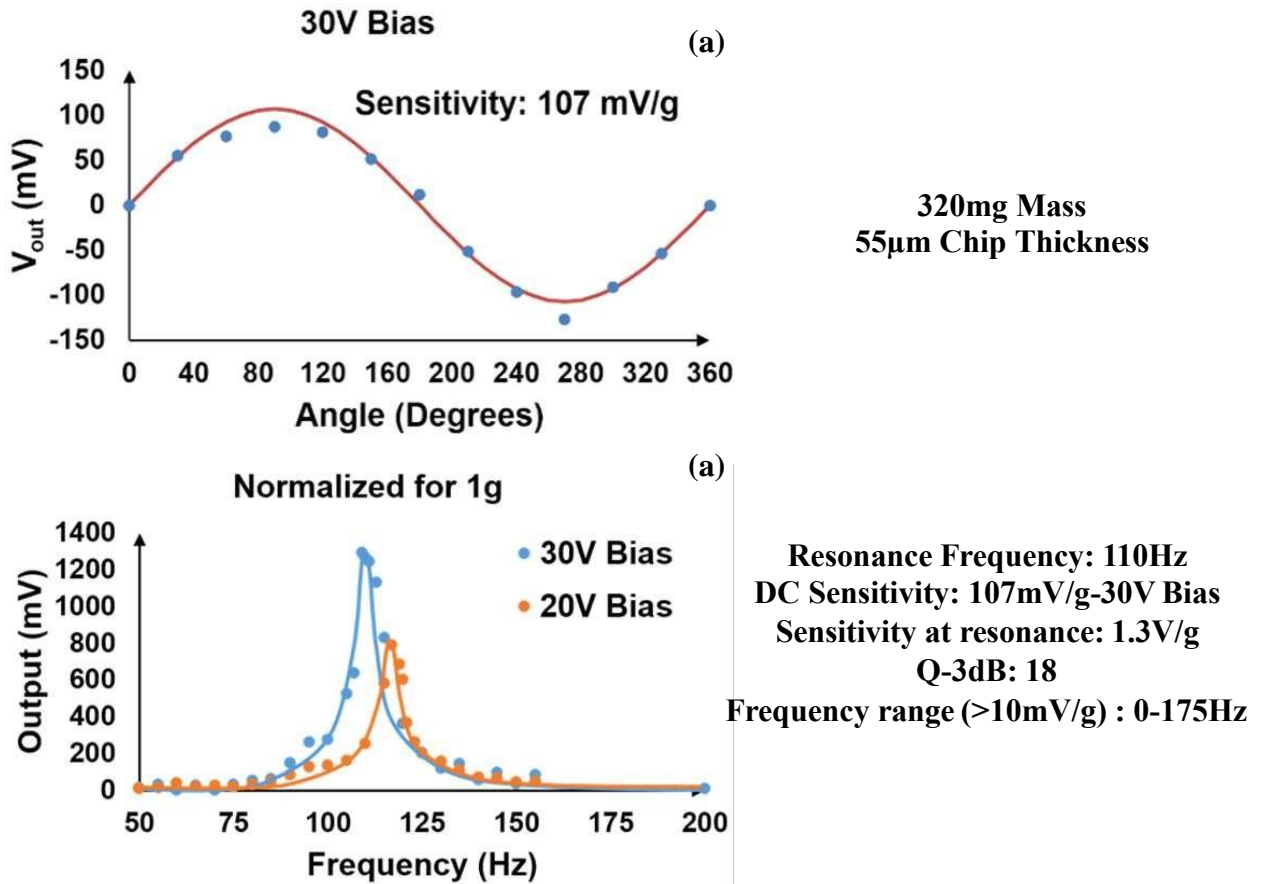
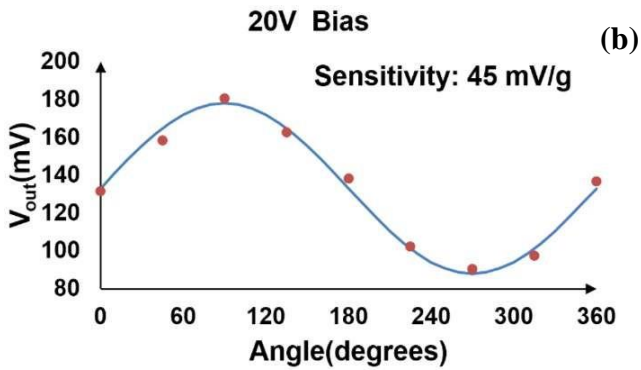
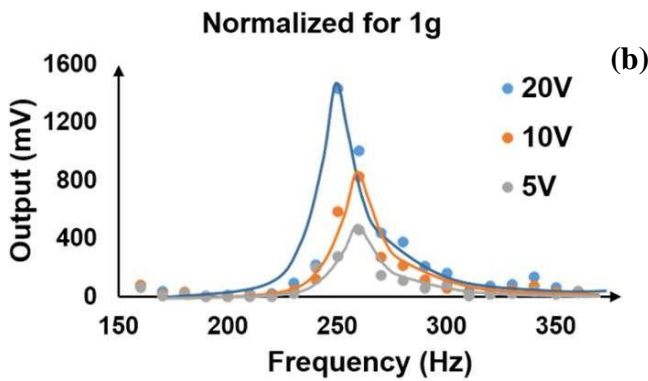


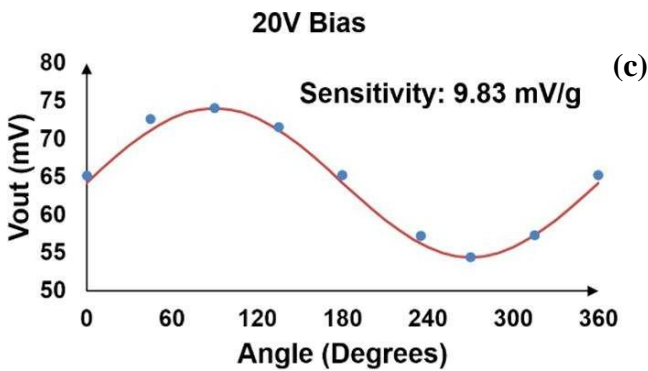
Figure 7.17.(a). Static and Frequency response for Sensor I for 1g of vibration.
(Continued below)



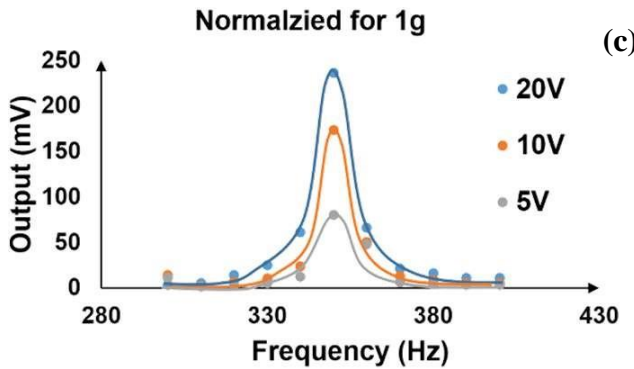
300mg Mass
70 μ m Chip Thickness



Resonance Frequency: 220Hz
DC Sensitivity: 45mV/g-20V Bias
Sensitivity at resonance: 1.4V/g
Q-3dB: 23
Frequency range (>10mV/g):140-360Hz



60mg Mass
70 μ m Chip Thickness



Resonance Frequency: 350Hz
DC Sensitivity: 10mV/g-20V Bias
Sensitivity at resonance: 0.24V/g
Q-3dB:87
Frequency range (>10mV/g): 315-400Hz

(Continued)

(b). Static and Frequency response for Sensor II for 1g of vibration.

(c). Static and Frequency response for Sensor III for 1g of vibration.

Table 7.1. CMOS-MEMS Vibration Sensors Characteristics and Bandwidth of Operation.

Parameter	Type I	Type II	Type III
Mass (mg) /Chip Thickness (μm)	300/55	300/70	60/70
Sensitivity DC (mV/V.g)	3.56	2.25	0.32
Sensitivity at resonance (mV/g)	2332	1439	236
Resonance Frequency (Hz)	109	255	347
Bandwidth for sensitivity >10mV/g (Hz)	0-175	140-360	315-400

7.7 CAPACITIVE AND MAGNETIC MODULATION FOR EXTENDED BANDWIDTH

To achieve larger operating bandwidths, magnetic and capacitive techniques were implemented to modulate the resonance frequency of the sensor. Solder masses were replaced by magnetic nickel masses of the same weight to retain the same resonance frequency. By applying a magnetic field between 0mT-37mT to the nickel mass, the resonance frequency of the sensor is modulated by ~20%. Figure 7.18 illustrates the change in the resonance frequency for the Type I sensor for different magnetic fields applied to the nickel mass. The major challenge in working with magnetic materials is hysteresis, due to which the response time for such sensors is limited. To overcome this issue, a novel capacitive mechanism was also explored. A piece of doped conductive silicon was added at the back of the CMOS chip with a thin piece of paper (~50 μm) in between that acted as the dielectric material. On applying 120V to the doped silicon chip and

grounding the CMOS sensor, the electrostatic force acting on the CMOS chip modulates the resonance frequency by $\sim 3.7\%$ as shown in Figure 7.18. Although the change in frequency is not as much as due to magnetic modulation, by using a thinner dielectric material/gap and applying larger capacitive voltages, the operating bandwidths of such sensors could be extended further.

7.8 DESIGN REFINEMENTS FOR EXTENDED OPERATION BANDWIDTH

The next CMOS chip tape-out was designed taking into consideration the preliminary results to improve stress/strain resolution and the sensing bandwidth. Figure 7.19 shows the microscopic view of a $7\text{mm} \times 4\text{mm}$ chip consisting of different vibration sensors. Side A consists of six different vibration sensors which work on a similar principle as reported Section 7.6 (with n-well piezoresistors in the Wheatstone bridge varying from 1k-ohm to 100k-ohm). Side B consists

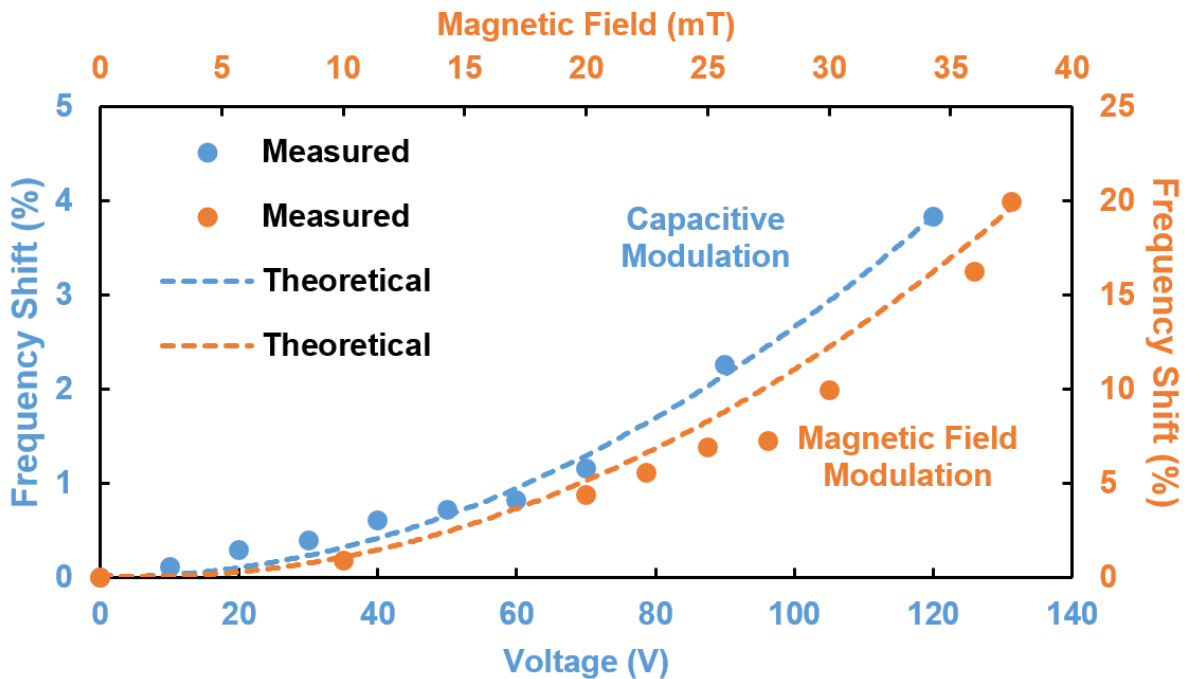


Figure 7.18. Shift in resonance frequency due to magnetic and capacitive modulation for Type I sensor.

of an identical array of such devices as on side A along with the addition of vias around the piezoresistors. The vias will be etched all the way through (using Aluminum etchant and Hydrogen Peroxide successively) to reach the silicon layer underneath. The silicon layer would be then etched anisotropically to create trenches around the piezoresistors. The advantage of such a design is to boost the stress acting on the piezoresistors as shown in Figure 7.20.

Vias of different lengths have been added at the center of the chip to create cantilevers of different lengths (and thus different resonant frequencies) to utilize the chip as a vibration spectrometer. Five different piezoresistors have been added to each of the cantilevers at their respective maximum stress locations. Vibrations close to/at the resonance frequency of the cantilever will actuate the cantilever which can be easily detected by a network analyzer. Figure 7.19 shows an example of such a sensor with vibrations being covered in the 2kHz-10kHz range.

7.9 POST PROCESS FABRICATION

For suspending the cantilever arrays, the center of the CMOS chip where the cantilevers are located was first thinned down to 54 μ m from the backside (DRIE) using Kapton tape as a mask (Figure 7.22 (b)). Large vias strategically placed in the CMOS layout around the cantilevers were then etched by dipping the chips successively in Aluminum etchant and Hydrogen Peroxide (Tungsten etchant) followed by Inductively Coupled Plasma (ICP) to remove the field oxide (~500nm) as shown in Figure 7.22 (c). The thick CMOS passivation layer (~2 μ m) protects the rest of the chip from the acids and the plasma during etch steps. The remaining silicon was then etched via DRIE from the top to suspend the cantilevers before removing the passivation oxide (via ICP) to expose the metal wire-bond pads (Figure 7.22(d)). Figure 7.23 shows the SEM view of the fabricated cantilever arrays.

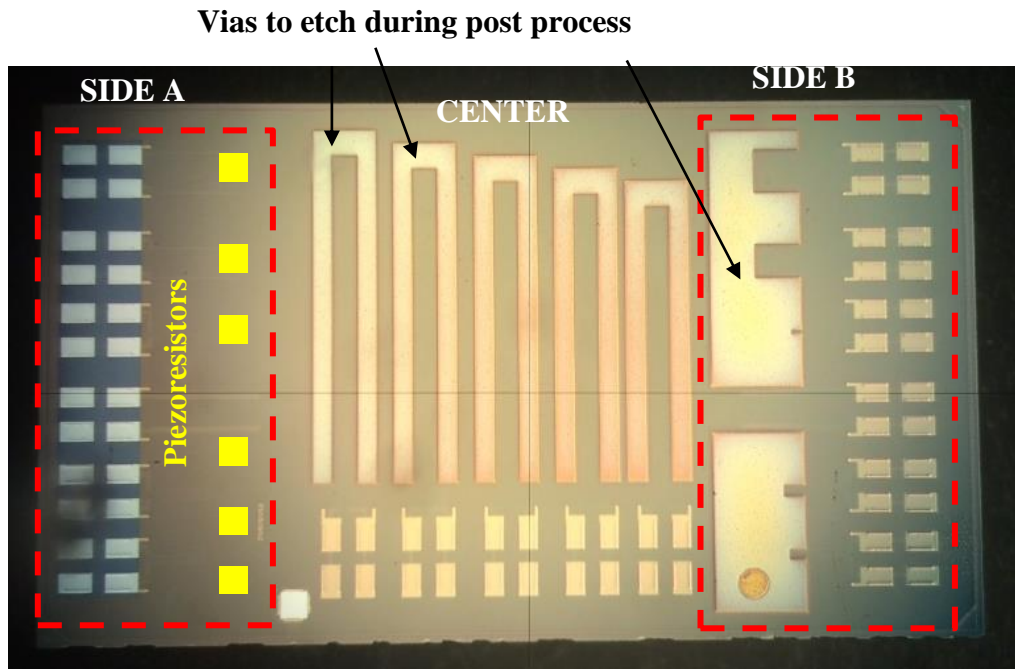


Figure 7.19. Optical image of the TI fabricated 7mm×4mm chip.

Side A: Six sensors each having piezoresistors connected in a Wheatstone's bridge fashion having resistors varying from 1k-ohm to 100-kohm.

Side B: Identical to Side A along with the addition of vias to increase the effect of stress due to vibrations acting on the piezoresistors.

Center: Vibration Spectrometer- five cantilevers with different resonance modes covering a wide range of frequency.

Stress acting on design two shows a 2.5X increase in stress at the piezoresistor location due to the addition of two 100µm×500µm trenches.

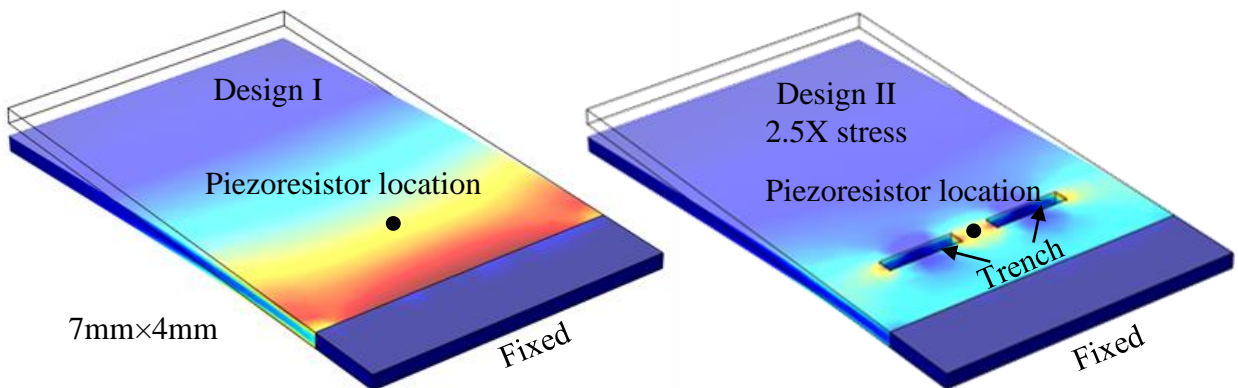


Figure 7.20. COMSOL Simulation showing an increase in stress on the piezoresistor on introductions of trenches around the piezoresistor.

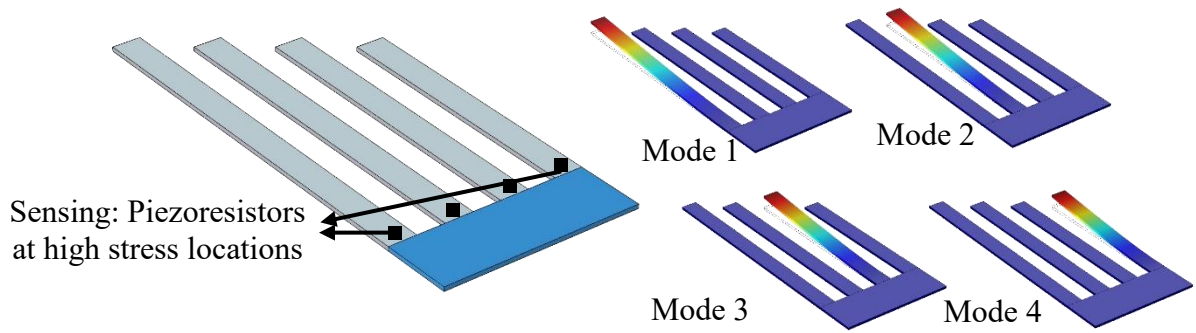


Figure 7.21. Eigenfrequency and mode shapes for 4 integrated cantilevers, each covering a small portion of the targeted frequency spectrum.

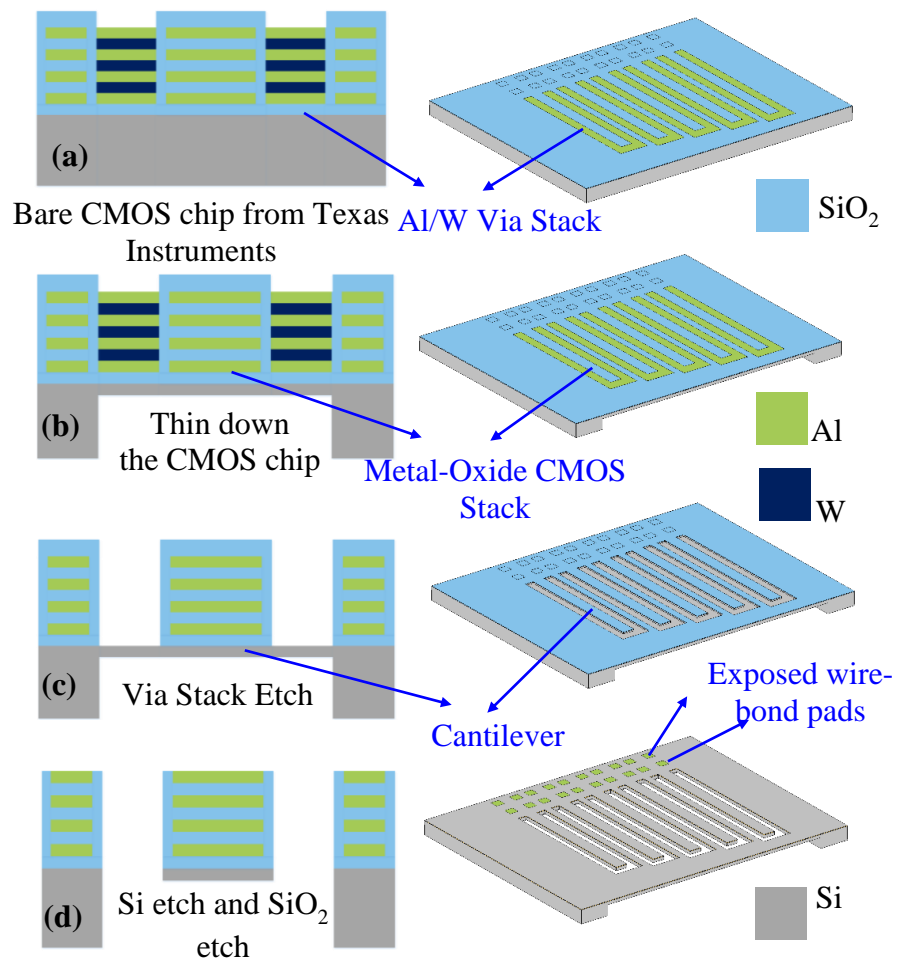


Figure 7.22. Post CMOS micro-machining steps for the higher frequency cantilever arrays.

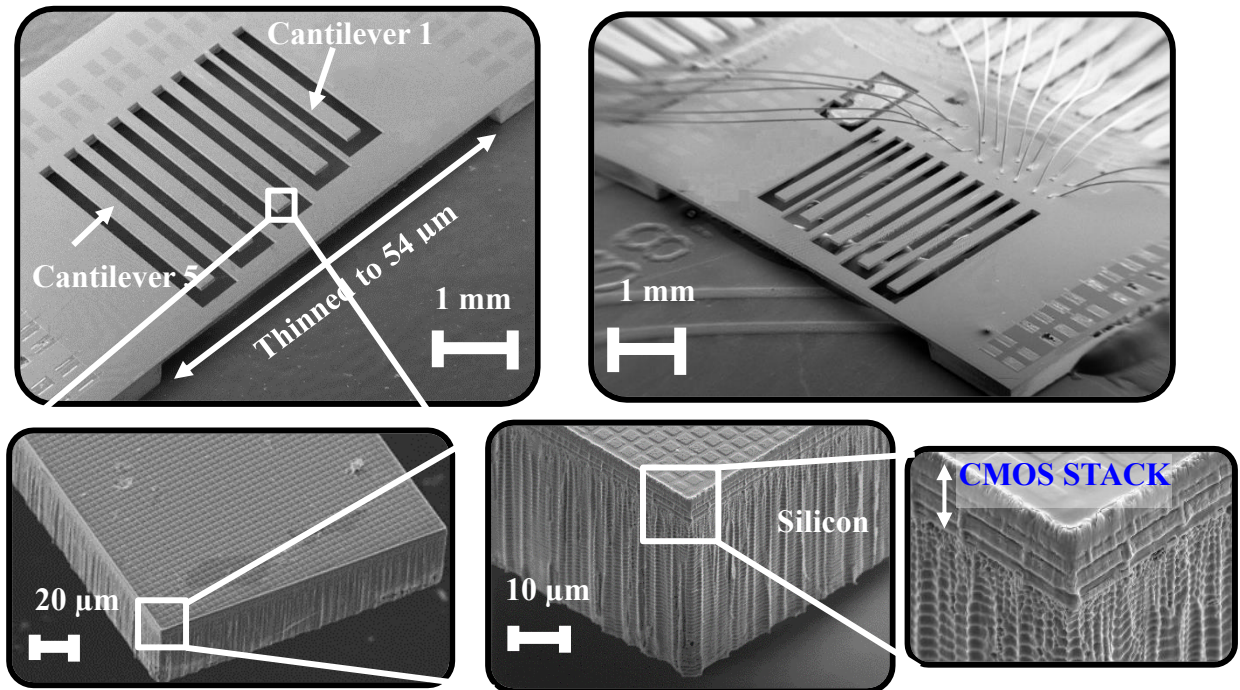


Figure 7.23. SEM view of the post processed higher frequency chip showing the integrated cantilever array.

7.10 MEASUREMENT RESULTS

Static and responses due to vibration were recorded once again similar to the previous sensors as explained in Section 7.6. Although the cantilever arrays are meant to be operated at higher frequencies, DC sensitivities can provide an insight into the behavior of the operation of such sensors at DC. To measure the DC sensitivity, a point load was swept along the length of the cantilever while measuring the changes in the output voltage across the piezoresistor, designed in a Wheatstone's bridge fashion. Figure 7.24 shows the changes in output voltage for different forces applied to the cantilever. The DC sensitivity for the longest cantilever ($\sim 2000\mu\text{m}$) is measured to be $7.6\mu\text{V/V.g}$.

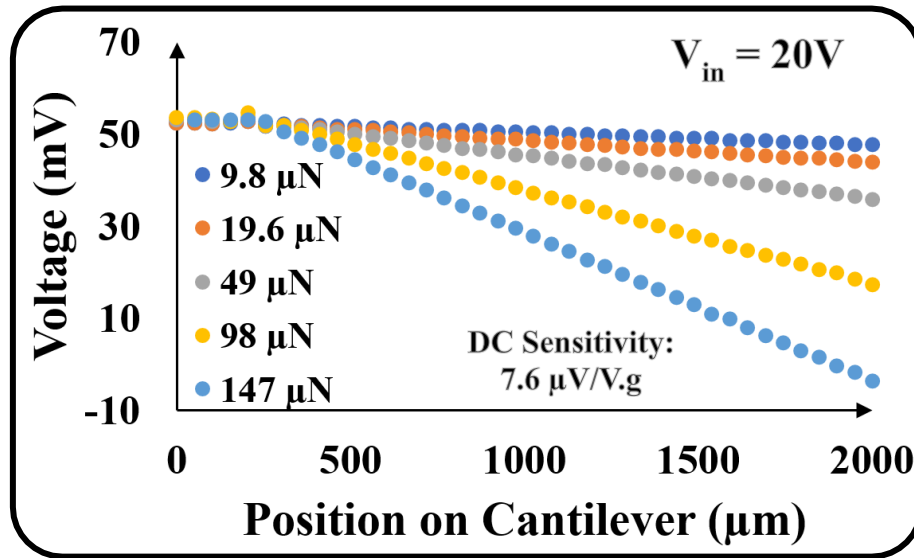


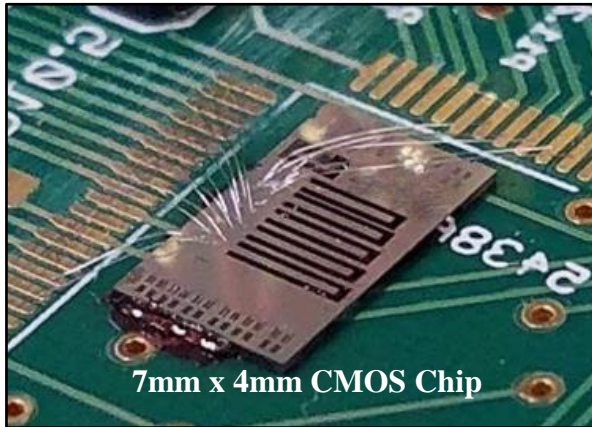
Figure 7.24. Output voltage vs position on cantilever for different static forces applied to Cantilever 5.

To measure the effect of vibrations on the CMOS chip, a speaker/sub-woofer was used to create sinusoidal vibrations at different frequencies using a network analyzer. The frequency spectrum for the vibration spectrometer was swept and the vibration response for all five cantilevers was recorded as shown in Figure 7.25. A maximum sensitivity of $\sim 5.3 \text{ mV/V.g}$ was achieved for the longest cantilever with its resonance frequency at $\sim 7.2 \text{ kHz}$.

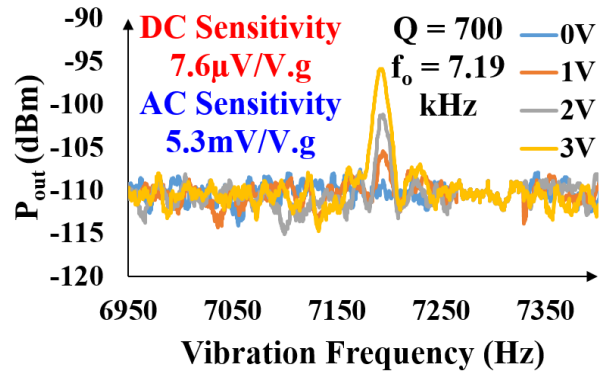
Table 7.2 summarizes the sensitivities (at DC and AC), the measured quality factors and the bandwidth for the five cantilevers.

7.11 SUMMARY

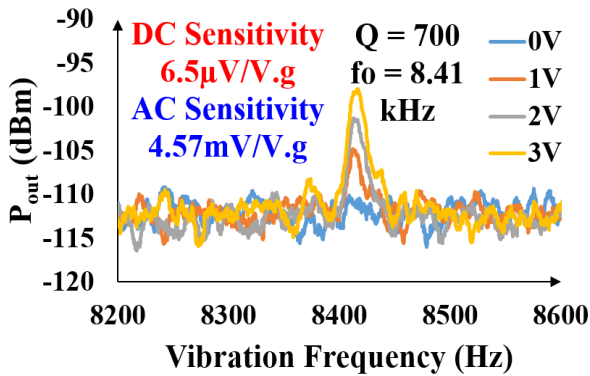
Two different configurations as shown in Section 7.6 and Section 7.8 can be utilized to cover the lower and higher end of the targeted spectrum. The lower frequency configuration utilizes the entire CMOS chip as a cantilever with on-chip piezoresistive strain gauges. A high-density mass is attached to the free end of the chips to lower the flexural resonance frequency ($\leq 500 \text{ Hz}$) and achieve sub-mg resolution (Figure 7.26(a)). The higher frequency configuration



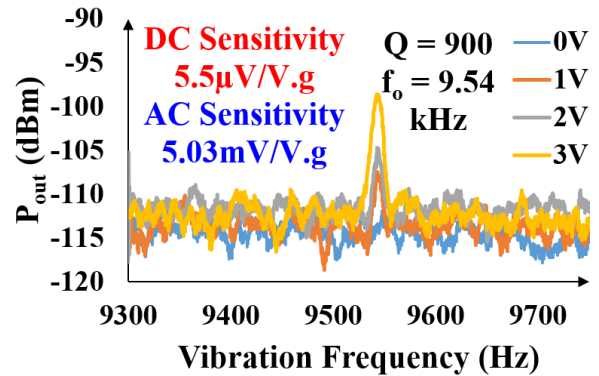
Cantilever 5



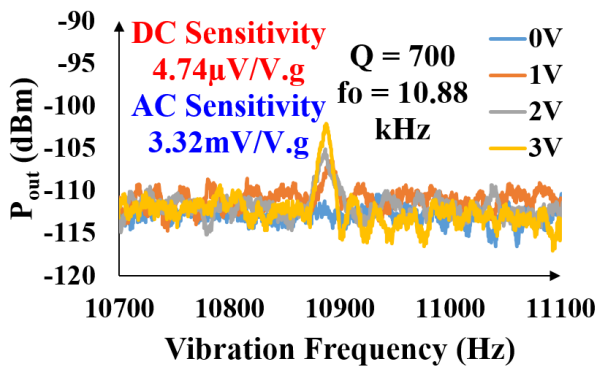
Cantilever 4



Cantilever 3



Cantilever 2



Cantilever 1

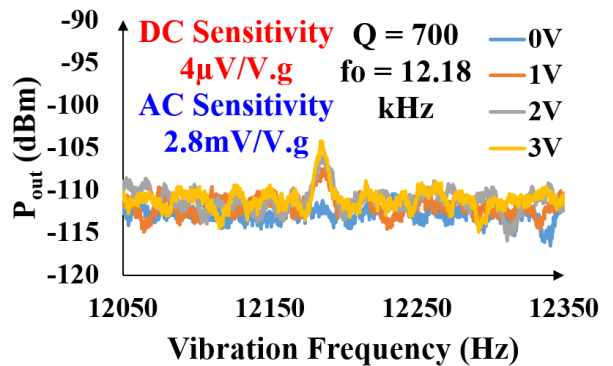
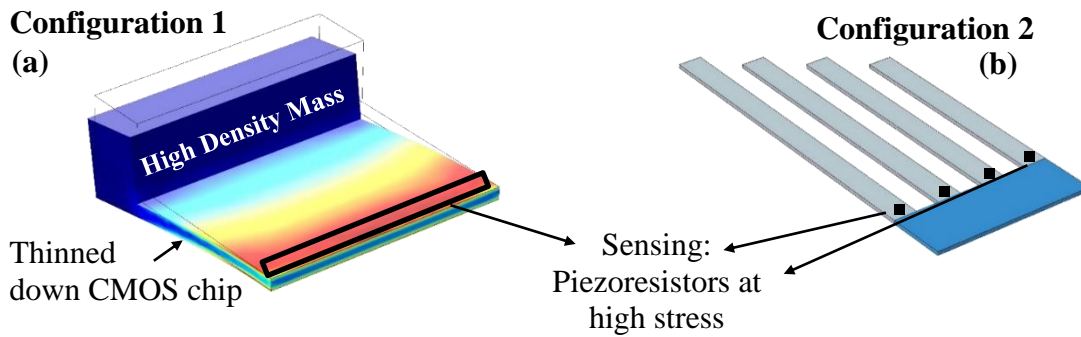


Figure 7.25. Image of the post processed and wire-bonded CMOS cantilevers (high frequency design) along with their response to vibrations at different frequencies. Each cantilever detects and measures the amplitude of vibrations at its resonance frequency where the vibration amplitude is amplified by the cantilever Q-factor.

Table 7.2. Sensitivity, Q-Factor and bandwidth of operation for the five cantilevers.

Cantilever	5	4	3	2	1
Frequency (kHz)	7.19	8.41	9.54	10.88	12.18
Sensitivity at DC ($\mu\text{V}/\text{V.g}$)	7.6	6.5	5.5	4.74	4
Sensitivity at AC ($\text{mV}/\text{V.g}$)	5.3	4.57	5.03	3.32	2.8
Q	700	700	900	700	700
Bandwidth (Hz)	10.2	10.6	10.6	15.5	17.4

utilizes arrays of integrated cantilevers within individual CMOS chips. Each cantilever detects and measures amplitude of vibrations at the vicinity of its resonance frequency (where the vibration amplitude is amplified by the cantilever Q-factor) (Figure 7.26 (b)). Piezoresistors (CMOS n-well resistors) on each cantilever are configured as a Wheatstone bridge, and located at the cantilever anchoring points where the vibrations cause maximum stress. The measured DC and AC sensitivities for the different cantilevers, in combination, makes it possible to sense very low amplitudes of vibrations over a large bandwidth by using a larger number of cantilevers (estimated 5 chips for covering DC-500Hz and 15 chips with 40 cantilevers each for covering 500Hz-10kHz) as shown in Figure 26(c).



Configuration 1: Utilizing the entire CMOS chip as the mechanical structure. High Density Mass added to **Lower Frequency (0-500Hz)**.

Configuration 2: Multiple post-processed CMOS chips with ‘n’ cantilevers each, covering **500Hz-10kHz** which sense frequency via resonance behavior- **no added mass**.

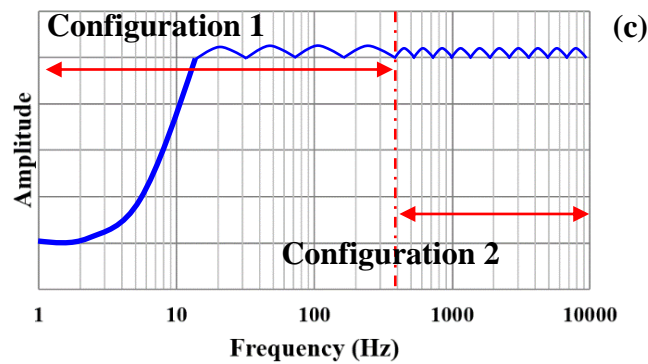


Figure 7.26.(a). Stress profile for the low frequency CMOS chip using Finite Element Static force analysis.
 (b). Eigenfrequency and mode shapes for 4 integrated cantilevers, each covering a small portion of the targeted frequency spectrum.
 (c). Overall frequency response for the combined configurations.

CHAPTER 8

CONCLUSIONS AND FUTURE WORK

8.1 CONTRIBUTIONS

The following is a list of contributions that have been achieved in this work.

- A tunable MEMS tunneling accelerometer based on the field emission principle was demonstrated. The tunneling gap was reduced to 170nm from the initial value of 1.5 μm by a simple mask-less gold deposition process with sidewall coverage. Parallel plate electrostatic electrode array embedded in the design was used to further reduce the tunneling gap size allowing tuning of the acceleration sensitivity over a wide range. The preliminary results laid in the pathway for self-computing switched coupled accelerometers.
- It was demonstrated that the concept of contact-based acceleration switches can be enhanced to perform higher resolution quantitative acceleration measurements. A tunable digitally operated MEMS accelerometer with a 2-bit resolution was successfully demonstrated with the help of a micro-controller. The same device principle can be utilized to implement 6-bit, 8-bit or even higher resolution digital accelerometers. Elimination of the need for the analog front-end and analog signal conditioning can lead to significant power savings and a leap forward towards ultralow power MEMS inertial sensors.
- The concept of multi-bit contact-based linear acceleration switches was successfully applied to rotational accelerometers which can be enhanced further to perform higher resolution quantitative acceleration measurements. A tunable digitally operated MEMS rotational accelerometer with a 3-bit resolution was successfully demonstrated.

- The concept of utilizing electrostatically coupled acceleration switches as ultra-low power digital MEMS accelerometer was demonstrated. A coupled switch accelerometer consisting of two electrostatically tunable acceleration switches was fabricated using a 2-mask fabrication process and successfully tested as a binary output 2-bit digital accelerometer without utilizing a micro-controller.
- Internal self-amplification of a micro-scale resonant Lorentz Force magnetometer with piezoresistive readout was demonstrated. The sensitivity of the device made up of n-type single-crystal silicon was improved by $\sim 2400X$. Close to $\sim 1620X$ improvement in the magnetometer sensitivity figure of merit was validated. It is expected that by thinning down the piezoresistive amplifying beam, much higher sensitivities can be obtained, potentially allowing compact low power sensor arrays for biomedical applications.
- A novel approach utilizing a high gain leverage mechanism and a low stiffness dual plate thermal piezoresistive resonator was successfully demonstrated for a frequency modulated magnetometer. Three different designs for the piezoresistive beams were explored and sensitivity was enhanced by $\sim 950X$ simply by optimizing the design of the piezoresistive beam. The sensitivity of the device was further improved by $\sim 55X$ due to the leverage mechanism boosting the sensitivity to $\sim 7200\text{ppm/mA/T}$ for the best-case design. It is expected that by optimizing the design to lower the stiffness of the resonator further and by increasing the force amplification factor by introducing a second stage of the leverage mechanism, much higher sensitivities can be potentially achieved.
- Implementation and characterization of building blocks of a low-power miniaturized vibration spectrum analyzer was demonstrated. To cover the entire targeted frequency

range (0-10kHz), two different device configurations, both utilizing piezoresistive strain gauges on microscale cantilevers, have been fabricated using a standard CMOS process with minimal mask-less post-CMOS micro-machining. Sensitivities as high as 9.73mV/g (at DC for 1mW of power consumed) and 14.5mV/g (at 7.2kHz for 1mW of power consumed) have been obtained for the lower and higher frequency configurations with a minimum resolution of 1.02mg and 0.2mg (for 1mW power consumption) respectively. The measured DC and AC sensitivities for the different cantilevers, in combination, makes it possible to sense very low amplitudes of vibrations over a large bandwidth by using a larger number of cantilevers (estimated 5 chips for covering DC-500Hz and 15 chips with 40 cantilevers each for covering 500Hz-10kHz).

8.2 FUTURE DIRECTION

- The concept of acceleration switches can be further enhanced to perform higher resolution quantitative acceleration measurements. The same principle can be utilized to implement 6-bit, 8-bit or even higher resolution digital accelerometers.
- The output of the rotational accelerometers should be integrated twice to provide angular position information (to be used as gyroscopes). Conventional gyroscopes require only one step of integration. Two such steps could lead to extra errors which can be fixed via signal processing and resetting techniques to reach acceptable accuracy for such sensors.
- Higher bits of resolution can be implemented for the self-computing coupled switch accelerometers as well once fabrication challenges associated with such large array of mass spring combinations have been resolved.

- Lorentz force MEMS resonant magnetometers with internal self-amplification: By thinning down the piezoresistor beam that can facilitate the self-amplification process as well as utilizing more compliant structures, much higher sensitivities can be obtained. The presented technique can also be applied to other sensor systems such as gyroscopes and accelerometers to boost their sensitivities.
- Frequency Modulated Lorentz force MEMS Magnetometers: Another step of leverage mechanism could be introduced to amplify the stress acting on the beam further and achieve much larger sensitivities. Further design optimization on the present structure could also lead to better stresses and higher sensitivities.
- Low power CMOS MEMS vibration sensors: The building blocks for a miniature vibration spectrum analyzer could be utilized to show a highly sensitive, wider-band vibration analyzer by designing and implementing a more practical version of the array of cantilevers demonstrated. Signal processing should also be incorporated to estimate the total power consumption of the entire system.
- CMOS-MEMS sensors created via post processing CMOS chips, as presented in this dissertation, could be explored to fabricate resonant structures which could in turn be used as vibration sensors. CMOS-MEMS sensors could potentially be used in variety of other applications as well such magnetometers, particle sensors and accelerometers.

REFERENCES

- [1] Olav Solgaard, Asif A. Godil, Roger T. Howe, Luke P. Lee, Yves-Alain Peter, and Hans Zappe, "Optical MEMS: From Micromirrors to Complex Systems", *Journal of Microelectromechanical Systems*, Vol 23, No3, pp 517-538, June 2014.
- [2] Hu, F., Tang, Y., & Qian, Y. (2012), "Design of a MEMS micromirror actuated by electrostatic repulsive force", *Optik-International Journal for Light and Electron Optics*, 123(5), pp 387-390.
- [3] Xu, R., Zhou, S., & Li, W. J. (2012) "MEMS accelerometer based nonspecific-user hand gesture recognition" *IEEE sensors journal*, 12(5), pp 1166-1173.
- [4] Fei, J., & Zhou, J. (2012) "Robust adaptive control of MEMS triaxial gyroscope using fuzzy compensator", *IEEE Transactions on Systems, Man, and Cybernetics, Part B (Cybernetics)*, 42(6), pp 1599-1607.
- [5] Zhuang, Y., Chang, H. W., & El-Sheimy, N. (2013) "A MEMS multi-sensors system for pedestrian navigation", In *China satellite navigation conference (CSNC) 2013 proceedings*, pp 651-660, Springer, Berlin, Heidelberg.
- [6] Kottapalli, A. G., Asadnia, M., Miao, J. M., Barbastathis, G., & Triantafyllou, M. S. (2012) "A flexible liquid crystal polymer MEMS pressure sensor array for fish-like underwater sensing", *Smart Materials and Structures*, 21(11), 115030.
- [7] Kim, B. H., Kim, S. I., Lee, J. C., Shin, S. J., & Kim, S. J. (2012), "Dynamic characteristics of a piezoelectric driven inkjet printhead fabricated using MEMS technology", *Sensors and Actuators A: Physical*, 173(1), pp 244-253.
- [8] Sue, Chung-Yang, and Nan-Chyuan Tsai. "Human powered MEMS-based energy harvest devices" *Applied Energy* 93 (2012): pp 390-403.
- [9] Sebastian, Abu, and Angeliki Pantazi. "Nanopositioning with multiple sensors: a case study in data storage." *IEEE transactions on control systems technology* 20, no. 2 (2012): pp 382-394.
- [10] Tsai, Ming-Han, Yu-Chia Liu, and Weileun Fang. "A three-axis CMOS-MEMS accelerometer structure with vertically integrated fully differential sensing electrodes." *Journal of Microelectromechanical Systems* 21, no. 6 (2012): 1329-1337.
- [11] Patel, Shyamal, Hyung Park, Paolo Bonato, Leighton Chan, and Mary Rodgers. "A review of wearable sensors and systems with application in rehabilitation." *Journal of neuroengineering and rehabilitation* 9, no. 1 (2012): 21.

- [12] Wang, Yu-Lin, Sheng-Fu Liang, Fu-Zen Shaw, Alvin WY Su, Yin-Lin Chen, and Ssu-Yen Wu. "Use of accelerometers to detect motor states in a seizure of rats with temporal lobe epilepsy." In Biomedical Circuits and Systems Conference (BioCAS), 2012 IEEE, pp 372-375. IEEE, 2012.
- [13] Anindya Lal Roy, Tarun Kanti Bhattacharyya, "Design, Fabrication and characterization of high performance SOI MEMS piezoresistive accelerometers", *Microsystem Technology*, pp 55-63, 201.
- [14] T Kobayashi, H Okada, T Masuda, R Maeda, T Itoh, "A Digital output accelerometer using MEMS-based piezoelectric accelerometers and arrayed CMOS inverters with satellite capacitors", *Smart Materials and Structures*, 065017, 2011.
- [15] Xiaofeng Zhou, Lufeng Che, Shenglin Liang, Youling Lin, Xiaolin Li, Yuelin Wang, "Design and fabrication of a MEMS capacitive accelerometer with fully symmetrical double-sided H-shaped beam structure", *Nicroelectronic Engineering*, pp 51-57, 2015.
- [16] V. Kumar, X. Guo, S. Pourkamali, "Single-Mask Field Emission based tunable MEMS Tunneling Accelerometer", pp1171-1174, *Proceedings of the 15th IEEE International Conference on Nanotechnology*, 2015.
- [17] Lee D, "Wireless and powerless sensing node system developed for monitoring motors" *Sensors* pp 5005-5022, 2008.
- [18] Zwahlen, P., Y. Dong, A. M. Nguyen, F. Rudolf, J. M. Stauffer, P. Ullah, and V. Ragot. "Breakthrough in high performance inertial navigation grade Sigma-Delta MEMS accelerometer", In *Position Location and Navigation Symposium (PLANS)*, 2012 IEEE/ION, pp 15-19. IEEE, 2012.
- [19] Tseng, Sheng-Hsiang, Michael SC Lu, Po-Chang Wu, Yu-Chen Teng, Hann-Huei Tsai, and Ying-Zong Juang. "Implementation of a monolithic capacitive accelerometer in a wafer-level 0.18 μm CMOS MEMS process." *Journal of Micromechanics and Microengineering* 22, no. 5 (2012): 055010.
- [20] Jeong, Y., D. E. Serrano, V. Keesara, W. K. Sung, and F. Ayazi. "Wafer-level vacuum-packaged triaxial accelerometer with nano airgaps." In *Micro Electro Mechanical Systems (MEMS)*, 2013 IEEE 26th International Conference on, pp 33-36. IEEE, 2013.
- [21] V. Kumar, X. Guo, S. Pourkamali, "A Tunable Digitally Operated MEMS Accelerometer", 10.1109/ICSENS.2015.7370304, pp 1-4, *IEEE Sensors* 2015.
- [22] V. Kumar, X. Guo, R. Jafari, S. Pourkamali, "Ultra-Low Power Self-Computing Binary Output Digital MEMS Accelerometer", pp 251-254, *IEEE MEMS* 2016.

- [23] D. Niarchos, "Magnetic MEMS: key issues and some applications," *Sensors & Actuators A, Phys.*, Vol 106, no. ½, pp 255-262, Sep 2003.
- [24] E. K. Ralph, "Comparison of a Proton and a Rubidium Magnetometer for Archaeological Prospecting," *Archaeometry*, vol. 7, no. 1, pp 20–27, Jun. 1964.
- [25] M. Li, V. T. Rouf, M. J. Thompson, and D. Horsley, "Three-Axis Lorentz-Force Magnetic Sensor for Electronic Compass Applications," *J. Microelectromechanical Syst.*, vol. 21, no. 4, pp 1002–1010, Aug 2012.
- [26] S. Levine, D. Silage, D. Henson, J. Y. Wang, J. Krieg, J. LaManca, and S. Levy, "Use of a triaxial magnetometer for respiratory measurements," *J. Appl. Physiol. Bethesda*, vol. 70, no. 5, pp 2311–2321, May 1991.
- [27] H. C. Séran and P. Fergeau, "An optimized low-frequency three-axis search coil magnetometer for space research," *Rev. Sci. Instrum.*, vol. 76, no. 4, p. 044502, Apr. 2005.
- [28] Bernieri, A. ; Univ. of Cassino, Cassino ; Ferrigno, L. ; Laracca, M. ; Tamburrino, A., "Improving GMR Magnetometer Sensor Uncertainty by Implementing an Automatic Procedure for Calibration and Adjustment", *IMTC*, 2007.
- [29] P. Ripka, "Advances in fluxgate sensors", *Sensors and Actuators*, vol 106, issue 1-3, 15 September 2003.
- [30] A. Pérez Galván, B. Plaster, J. Boissevain, R. Carr, B. W. Filippone, M. P. Mendenhall, R. Schmid, R. Alarcon, and S. Balascuta, "High uniformity magnetic coil for search of neutron electric dipole moment," *Nucl. Instrum. Methods Phys. Res. Sect. Accel. Spectrometers Detect. Assoc. Equip.*, vol. 660, no. 1, pp 147–153, Dec. 2011.
- [31] N. L. Adolphi, D. L. Huber, H. C. Bryant, T. C. Monson, D. L. Fegan, J. Lim, J. E. Trujillo, T. E. Tessier, D. M. Lovato, K. S. Butler, P. P. Provencio, H. J. Hathaway, S. A. Majetich, R. S. Larson, and E. R. Flynn, "Characterization of single-core magnetite nanoparticles for magnetic imaging by SQUID relaxometry," *Phys. Med. Biol.*, vol. 55, no. 19, pp. 5985, Oct. 2010.
- [32] D. Sheng, S. Li, N. Dural, M. V. Romalis, "Subfemtotesla Scalar Atomic Magnetometry using multipass cells", *Physical review letters* 110, 160802, April 2013.
- [33] F. Gueissaz and D. Pigué, "The MicroReed, an ultra-small passive MEMS magnetic proximity sensor designed for portable applications," in the 14th IEEE International Conference on Micro Electro Mechanical Systems, 2001. *MEMS 2001*, 2001, pp 269–273.
- [34] A. L. Herrera-May, L. A. Aguilera-Cortes, P. J. Garcia-Ramirez, and E. Manjarrez, "Resonant Magnetic Field Sensors Based on MEMS Technology," *Sensors*, vol. 9, no. 10, pp 7785–7813, Sep. 2009.

- [35] Y. Hui, T. Nan, N. X. Sun, and M. Rinaldi, “High Resolution Magnetometer Based on a High Frequency Magnetoelectric MEMSCMOS Oscillator,” *J. Microelectromechanical Syst.*, 2014.
- [36] S. Marauska, R. Jahns, H. Greve, E. Quandt, R. Knöchel, and B. Wagner, “MEMS magnetic field sensor based on magnetoelectric composites,” *J. Micromechanics Microengineering*, vol. 22, no. 6, pp 065024, Jun. 2012.
- [37] M. Thompson and D. Horsley, “Resonant MEMS magnetometer with capacitive read-out,” 2009 IEEE Sensors Conference, 2009, pp 992–995.
- [38] M. Li , Eldwin J. Ng , Vu A. Hong , C. Ahn , Yushi Yang , T. Kenny and D. Horsley, “Single structure 3-axis Lorentz Force Magnetometer with sub-30nT/ $\sqrt{\text{Hz}}$ resolution”, *IEEE MEMS 2014*, pp 80-83.
- [39] E. Mehdizadeh, V. Kumar, and S. Pourkamali, “Sensitivity Enhancement of Lorentz Force MEMS Resonant Magnetometers via Internal Thermal- Piezoresistive Amplification,” *IEEE Electron Device Lett.*, vol. 35, no. 2, pp 268–270, Feb. 2014.
- [40] E. Mehdizadeh, V. Kumar, and S. Pourkamali, “High Q Lorentz Force MEMS Magnetometer with Internal Self-Amplification,” *IEEE Sensors 2014*, pp 706–709, October 2014.
- [41] W. Zhang and J. E. Lee, “A horseshoe micromachined resonant magnetic field sensor with high quality factor,” *IEEE Electron Device Lett.*, vol. 34, no. 10, pp 1310–1312, Oct. 2013.
- [42] M. Thompson & D. Horsley, “Parametrically Amplified MEMS Magnetometer,” *IEEE Transducers*, pp 1194-1197, 2009.
- [43] J. Kyynarasinen, J. Saarilahti, H. Kattelus, A. Karkkainen, T. Meinander, A. Oja, P. Pekko, H. Seppa, M. Suhonen, H. Kusima, S. Ruotsalainen, M. Tilli, “A 3D micromechanical compass”, *Sensors and Actuators A* 142, pp 561-568, 2008.
- [44] G. Laghi, A. Longoni, P. Minotti, A. Tocchio, G. Langfelder, “100 μA , 320nT/rHz, 3Axis Lorentz force MEMS magnetometer”, *Transducers 2015* pp 803-806, June 2015.
- [45] V. Kumar, M. Mahdavi, X. Guo, E. Mehdizadeh and S. Pourkamali, “Ultra-Sensitive Lorentz Force MEMS Magnetometer with Pico-Tesla Limit of Detection”, pp 204-207, *IEEE MEMS*, 2015.
- [46] G. Langfelder, G. Laghi, P. Minotti, “Off resonance low-pressure operation of Lorentz Force MEMS magnetometers”, *IEEE Transactions on industrial electronics*, vol 61, no.12, pp 7124-7131, Dec 2012.

- [47] P. Minotti, S. Brenna, G. Laghi, A. Bonfanti, G. Langfelder, A. Lacaita, "A Sub-400nT/rtHz, 775 μ W, Multi-loop MEMS magnetometer with integrated Readout electronics", *JMEMS*, vol 24, no 6, pp 1938-1950, Dec 2015.
- [48] S. Sonmezoglu, D. Horsley, "Off-resonance operation of a MEMS Lorentz Force Magnetometer with improved thermal stability of the scale factor", *IEEE MEMS 2016*, pp 103-106.
- [49] V. Kumar, S. Pourkamali, "Lorentz Force MEMS Magnetometer with Frequency Modulated Output", *IEEE MEMS 2016*.
- [50] W. Zhang, J. Lee, "Frequency-based magnetic field sensing using Lorentz force axial strain modulation in a double-ended tuning fork", *Sensors and Actuators A211*, pp 145-152, 2011.
- [51] M. Li, S. Nitzan, D. Horsley, "Frequency-Modulated Lorentz Force Magnetometer with enhanced sensitivity via Mechanical Amplification", *IEEE EDL*, vol 36, no. 1, pp 62-64, Jan 2015.
- [52] M. Li, S. Sonmezoglu, D. Horsley, "Extended Bandwidth Lorentz Force Magnetometer based on Quadrature Frequency Modulation", *Journal of Microelectromechanical systems*, 2014.
- [53] Albarbar A (2012) *Vibration and noise of diesel engines*. Lap Lambert Academic, Saarbrücken. ISBN 978-3-659-11039-9 2.
- [54] Shi H-Y, Wang W-L, Kwok N-M, Chen S-Y (2012) Game theory for wireless sensor networks: a survey. *Sensors* 12(7):9055–9097 3.
- [55] Ibrahim G, Albarbar A, Abouhnik A, Shnibha R (2013) Adaptive filtering-based system for extracting gearbox condition feature from the measured vibrations. *Measurement* 46:2029–2034.
- [56] Albarbar A, Sinha J, Starr A (2009) Performance evaluation of MEMS accelerometers. *J Meas* 42(5):790–795.
- [57] Y. Chiu, V. Tseng, "A capacitive vibration-to-electricity energy converter with integrated mechanical switches", *Journal of Micromechanics and Microengineering*, 18, 1004004, 2008.
- [58] S. Saadon, O. Sidek, "A review of vibration-based MEMS piezoelectric energy harvesters", *Energy Conversion and Management* 52, pp 500-504, 2011.
- [59] Laine, Jerome, and Denis Mougnot. "Benefits of MEMS based seismic accelerometers for oil exploration." In *Solid-State Sensors, Actuators and Microsystems Conference, 2007. Transducers 2007. International*, pp 1473-1477. IEEE, 2007.

- [60] C. H. Liu, J. D. Grade, A. M. Barzilai, K. K. Reynolds, A. Partridge, J. J. K. Rockstad, and T. W. Kenney, "Characterization of a highly sensitive tunneling accelerometer," in *Transducers '97 Tech. Dig.*, 1997, pp 471–472, paper 2B3.07.
- [61] H. K. Rockalnd, T. W. Kenny, P. Kelley, and T. Gabrielson, "A microfabricated electron-tunneling accelerometer as a directional underwater acoustic sensor," in *Proc. Acoustic Particle Velocity Sensors: Design, Performance, and Applications*, 1996, pp 57–68.
- [62] Bernstein, Jonathan, Raanan Miller, William Kelley, and Paul Ward. "Low-noise MEMS vibration sensor for geophysical applications." *Journal of microelectromechanical systems* 8, no. 4 (1999): 433-438.
- [63] Ollier, Eric. "Optical MEMS devices based on moving waveguides." *IEEE Journal of selected topics in quantum electronics* 8, no. 1 (2002): 155-162.
- [64] Kon, Stanley, Kenn Oldham, and Roberto Horowitz. "Piezoresistive and piezoelectric MEMS strain sensors for vibration detection." In *Proc. SPIE*, vol. 6529, pp 65292V, 2007.
- [65] Wisitsoraat, A., V. Patthanasetakul, T. Lomas, and A. Tuantranont. "Low cost thin film based piezoresistive MEMS tactile sensor." *Sensors and Actuators A: Physical* 139, no. 1 (2007): 17-22.
- [66] R. Abdolvand, B.V. Amini, and F. Ayazi, "Sub-micro-gravity in-plane accelerometers with reduced capacitive gaps and extra seismic mass," *IEEE Journal of Microelectromechanical Systems*, Vol. 16, pp 1036- 1043, Oct. 2007.
- [67] L. J. Currano, et al "Latching ultra-low power MEMS shock sensors for acceleration monitoring," *Sensors and Actuators A*, 147 (2008), pp 490–497.
- [68] L. J. Currano, C. R. Becker, G. L. Smith, B. Isaacson, and C. J. Morris, "3-axis acceleration switch for traumatic brain injury early warning," in *Proc. MEMS 2012, Paris, France*, pp 484-487.
- [69] S. McNamara, Y. B. Gianchandani, "LIGA fabricated 19-element threshold accelerometer array," *Sensors and Actuators A*, 112 (2004), pp 175–183.
- [70] A. Selvakumar, N. Yazdi and K. Najafi, "A wide-range micromachined threshold accelerometer array and interface circuit," *J. Micromech. Microeng.*, 11 (2001), pp 118–125.
- [71] T Tonnesen, O Ludtke, J Noetzel, J binder, G Mader, "Simulation, design and fabrication of electroplated acceleration switches", *J. Micromech. Microeng.*, pp 237-239, April 1997.
- [72] Sven Michaelis, Hans Jorg Timme, Michael Wycisk, Josef Binder, "Additive electroplating technology as a post CMOS process for the production of MEMS acceleration-threshold switches for transport applications", *J. Micromech. Microeng.*, pp 120-123, Feb 2000.

- [73] Jeung Sang Go, Young Ho Cho, Byung Man Kwak, Kwanhum Park, “Snapping microswitches with adjustable acceleration threshold”, *Sensors and Actuators A*. 54, pp 579-583, 1996.
- [74] H. S Kim, Y. H Jang, Y. K Kim, J. M Kim, “MEMS acceleration switch capable of increasing threshold acceleration”, *Electronics Letters*, Vol 48, No 25, Dec 2012.
- [75] John G Simmons, “Generalized Formula for the electric Tunnel effect between similar electrodes separated by a thin insulating film”, *J. Applied Physics*, Vol 34, pp 1793-1803, 1963.
- [76] A. Rahafrooz, and S. Pourkamali, “Thermal piezoresistive energy pumps in micromechanical resonant structures,” *IEEE Trans. Electron Devices*, vol. 59, no. 12, pp 3587–3593, Dec. 2012.
- [77] A. Ramezany, M. Mahdavi, S. Pourkamali, “Nanoelectromechanical resonant narrow-band amplifiers”, *Microsystems and Nanoengineering 2*, Article Number 16004, March 2016.
- [78] M. Mahdavi, A. Ramezany, V. Kumar and S. Pourkamali, “SNR Improvement in Amplitude Modulated Resonant MEMS Sensors Via Thermal-Piezoresistive Internal Amplification”, pp 913-916, *IEEE MEMS 2015*.
- [79] A. Hajjam, A. Logan, S. Pourkamali, “Doping Induced Temperature Compensation of Thermally Actuated High-frequency Silicon Micromachined resonators”, *Journal of Microelectromechanical systems*, Vol 21, No3, pp 681-687, June 2012.
- [80] A. Rahafrooz, S. Pourkamali, “High-Frequency Thermally Actuated Electromechanical Resonators with Piezoresistive Readout”, *IEEE Transactions on Electron Devices*, vol 58, no. 4, pp 1205-1214, 2011.
- [81] Alireza Ramezany, Mohammad Mahdavi, Siavash Pourkamali, “Nanoelectromechanical resonant narrow-band amplifiers”, *Microsystems & Nanoengineering 2*, Article number: 16004 (2016).

BIOGRAPHICAL SKETCH

Varun Kumar was born in New Delhi, India. After finishing high school at Indian School Muscat, Oman in 2008, he pursued his undergraduate degree in Electrical Engineering from NIRMA University, Gujarat, India in 2008. Soon after the completion of his undergraduate degree (B.Tech) in 2012, Varun entered graduate school at The University of Texas at Dallas. He graduated with a master's degree in Electrical Engineering in 2014, and a PhD degree in Electrical Engineering from The University of Texas at Dallas, Dallas, TX, in 2018. His PhD work focused on exploring novel sensing mechanisms for various sensors including accelerometers, magnetometers and CMOS-MEMS vibration sensors. His current interests are in the areas of MEMS magnetometers and accelerometers, silicon micromachining technologies and integrated microsystems. Varun is a recipient of the Outstanding Student Paper Award at the IEEE MEMS 2015 conference.

CURRICULUM VITAE

Varun Kumar

800 West Campbell Road, RL 10, Richardson, TX 75080| v.kumar@utdallas.edu

EDUCATION

PhD in Electrical Engineering

May 2018

The University of Texas, Dallas, USA

Dissertation: Novel Sensing Approaches towards Ultimate MEMS sensors

The purpose of this research project is to explore novel techniques for achieving ultra-high sensitivities for MEMS magnetic sensors, accelerometers, and vibration sensors.

Key features of the research:

MEMS Magnetometers

- ✓ Achieve ultra-high sensitivities (in the pT-fT range) for Lorentz Force MEMS magnetometers to potentially replace SQUID's for bio-medical applications.
- ✓ Utilization of thermal-piezoresistive amplification mechanism which amplifies the stress and consequently the vibration amplitude acting on a n-type silicon piezoresistive beam.
- ✓ Explore frequency modulation of MEMS magnetometers to overcome the challenges present in Q-factor enhanced amplitude modulation which includes noise, temperature effects and bandwidth of operation.

MEMS Accelerometers

- ✓ Design, fabricate and characterize an ultra-low power consuming (sub nW) accelerometer by eliminating the need for an analog front end.
- ✓ Obtain a binary digital output with or without the use of a processor directly from the sensor.

CMOS Compatible MEMS Vibration Sensors

- ✓ Design and implement low-power chip scale vibration sensors that have ~1mg resolution over a wide frequency range of 0-20kHz by using an existing Texas Instruments process platform.
- ✓ Potentially compete with the commercially available bulky and expensive vibration spectrometers.

Relevant Coursework: Semiconductor processing Technology, Introduction to MEMS, Mechanical properties of materials, Electrical, Optical and Magnetic Materials.

Master's in Electrical Engineering

May 2014

The University of Texas, Dallas, USA

Thesis: Sensitivity Enhancement of Resonant MEMS Magnetometers using Internal Thermal-Piezoresistive Amplification

This thesis focuses on the sensitivity enhancement of magnetometers using the internal thermal piezoresistive Q-Amplification in resonators.

Key features:

- ✓ Presents an electromechanical model of the magnetometer along with its simulation in MATLAB. The results of the simulation are studied, and the parameter selection criteria are determined for an optimized design.
- ✓ Show improvement in sensitivity of the magnetometer solely due to the internal thermal-piezoresistive Q amplification mechanism.

B.Tech in Electrical Engineering

June 2012

NIRMA University, Ahmedabad, India

Final Year Project: PLC Based Numerical Relay for Induction Machine Protection

The machine voltages and currents were detected by the PLC and the tolerances were calculated as per the developed program. The relay tripped during any mal-operation to protect the machine.

WORK EXPERIENCE

Internship: Texas Instruments

June 2017-Aug 2017

Systems Engineer Intern

- Comprehensive testing and characterization of a new Graphene Hall Effect Sensor to compare its performance with existing silicon Hall sensors and III/V Hall sensors.
- Sensor performance compared in terms of Sensitivity, Linearity, Noise, Contact Resistance and Offset.
- Implementation of TI's patented Offset calibration technique in Graphene Hall Sensors.
- Potentially introduce a market for Graphene Hall Sensors that can eventually replace Silicon Hall sensors.
- Build routines and equipment for characterization and automation via MATLAB.

Internship: femtoScale Inc.

Aug 2016-Dec 2016

Product Engineer

- Comprehensive testing and characterization of the ultra-fine particulate (10nm-100nm) matter sensor system- currently, no commercially available sensor can measure "mass" of ultra-fine particles in real-time- only "count".
- Preparing technical reports and application notes for the prototype sensor.
- Designing a user-friendly 3D printed package for the prototype sensor system.

RESEARCH EXPERIENCE

The University of Texas at Dallas

Jan 2013-Jan 2018

Graduate student with Dr. Siavash Pourkamali

- Development of Ultra-low power digital accelerometers.
- Achieve ultra-high sensitivities for Lorentz force MEMS Magnetometers.
- Development of a highly sensitive, wide band CMOS compatible MEMS vibration sensor-collaboration with Texas Instruments.
- Exploring novel nanolithography techniques, testing and characterization of various mass sensors and thermal resonators.

Texas Instruments

Aug 2017-Dec 2017

Visiting Student Researcher

- Development of signal conditioning circuit for the Hall-effect magnetic sensor using board-level design.
- Assist tool design engineers in the development of CMOS sensors using Cadence.

SKILLS AND TECHNIQUES

- **Cleanroom experience:** photolithography, metal deposition, plasma etch tools and SEM.
- **Software Knowledge:** COMSOL, Solid Works, ANSYS, Cadence, Allen Bradley PLC Programming.
- Automation for test equipment via MATLAB, C, C++.
- Perform device and product characterization.
- Highly knowledgeable about most **fabrication techniques** used in the semiconductor industry.

HONORS AND AWARDS

- Awarded **Best Student Paper** of the conference at IEEE MEMS, 2015, held at Portugal in **Jan. 2015**.
- Awarded **Best Poster** at TxACE Annual Review, held at The University of Texas at Dallas in **Oct. 2015**.
- Awarded **Best Poster** at the SRC Annual Review, held at The University of Texas at Dallas in **Oct. 2017**.

PUBLICATIONS

Journal Articles

1. **V. Kumar**, S. Sebdani, S. Pourkamali, "Sensitivity Enhancement of a Lorentz Force MEMS Magnetometer with Frequency Modulated Output", Journal of Microelectromechanical Systems, Vol 26, Issue 4, pp 870-878, Aug 2017.
2. E. Mehdizadeh, **V. Kumar**, J. Wilson, S. Pourkamali, "Inertial Impaction on MEMS Balance Chips for Real-Time Air Quality Monitoring", IEEE Sensors Journal, Vol. 17, Issue 8, pp 2329-2337, April 2017.
3. M. Maldonado-Garcia, **V. Kumar**, J C Wilson, S. Pourkamali, "Chip-scale implementation and Cascade Assembly of particulate matter collectors with embedded resonant mass balances", IEEE Sensors Journal, Volume 17, Issue 6, pp 1617-1625, March 2017.
4. **V. Kumar**, A. Ramezany, M. Mahdavi, S. Pourkamali, "Amplitude Modulated Lorentz Force MEMS Magnetometer with Pico-tesla sensitivity", Journal of Micromechanics and Microengineering, Volume 26, Number 10, 105021, September 2016.
5. **V. Kumar**, R. Jafari, S. Pourkamali, "Ultra-Low Power Digitally Operated Tunable MEMS Accelerometer", IEEE Sensors Journal, Vol 16, Issue 24, Dec 2016.
6. **V. Kumar**, E. Mehdizadeh, S. Pourkamali, "Microelectromechanical Parallel Scanning Nanoprobes for Nanolithography", IEEE Transactions on NanoTechnology, Vol 15, Issue 3, pp 457-464.
7. E. Mehdizadeh, **V. Kumar** and Siavash Pourkamali, "Sensitivity Enhancement of Lorentz Force MEMS Resonant Magnetometers via Internal Thermal-Piezoresistive Amplification", IEEE Electron Device Letters, Vol 35, Issue 2, pp 268-270.

Conference Publications

1. A. Ramezany, S. Babu, **V. Kumar**, J. B. Lee, S. Pourkamali, "Resonant Piezoresistive Amplifiers: towards single element Nano-mechanical RF front ends", IEEE MEMS 2017.
2. **V. Kumar**, A. Ramezany, S. Mazrouei, R. Jafari, S. Pourkamali, "A 3-bit digitally operated MEMS rotational accelerometer", IEEE MEMS 2017.
3. V. Qaradaghi, M. Mahdavi, **V. Kumar**, S. Pourkamali, "Frequency Output mems resonator on membrane pressure sensors", IEEE Sensors 2016.
4. A. Ramezany, V. Qaradaghi, **V. Kumar**, S. Pourkamali, "Frequency Modulated Electrostatically Coupled Resonators for Sensing Applications", IEEE Sensors 2016.
5. A. Abbasalipour, M. Mahdavi, **V. Kumar**, S. Pourkamali, "Nano-Precision Micromachined Frequency Output Profilometer", IEEE Sensors 2016.
6. **V. Kumar**, X. Guo, R. Jafari, S. Pourkamali, "Ultra-Low Power Self-Computing Binary Output Digital MEMS Accelerometer", pp 251-254, IEEE MEMS 2016.

7. **V. Kumar**, S. Pourkamali, “Lorentz Force MEMS Magnetometer with Frequency Modulated Output”, pp 589-592, IEEE MEMS 2016.
8. **V. Kumar**, X. Guo, S. Pourkamali, “A Tunable Digitally Operated MEMS Accelerometer”, IEEE Sensors 2015.
9. M. Maldonado-Garcia, **V. Kumar**, J.C. Wilson and S. Pourkamali, “Miniaturized two stage aerosol impactor with chip-scale stages for airborne particulate size separation”, IEEE Sensors 2015.
10. **V. Kumar**, X. Guo, S. Pourkamali, “Single-Mask Field Emission Based Tunable MEMS Tunneling Accelerometer”, IEEE Nano, 2015.
11. **V. Kumar**, E. Mehdizadeh, S. Pourkamali, “Enhanced Parallel Scanning Probe Nanolithography through Electrically Decoupled 2D MEMS Thermal Actuators”, IEEE Nano 2015.
12. M. Mahdavi, A. Ramezany, **V. Kumar** and S. Pourkamali, “SNR Improvement in Amplitude Modulated Resonant MEMS Sensors Via Thermal-Piezoresistive Internal Amplification”, pp 913-916, IEEE MEMS 2015.
13. M. Maldonado Garcia, E. Mehdizadeh, **V. Kumar**, J.C Wilson and S. Pourkamali, “Chip Scale Aerosol Impactor with Integrated Resonant Mass Balances for Real Time Monitoring of Airborne Particulate Concentrations”, pp 885-888 IEEE MEMS 2015.
14. **V. Kumar**, M. Mahdavi, X. Guo, E. Mehdizadeh and S. Pourkamali, “Ultra-Sensitive Lorentz Force MEMS Magnetometer with Pico-Tesla Limit of Detection”, pp 204-207, IEEE MEMS 2015.
15. Xiaobo Guo, Emad Mehdizadeh, **V. Kumar**, Alireza Ramezany and Siavash Pourkamali, “An Ultra High-Q Micromechanical In-plane Tuning Fork”, IEEE Sensors 2014.
16. E. Mehdizadeh, **V. Kumar**, and S. Pourkamali, “High-Q Lorentz Force MEMS Magnetometer with Internal Self-Amplification”, IEEE Sensors 2014.
17. E. Mehdizadeh, **V. Kumar** and Siavash Pourkamali, “Characterization of a Nanoparticle Collector with Embedded MEMS-Based Mass Monitors”, IEEE NEMS-2014.
18. E. Mehdizadeh, **V. Kumar**, J. Gonzales, R. Abdolvand, and S. Pourkamali, “A Two-Stage Aerosol Impactor with Embedded MEMS Resonant Mass Balances for Particulate Size Segregation and Mass Concentration Monitoring”, IEEE Sensors 2013.